Spring 2019

Biophysical Analyses of Left Ventricular Remodeling Secondary to Myocardial Infarction and Left Ventricular Pressure Overload

William Manuel Torres

Follow this and additional works at: https://scholarcommons.sc.edu/etd

 Part of the Biomedical Commons

BIOPHYSICAL ANALYSES OF LEFT VENTRICULAR REMODELING SECONDARY TO
MYOCARDIAL INFARCTION AND LEFT VENTRICULAR PRESSURE OVERLOAD

by

William Manuel Torres

Bachelor of Science
University of South Carolina, 2014

_____

Submitted in Partial Fulfillment of the Requirements

For the Degree of Doctor of Philosophy in

Biomedical Engineering

College of Engineering and Computing

University of South Carolina

2019

Accepted by:

Tarek Shazly, Major Professor

Francis G. Spinale, Major Professor

Susan M. Lessner, Committee Member

Vijaya B. Kolachalama, Committee Member

Michael R. Zile, Committee Member

Cheryl L. Addy, Vice Provost and Dean of the Graduate School

ii

DEDICATION

I dedicate this work to my friends and family whose unwavering love and support over the last five years have made this work possible. Specifically, I would like to thank my parents, Maria and Willie, for encouraging my dreams and showing me that all of my goals are attainable through hard work and determination. Finally, a special thank you to my beautiful wife, Emily, whose unconditional love keeps me grounded on the most important things in life and makes me want to be my best self.

ACKNOWLEDGEMENTS

My sincere acknowledgement and gratitude go to my advisors, Dr. Tarek Shazly and Dr. Francis G. Spinale. In your own ways, both of you have shown me how to be a successful researcher, driven me to tackle new challenges, and set me up for a successful professional career. I appreciate the enormous amount of time, energy, and resources you have invested in me over the last five years in my pursuit of this doctoral degree. I would also like to thank my dissertation committee members, Dr. Susan M. Lessner, Dr. Vijaya B. Kolachalama, and Dr. Michael R. Zile, for their contributions to my work and their candid feedback along the way. Finally, I would like to thank all of the collaborators and friends I have had the pleasure of working with in both the College of Engineering and the School of Medicine.

ABSTRACT

Left ventricular (LV) remodeling is nominally an adaptive process that restores biomechanical function following myocardial injury and/or sustained alterations in loading conditions. This remodeling can materialize as changes in myocardial geometry, composition, and mechanical properties. When these changes fail to restore LV biomechanical function, remodeling is termed maladaptive. It is generally accepted that maladaptive LV remodeling underlies the progression to heart failure in various forms of heart disease. The central hypothesis of this study is that we can leverage echocardiographic imaging techniques to non-invasively quantify changes in biomechanical function and mechanical properties in a serial manner throughout the progression towards heart failure. The corollary to this hypothesis is that the observed changes in function and mechanical properties can, at least in part, be attributed to a reorganization of collagen within the extracellular matrix. Large animal models of myocardial infarction and left ventricular pressure overload were integrated with echocardiographic imaging, computational modeling, and multi-photon microscopy to test this hypothesis. We posit that this delineation of disease-specific LV remodeling outcomes, with focus on regional mechanical changes throughout the myocardium, will promote translational strategies that can interrupt this deterministic process.

TABLE OF CONTENTS

LIST OF TABLES

LIST OF FIGURES

x

LIST OF ABBREVIATIONS

CVF..Collagen Volume Fraction

ECG..Electrocardiogram

ECM..Extracellular Matrix

EDV ....End Diastolic Volume

EF...Ejection Fraction

ESV ....End Systolic Volume

FE...Finite Element

HF ....Heart Failure

IR..Ischemia-Reperfusion

LA ....Left Atrium

LAD ....Left Anterior Descending Artery

LV ....Left Ventricle

MI...Myocardial Infarction

PCWP...Pulmonary Capillary Wedge Pressure

PO ....Pressure Overload

PSR ....Picrosirius Red

ROI...Region of Interest

SHG..Second-Harmonic Generation

STE ....Speckle Tracking Echocardiography

CHAPTER 1

INTRODUCTION – MECHANOBIOLOGY OF THE HEART

1.1   BASIC ANATOMY AND PHYSIOLOGY

The heart, a muscular organ located in the center of the thoracic cavity, will beat up to 10,000 times in a single day or three billion times over the average lifespan of a human. The primary function of the heart is to serve as the pump in the cardiovascular system which is responsible for delivering oxygen-rich blood and nutrients to every cell in the body via the vascular network of arteries and veins. This circulation of blood is vital to sustaining life.

1.1.1   The Four Chambers of the Heart

The internal anatomy of the heart reveals four chambers composed of cardiac muscle (**Figure 1.1**). The four chambers of the heart are separated into two halves by a central wall, the septum. Each half of the heart functions as an independent pump that consists of an atrium and a ventricle. The atria receive incoming blood from the venous system and the ventricles propel the blood through the arterial system in a continuous loop (**Figure 1.2**). The key function of the right side of the heart is to receive unoxygenated blood from the entire body and deliver it through the pulmonary circulatory system to the lungs for oxygenation. Once the oxygenated blood returns to the heart through the left

1

atrium, it is then actively pumped through to the entire body via the mechanical force resulting from the contraction of the left ventricular myocardium.

The major blood vessels emerge from the base of the heart. The inferior and superior vena cava terminate at the right atrium to return blood to the heart from the rest of the body. The pulmonary trunk, or pulmonary artery, delivers blood to the lungs from the right ventricle. Oxygenated blood returns to the heart from the lungs via the pulmonary vein at the left atrium. Finally, blood is delivered from the left ventricle to the rest of the body first through the ascending aorta. Superficially on the surface of each of the ventricles is a network of coronary arteries and veins which supply blood to and from the heart muscle itself. The left anterior descending artery and the left circumflex artery deliver the vast majority of the oxygenated blood to the left ventricular myocardium so as to ensure it can function properly as a pump.

The flow of blood through the heart is unidirectional. This is made possible by two sets of valves which prevent the backward flow of blood. Between each atrium and ventricle is an atrioventricular valve. These thin flaps of tissue are attached to the base of the atrioventricular union by a ring of connective tissue. The ends of the valves on the ventricular side are attached to collagenous tendons, the chordae tendineae. These chordae tendineae terminate inside the ventricles at a muscle mass called the papillary muscle. While this papillary muscle plays no role in the opening of the valves, its primary function is to stabilize the valves and prevent inversion during ventricular contraction. While similar in function, the two atrioventricular valves are not identical. The valve separating the right atrium and right ventricle is called the tricuspid valve in reference to its three distinct flaps. Alternatively, the atrioventricular valve separating the left atrium and left ventricle only

2

has two flaps and is accordingly called the bicuspid valve. This bicuspid valve is more commonly referred to as the mitral valve in reference to its resemblance to the tall headdress worn by bishops and senior clergy, a miter. Distal to each of the two ventricles is a semilunar valve preventing the backflow of blood from the arteries to the ventricles. Each semilunar valve has three cuplike leaflets which snap closed when the pressure inside of the ventricle drops during ventricular relaxation.

1.1.2 Composition of the Heart

The heart is encased in a tough membranous sac known as the pericardium. The pericardium is attached to the diaphragm and is filled with pericardial fluid that protects the heart and functions similarly to a lubricant. Additionally, this pericardial sac limits the rigid body motion of the heart. The outermost layer of the heart itself is primarily composed of collagenous matrix with some embedded elastic fibers. A cross-section of the heart reveals that there are two additional layers, the middle myocardium and a deep lining called the endocardium. The endocardium is a thin sheet of epithelium that lines the heart and constitutes the valves of the heart. On the other hand, contractile cardiac myocytes make up the bulk of the myocardium and are generally 120 µm long and 20-30 µm in diameter. These cardiac myocytes are arranged in a locally parallel manner and are embedded in an extracellular matrix consisting primarily of collagen. While relatively parallel on a local level, the myocytes are arranged in a spiraled helix that varies transmurally from the endocardium to the epicardium such that the cardiac myocytes can generate sufficient force to direct the proper flow of blood through the cardiovascular system.

3

1.1.3 Contraction of the Heart

Much like skeletal muscle, cardiac muscle is excitable and can generate an action potential. Unlike an innervated skeletal muscle, however, the signal for contraction is generated by specialized non-contractile cardiac cells called autorhythmic cells. These autorhythmic cells are commonly referred to as the pacemaker cells. These autorhythmic cells have an unstable membrane potential which begins at -60 mV and gradually becomes less negative until it reaches a threshold and ultimately triggers an action potential. This action potential, originated by the pacemaker cells in the sinoatrial and atrioventricular nodes, is conducted to the contractile cardiac myocytes. This electrical signal is then converted to a mechanical response (i.e. contraction of the muscle) through a process called excitation-contraction coupling. In this process, calcium ions from the sarcoplasmic reticulum and the extracellular fluid are released and then bind to troponin – thereby initiating the formation of actin-myosin cross-bridges and the contraction of the cell

1.1.4 The Cardiac Cycle

The cardiac cycle is the sequence of rhythmic events including the contraction and relaxation of each of the four chambers of the heart to pump blood through the cardiovascular system. The beginning of the cardiac cycle is commonly marked with the brief moment at which all four chambers are relaxing. In this moment, the atria are filling with blood from the veins. Meanwhile, active ventricular ejection has just been completed. Subsequently, the atrioventricular valves open and blood is passively transferred to the ventricles down the hydrostatic pressure gradient with the assistance of gravity. The final twenty percent of ventricular filling is accomplished as the atria contract and forcibly eject into the ventricles. Ventricular systole then begins and the rapid elevation in pressure

4

pushes against the underside of the atrioventricular valves and forces them closed so that blood does not flow back in the atria. With both the atrioventricular and semilunar valves closed, the cardiomyocytes of the left ventricle continue to contract in what is referred to as isovolumic ventricular contraction. Subsequently, the resultant generation of pressure forces the semilunar valves to open and the blood is pushed in to the arteries. This is referred to as ventricular ejection. The force generated by this ventricular contraction becomes the driving force for blood flow. The high-pressure blood forced in to the arteries then displaces the stagnant low-pressure blood and forces that blood further into the vasculature. At the end of ventricular ejection, the ventricles begin to relax, and intraventricular pressure is reduced. Once the pressure in the arteries exceeds that of the ventricle, the semilunar valves are forced shut by the backflow of blood from the arteries. While the ventricles relax and the intraventricular pressure continues to fall, isovolumic ventricular relaxation occurs. Once the atrial pressure exceeds that of the ventricle, the atrioventricular valves open and initiate the beginning of the next cardiac cycle. This process is summarized in the widely-accepted Wigger's Diagram (**Figure 1.3**) which illustrates the coordination of cardiac events and the resultant relationships between hydrostatic pressure, chamber volumes, and electrical impulses. The entire cardiac cycle is customarily simplified into two distinct phases: systole and diastole. In the left ventricle, the onset of systole is conventionally defined as the time of the mitral valve closure or the by the peak of the QRS complex (i.e. R) on the electrocardiographic signal. The end of systole and the subsequent onset of diastole is conventionally defined as the end of ventricular ejection. Finally, diastole is used to define the entire ventricular filling phase.

1.2   CLINICAL EVALUATION OF HEART STRUCTURE AND FUNCTION

Given the vital importance of the function of the heart to sustaining life, there is an obvious need for techniques that allow for the measurement of the myriad of geometric and functional parameters of the heart in a clinical setting. Advancements in both hardware and software over the years have given rise to a variety of clinically-translatable modalities for this very purpose.

1.2.1   Echocardiography

At present, echocardiography is the most clinically-accessible modality to assess the structure and function of the heart.[1] In short, echocardiography uses ultrasonic waves, in the order of MHz, to provide a real-time image of the beating heart. The ultrasonic beam is produced by a transducer probe and directed towards the region of interest using a transthoracic or transesophageal approach. As the sound waves are intersected by tissues with varying densities, these sound waves are reflected back on the transducer. The detected backscatter will be higher in magnitude for tissues with a higher density. The real-time processing of this backscatter on the ultrasound device allows for a non-invasive bedside visualization of the structure and function of the heart.

Current guidelines for the clinical use of echocardiography reveal that the most common use-case for echocardiography is for the assessment of left ventricular (LV) systolic function and diastolic function.[2] The most commonly reported quantitative measure of global LV systolic function is the ejection fraction (EF) defined as

$$EF = \frac{V_{ED} - V_{ES}}{V_{ED}} \times 100\%. \qquad (1.1)$$

This measurement of EF is reliant on the measurements of LV volumes at end diastole (V_{ED}) and end systole (V_{ES}) determined most commonly from Simpson's biplane method of disks.[3] Along with LV EF and volumes, echocardiography also allows for the quantification of LV internal diameters and wall thicknesses. These measurements give rise to an estimation of LV mass originally proposed by Devereux *et al* in 1986 of the form

$$LV\ mass = 0.8\{1.04[([LVEDD + IVSd + PWd]^3 - LVEDD^3)]\} + 0.6,\quad (1.2)$$

where LVEDD, IVSd, and PWd represent LV, intraventricular septal, and posterior wall thickness at end diastole, respectively.[4]

Going beyond measures of structure and function derived from geometric measurements, Doppler principles have been applied to echocardiographic analysis to allow for quantitative measurements of the hemodynamics in the heart to evaluate global diastolic function.[5] The phenomena first observed by Doppler in the 19th century was that the frequency of a wave can be altered by a moving target acting as interference. In regard to its applicability to cardiac evaluation, the ultrasonic waves emitted by the echocardiographic probe are altered by the movement of red blood cells in such a way that we can derive a complete picture of the cardiac flow field from an analysis of the detected backscatter. Furthermore, the emitted frequency can be tuned for different applications. A pulse-wave Doppler analysis has a high spatial resolution but encounters error when measuring high-velocity flow. Meanwhile, continuous-wave Doppler excels at accurately detecting high-velocity flow, but only flow in the direct line of the emitted signal.[6] While most commonly applied to fluid analysis, the same principles can also be applied to structural analysis where the tissue serves as the interference for the frequency rather than the red blood cells. Through a combinatorial approach of both fluid Doppler and tissue

7

Doppler, we can measure mean pulmonary capillary wedge pressure (PCWP), an indirect estimate of LV diastolic pressure, using the techniques first proposed by Nagueh *et al* in 1997 of the form

$$PCWP = 1.91 + 1.24 \times \frac{E}{E_a}, \quad (1.3)$$

where E is the peak transmitral flow velocity of early left ventricular filling and E_a is the velocity of the movement of the mitral annulus at the lateral site early in diastole.

The most recent advancement to be applied to echocardiographic analysis of the heart is that of strain imaging through speckle tracking echocardiography (STE). An early study by Leitman *et al* in 2004 laid the groundwork for this technology with the initial observation that intrinsic acoustic markers in the myocardium, or speckles, visible in echocardiographic images were stable throughout the cardiac cycle.[7] With this observation, a tracking algorithm was developed to track the movement of the spatial mesh of acoustic markers throughout the cardiac cycle to allow for an accurate measurement of strain in the myocardium. Measurements of segmental strain (ε) are calculated as

$$\varepsilon = \frac{L - L_0}{L_0} = \frac{\Delta L}{L_0}, \quad (1.4)$$

where L is the length of a particular myocardial segment and L_0 is the length of that segment at end diastole. Over the years, this quantitative technique has been applied with increasing regularity for both global and regional analysis of left ventricular function and mechanical behavior.[8] The utilization of different echocardiographic views makes it possible to determine the full field of LV strain in the circumferential, longitudinal, and radial directions.

8

1.2.2 Cardiac Magnetic Resonance Imaging

While echocardiographic analysis is certainly more clinically-accessible, the long-heralded gold standard for the evaluation of cardiac structure and function is cardiac magnet resonance imaging (cMRI). The most prominent advantage that cMRI has over echocardiography is that it is not limited to acoustic windows. The quality of an echocardiographic image varies greatly depending on factors such as anatomical interference (e.g. the location of the lungs) or the degree of obesity of an individual patient. The magnetic field applied in cMRI applications can penetrate through these interferences and capture the entirety of the heart. Furthermore, the application of techniques such as cMRI tagging allows for high-fidelity measurements of deformation throughout the heart.[9,10] Nevertheless, the high cost and long examinations times has severely limited the clinical use of cMRI for the assessment of cardiac structure and function.[11]

1.3   MECHANICAL ASSESSMENT OF THE HEART

Under normal and pathological conditions, the function of the heart is governed and regulated by the underlying mechanics of both the structure and the myocardium. Broadly speaking, mechanics refers to the relationship between the forces applied to an object and the translation, rotation, and deformation resulting from these applied forces. In the living heart, the total mechanical behavior would be defined as the sum of both the active mechanics resulting from the contractile cardiac myocyte and the passive mechanics of the completely relaxed myocardium. While there is interrelation between these two forces, for the purposes of this review, we focus only on the passive mechanics of the myocardium.

9

An understanding of the relationship between the passive mechanical properties of the heart and their effect on function is the central goal of cardiac mechanics research.

1.3.1 Benchtop (*ex-vivo*) Analysis

The majority of the early work characterizing the mechanics of the passive myocardium came from uniaxial tests on excised pieces of cardiac tissue.[12,13] Despite the significance of this early work, further investigation into the locally heterogeneous structure of the myocardium gave rise to a need to move beyond an assumption of isotropic behavior. To that end, studies using biaxial test setups would later show that the passive myocardium exhibits an anisotropic behavior that varies from region to region.[14] This work gave rise to a "golden-era" of cardiac mechanics research from 1980-2000 where a number of constitutive models were developed to link the states of stress and strain in the passive myocardium.[15–20] Further work was completed by Zile and colleagues to isolate the cardiac myocyte and perform tensile testing and eventually define constitutive relations for the isolated myocyte. While there is clear value in these monumental studies, no one experiment is comprehensive. It must be considered that the excision of these tissues influences hormonal factors and control of the nervous system and ultimately the properties of the cardiac myocytes, the myocardium, and the heart as a whole.

1.3.2 Clinical (*in-vivo*) Analysis

Technological advancements over the last few decades have made it possible to perform mechanical analysis for clinical research. One of the most important advancements in that time was the advent of sensitive cardiac catheters for the measurement of intraventricular pressures. The use of these catheters along with image modalities such as angiography or echocardiography allowed for detailed analysis of the relationship between

pressure and volume throughout the cardiac cycle. Early work by Mirsky and Pasipoularides laid the foundation for this work.[21,22] They first introduced the concept of calculating an index of LV chamber stiffness of the form

$$P = P_0 e^{K_C \frac{V}{V_W}}, \ (1.5)$$

where P is the intraventricular pressure, P_0 is a fitting parameter, K_C is the chamber stiffness, V is the volume of the ventricular chamber, and V_W is the volume of the wall. This measurement of chamber stiffness, a structural index that is a function of geometry and local material properties, has proven to be a valuable index of diastolic function.[23] On a local level, Janz introduced a method by which to quantify local myocardial wall stress

$$\sigma = \frac{Pr^2}{2t(sin\theta)(r+\frac{t(sin\theta)}{2})}, \ (1.6)$$

where P is the intraventricular pressure, r is the local radius, t is the local thickness, and θ is angle between the normal vector from the endocardium at the region of interest and the axis of revolution in the truncated ellipsoid model.[24] Since then, the major push in the *in-vivo* analysis of cardiac mechanics has come by way of advanced finite element analysis. The work by Costa, Wenk, and others of the normal and diseased heart serves as demonstration that detailed biomechanical analysis using computational tools is feasible, albeit at the cost of computational time, the need for expert analysis, and expensive hardware resources.[25–29] There is a clear need for this type of technology to be made more clinically accessible and practical for the routine analysis of cardiac mechanical function.

11

1.4　HEART FAILURE – ONE SYNDROME WITH MULTIPLE ETIOLOGIES

1.4.1　Clinical Relevance

An all-too-common pathway for a host of cardiac disorders is a progression towards heart failure. Heart failure is a complex clinical syndrome that can result from any structural or functional cardiac disorder that impairs the ability of the ventricle to fill with or eject blood. The rate and incidence of the development and progression of heart failure continues to escalate, and recent statistics have identified this disease as the leading cause of morbidity and mortality – eclipsing all other chronic diseases.[30] While significant progress has been achieved in the therapeutic management of other major illnesses such as cancer, these advancements have not been forthcoming for heart failure. One likely reason for this is that, unlike cancer which is classified by morphology, cell type, and molecular/genetic profiles, heart failure has been historically considered as a single entity. However, it has become recognized that distinctly different etiologies for the presentation of these heart failure symptoms exist, which, in turn, have demonstrated distinctly different therapeutic responses and clinical outcomes.[31] A recent consensus has emerged that a generalized dichotomy can be made for the classification of heart failure through the evaluation of LV EF.[32] Specifically, heart failure patients presenting with a LV EF below 45% would be classified as heart failure with reduced ejection fraction (HFrEF). Alternatively, those heart failure patients with a normal LV EF (i.e. greater than 45%) would be classified as heart failure with preserved ejection fraction (HFpEF). It has been found that the prevalence of these two phenotypes of heart failure is equally distributed.[31] Furthermore, long-term morbidity and mortality rates between the two phenotypes are virtually indistinguishable.[33] Ultimately, these trends warrant further investigation so as to

12

delineate the pathophysiological mechanisms which give rise to each phenotype of heart failure (**Table 1.1**). Though the progression to heart failure is unequivocally multi-factorial in nature, the changes associated with both types of heart failure can be attributed to the cumulative alterations in geometry, composition, and function; defined as remodeling.

1.4.2   Systolic Heart Failure (HFrEF)

Systolic heart failure, commonly referred to as HFrEF, is a clinical syndrome characterized by a dilation of the left ventricle and impaired systolic pump function. HFrEF is an all-too-common sequela of myocardial infarction (MI). A MI occurs secondary to an acute coronary event which functionally cuts off the flow of oxygen-rich blood to the area of the myocardium supplied by that vessel. This local ischemia results in cardiac myocyte death and the development of a non-viable and fibrotic scar.[34] In the days and weeks that follow this acute event, there are progressive changes in the LV geometry on a global (e.g. increased end-diastolic volume) and local (e.g. thinning within the MI region and hypertrophy of the viable remote region) scale.[35–41] Critically, these structural abnormalities have a detrimental effect on the systolic function of the LV. This systolic dysfunction becomes apparent through an analysis of LV EF as it commonly falls below 45%.[42] This fall in EF can be attributed to several factors such as severe dilation of the LV, a high prevalence of non-viable myocardium, and changes in the passive mechanical properties of both the MI region and the remote myocardium.[41,43,44] Ultimately, the inability to meet the metabolic demands of the body through normal pump function gives rise to the presentation of the signs and symptoms of HFrEF.

13

1.4.3 Diastolic Heart Failure (HFpEF)

Diastolic heart failure, commonly referred to as HFpEF, is a clinical syndrome characterized by a presentation of the signs and symptoms of heart failure, abnormal diastolic function, and a preserved ejection fraction. Conceptually, HFpEF occurs when the LV chamber compliance is reduced to the point at which it can no longer accept an adequate volume of blood during the diastolic filling phase. This type of heart failure commonly results from an exposure to a prolonged LV pressure overload such as aortic stenosis.[45] HFpEF that occurs secondary to LV pressure overload results in a thick, hypertrophied, left ventricle. Furthermore, this disease is coincident with the presentation of abnormal active relaxation. This phenomena becomes apparent through the echocardiographic observation of either a prolonged isovolumic relaxation phase or delayed active relaxation.[46] In addition to active relaxation, the passive mechanical properties of the LV myocardium contribute to this presentation of diastolic dysfunction. On a structural/chamber level, this is made evident by elevations in chamber stiffness (K_C) determined from end diastolic pressure-volume relations.[3,47,48] On a local material level, the determination of regional myocardial stiffness (K_M) from stress-strain or stress-diameter relationships reveals increases in the passive stiffness of the cardiac myocyte and the extracellular matrix it is embedded within.[42,49] Coupled together, abnormal relaxation and increases in stiffness ultimately initiate a cascade of events including elevations in LV filling pressures, dilation of the left atrium, and a presentation of the signs and symptoms of HFpEF.[50,51]

14

1.5   DISSERTATION SCOPE AND SPECIFIC AIMS

The primary goal of this dissertation is to advance the state of knowledge in the field in regard to pathophysiological mechanisms which give rise to heart failure and how they interrelate with local changes in mechanical behavior and mechanical properties as a consequence of disease-induced remodeling. The central hypothesis of this study is that we can leverage echocardiographic imaging techniques to non-invasively quantify changes in biomechanical function and mechanical properties in a serial manner throughout the progression towards heart failure. The corollary to this hypothesis is that the observed changes in function and mechanical properties can, at least in part, be attributed to a reorganization of collagen within the extracellular matrix. This hypothesis was tested with a combinatorial approach of clinically-relevant large animal models of heart failure, novel image-processing techniques, and computational modeling. These results provide novel information on LV remodeling outcomes in clinically-relevant disease states and lay the groundwork for the evaluation of emergent therapeutic strategies that seek to curtail adverse remodeling.

1.5.1   Aim 1 – Quantify regional and temporal changes in left ventricular strain and stiffness in a porcine model of myocardial infarction

For the first time, STE was used to serially track regional biomechanical behavior and mechanical properties post-MI. We found that changes initially confined to the MI region extended throughout the myocardium in a non-uniform fashion over 28 days post-MI. We posit that STE-based evaluation of regional changes in LV biomechanics could advance both clinical assessment of left ventricular remodeling and therapeutic strategies that target aberrant biomechanical behavior post-MI.

15

1.5.2 Aim 2 – Quantify changes in myocardial microstructure and mechanics secondary to left ventricular pressure overload

Left ventricular pressure overload has been shown to give rise to the HFpEF phenotype. LVPO was induced in mature pigs by inflation of an implanted ascending aortic cuff for up to five weeks. Serial echocardiographic analyses of diastolic function and mechanical properties along with terminal histological analysis allowed for a correlative analysis of the abnormalities in the microstructural composition of the extracellular matrix and these observed changes in structure and function. Our findings support the use of serial biomechanical analysis to track the progression of HFpEF and present a translational method to stratify patient-specific risk and assess the efficacy of pharmacological and therapeutic approaches.

1.5.3 Aim 3 – Develop a clinically-accessible tool for the identification of the passive mechanical properties of the left ventricular myocardium

Sensitive techniques to track the rate and extent of remodeling are necessary to evaluate risk and treatment options on a patient-specific basis throughout the progression to heart failure. The technology we have developed is a novel and non-obvious extension of two-dimensional STE which allows for the definition of a constitutive relation for the regional left ventricular myocardium that links the states of stress and strain. This was accomplished through the use of an inverse finite element analysis approach along with a novel objective function which accounts for regional differences in strain and thickness. This technology allows for a comprehensive biomechanical analysis of the left ventricle to be performed in a clinical setting for the assessment of the rate and extent of myocardial remodeling in response to heart disease.

16

Table 1.1: Features that differentiate HFrEF from HFpEF.

Characteristics	HFrEF	HFpEF
Systolic function		
Ejection fraction	↓↓	N
Stroke volume	↓	N
Contractility	↓↓	↓
Diastolic function		
LV end diastolic pressure	↑	↑↑
Relaxation time constant	↑	↑↑
Filling rate	↓	↓
Chamber stiffness	↓	↑↑
Myocardial stiffness	↑	↑
Remodeling		
LV volume	↑↑	N
LV mass	↑	↑
LV geometry	Eccentric	Concentric
Cardiomyocyte	↑ (Length)	↑ (Diameter)
Mortality at 5 years	↑↑	↑
Morbidity at 5 years	↑↑	↑↑

HFrEF = Heart failure with a reduced ejection fraction; HFpEF = Heart failure with a preserved ejection fraction; LV = left ventricular, N = normal; ↓ = decreased; ↑ = increased. *Table adapted from Zile MR. Heart failure with preserved ejection fraction: Is this diastolic heart failure? *J Am Coll Cardiol*. 2003;41:1519-1522.
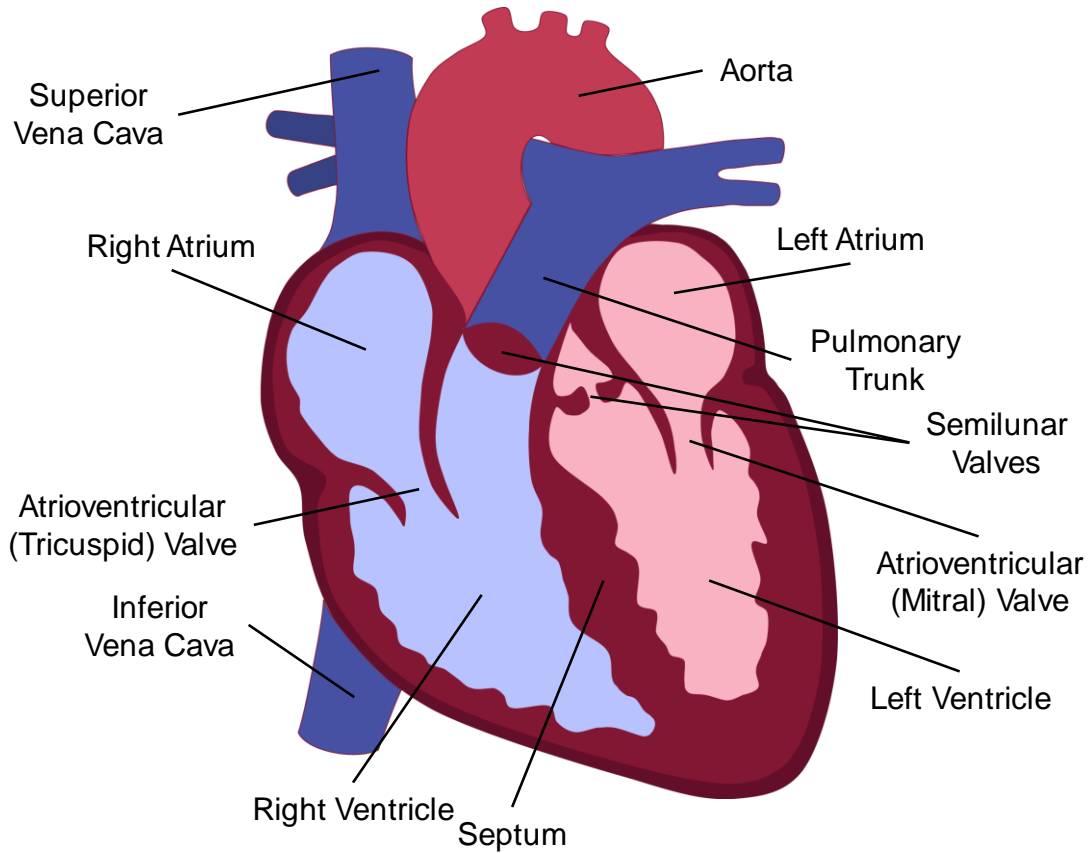
Figure 1.1: Anatomy of the heart and major blood vessels.
There are four main chambers to the heart: right atrium, right ventricle, left atrium, and left ventricle. The atria and ventricles are separated by atrioventricular valves and the semilunar valves prevent backflow of blood from the major arteries to the ventricles.
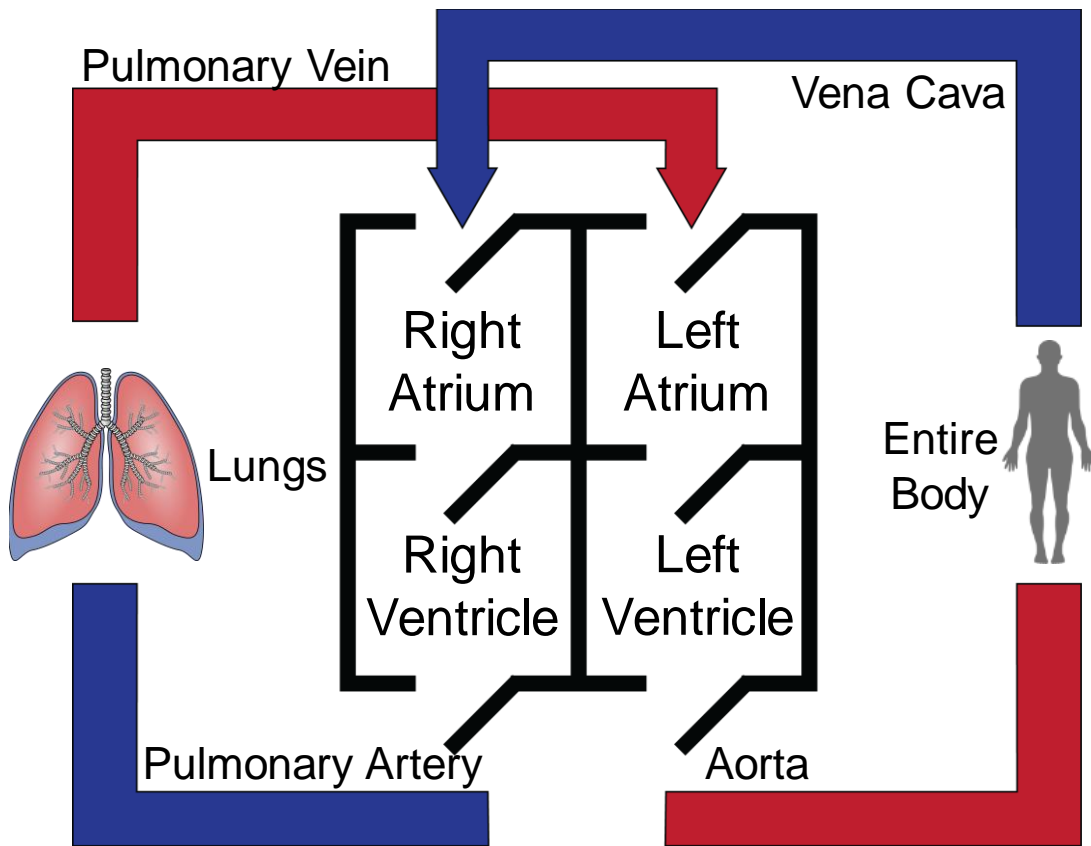
Figure 1.2: Cardiovascular circulation.
Blood collected in the right atrium is pumped into the right ventricle. Contraction of the right ventricle sends the blood through the pulmonary system for oxygenation. After oxygenation, the blood returns to the heart through the left atrium. Blood then goes to the left ventricle where the force is generated to pump the blood through the rest of the body.
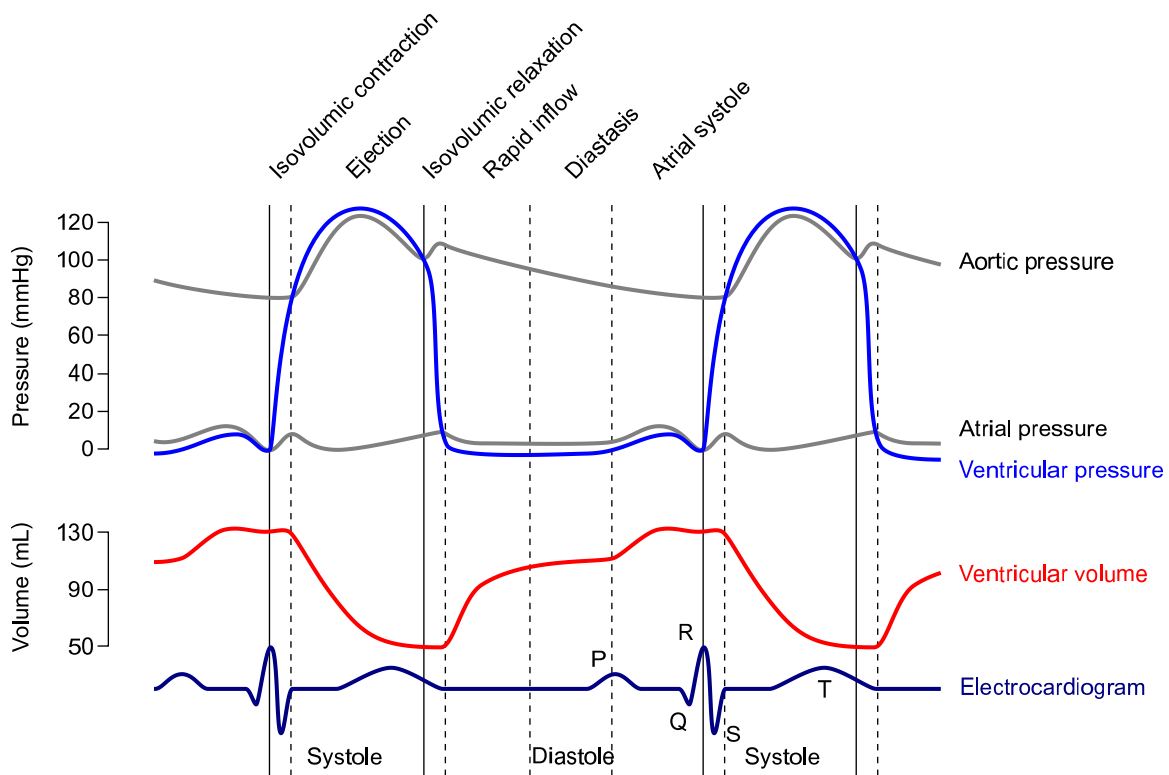
Figure 1.3: Wigger's Diagram.
This diagram is a representation of the electrical and mechanical events of the cardiac cycle. By DanielChangMD, revised original work of DestinyQx, redrawn as SVG by xavax (Wikimedia Commons, File: Wiggers_Diagram.svg), "Wigger's Diagram", https://creativecommons.org/licenses/by-sa/2.5/legalcode

CHAPTER 2

REGIONAL AND TEMPORAL CHANGES IN LEFT VENTRICULAR

STRAIN AND STIFFNESS IN A PORCINE MODEL OF

MYOCARDIAL INFARCTION [1]

2.1 ABSTRACT

The aim of this study was to serially track how myocardial infarction (MI) impacts regional myocardial strain and mechanical properties of the left ventricle (LV) in a large animal model. Post-MI remodeling has distinct regional effects throughout the LV myocardium. Regional quantification of LV biomechanical behavior could help explain changes in global function and thus advance clinical assessment of post-MI remodeling. The present study is based on a porcine MI model to characterize LV biomechanics over 28 days post-MI via speckle-tracking echocardiography (STE). Regional myocardial strain and strain rate were recorded in the circumferential, radial, and longitudinal directions at baseline and at three, 14, and 28 days post-MI. Regional myocardial wall stress was calculated using standard echocardiographic metrics of geometry and Doppler-derived hemodynamic measurements. Regional diastolic myocardial stiffness was calculated from the resultant stress-strain relations. Peak strain and phasic strain rates were nonuniformly reduced throughout the myocardium post-MI, while time to peak strain was increased to a similar degree in the MI region and border zone by 28 days post-MI. Elevations in diastolic myocardial stiffness in the MI region plateaued at 14 days post-MI, after which a significant reduction in MI regional stiffness in the longitudinal direction occurred between 14 and 28 days post-MI. Post-MI biomechanical changes in the LV myocardium were initially limited to the MI region but nonuniformly extended into the neighboring border zone and remote myocardium over 28 days post-MI. STE enabled quantification of regional and temporal differences in myocardial strain and diastolic stiffness, underscoring the potential of this technique for clinical assessment of post-MI remodeling.

22

2.2   INTRODUCTION

The post-MI period is accompanied by temporal changes in inflammatory-signaling-proteolytic cascades within the MI region, which in turn give rise to changes in LV geometry, composition, and function in a process termed post-MI remodeling [52,53]. Global changes in LV geometry (e.g., increased EDV) and pump function (e.g., reduced EF) are commonly used to assess the relative extent of post-MI remodeling [54–56]. However, this is a spatially nonuniform process, as myocardial thinning (within the MI region) occurs concomitantly with hypertrophy (within the viable remote region) [35,36]. As such, improved regional assessment of temporal changes throughout the myocardium may enhance clinical evaluation of the rate and extent of the post-MI remodeling process.

In vivo regional mechanical behavior has been assessed post-MI in both basic scientific and clinical studies using techniques such as sonomicrometry, cardiac magnetic resonance imaging, and tissue Doppler-derived imaging [57–63]. While these and other approaches have yielded critical information on the post-MI remodeling process, they have not been uniformly applied to assess LV regional function across the entire chamber and in a serial fashion due to several factors. In large animal studies using sonomicrometry, high spatial and temporal resolution is offset by a limited field of view [58,59]. In clinical studies, noninvasive approaches such as cardiac magnetic resonance imaging can provide high fidelity regional assessment of LV function, but lengthy acquisition and post-processing times make it impractical to collect repeated measurements [60]. Tissue Doppler-derived imaging has also been applied in both large animal models and clinical settings to quantify regional myocardial strain with reported limitations stemming from a significant dependency on the angle of the ultrasound beam and low signal-to-noise ratio [61–63].

23

STE, an ultrasound-based technique which tracks the movement of intrinsic acoustic markers of the LV, has the potential to address limitations of tissue Doppler approaches. Past large animal and clinical studies have demonstrated the feasibility of STE in terms of post-MI assessment of LV regional function [64–72]. It has been established that longitudinal strain patterns can be used to identify regions of ischemic injury and predict remodeling outcomes [64,65]. Measures of global radial and circumferential strains have shown correlation with MI size and can enable differentiation between subendocardial and transmural infarction [67–69]. STE can also capture the heterogeneous and temporal changes in LV strain in the minutes immediately after MI and over more extensive time intervals post-MI [70–72]. Despite these advancements, there is a paucity of studies that have applied STE to serially assess the extent and magnitude of changes in regional strain over the critical early remodeling period (up to 28 days post-MI) in a large animal model. Furthermore, no studies to date have extended STE to track regional mechanical property changes post-MI. The current study utilizes a porcine model of an acute coronary syndrome and subsequent MI based on an intracoronary IR approach; STE is then performed up to 28 days post-MI. We postulate that this combinatorial approach to the in-vivo quantification of LV mechanical behavior post-MI will yield novel insight into the progression of the post-MI remodeling process and thereby motivate the development of therapeutic strategies, which aim to mitigate these adverse effects.

2.3   METHODS

2.3.1   IR Protocol

Mature pigs (n=8) (Yorkshire, male, 22.0 ± 0.9 kg) were administered amiodarone (200 mg PO) and aspirin (81 mg PO) for three days pre-operatively and a broad-spectrum antibiotic (Draxxin, 2.5 mg/kg, IM) at least once pre-operatively. On the day of surgery, the pigs were sedated (ketamine/acepromazine/atropine: 22/1.1/0.04 mg/kg IM, respectively), intubated, and then maintained on $1.5 - 2.0$ % isoflurane delivered in an oxygen/nitrous mixture (3:1 L/min, respectively). Buprenorphine (0.05 mg/kg IM) was administered as pre-surgery analgesia. An intravenous infusion (via ear vein cannula) of Benadryl (25 mg) in conjunction with a continuous lidocaine infusion (4 mg/kg/hr) and lactated ringer's solution (10 mL/kg/hr) was initiated. The region encompassing the right femoral artery was prepared in a sterile fashion, the main branch of the femoral artery surgically exposed, and a catheter introducer (6F Input Introducer Sheath, Medtronic) positioned and stabilized in the artery. A bolus of heparin was administered (4000 units, IV) prior to placement of the guide catheter followed by an additional bolus every hour (1000 units, IV). Under fluoroscopic guidance (GE OEC 9600, UT), a coronary angiography catheter/launcher (5F Launcher guiding catheter .058" HSI, Medtronic) was placed in the left coronary ostia, and an angioplasty balloon catheter containing an injection lumen (3mm x 10mm Sprinter OTW balloon catheter, Medtronic) was positioned in the lower portion of the left anterior descending artery (LAD; defined as 1 cm below the First Diagonal). The LAD was occluded by balloon inflation (12 ATM balloon inflation pressure, Everest 30 Disposable inflation device, Medtronic) and maintained for 90 minutes. The balloon was then deflated, and the catheter system disengaged and removed.

The femoral artery was ligated, and the incision closed. A transdermal fentanyl patch was placed for three days for post-operative analgesia. Prior studies have demonstrated that this technique produces a highly-reproducible anteroapical ischemic region resulting in an MI, which constitutes approximately 8.7% ± 1.3% of the entire LV at 28 days post-MI [73,74].

All experimental protocols were approved by the Institutional Animal Care and Use Committees at the University of South Carolina and performed according to the National Institutes of Health guidelines for Care and Use of Laboratory Animals.

2.3.2 Standard Echocardiography

The day before the animals underwent the IR protocol, they were sedated (diazepam, 200 mg PO, Barr Laboratories, Pomona, NY), placed in a custom-designed sling, and echocardiography was performed (GE Vivid E9 with XDclear Ultrasound System: M5S (1.5-4.6 MHz) transducer probe). Cardiac dimensions and function were assessed by two-dimensional echocardiographic studies. The transthoracic images were acquired from a right parasternal approach and the LV was imaged in long axis and short axis views. The short axis views were taken at the level of the papillary muscles. EDV, ESV, and EF were calculated using the biplane method of disks. Pulse-wave Doppler, using a sample volume placed at the tips of the mitral valve leaflets, was used to determine the peak early mitral inflow velocity (E). Tissue Doppler assessment was used to calculate the peak early mitral annular velocity (E') with a sample volume positioned at the lateral site of the mitral annulus. PCWP was calculated using the method proposed by Nagueh et al in 1997. Additionally, wall thickness was collected at early- and end-diastole for each of the six conventional echocardiogram LV segments in the parasternal long-axis and papillary

level short-axis. The pigs were returned to the laboratory under identical sedation/study conditions at three, 14, and 28 days post-MI.

2.3.3 Strain Imaging

Digital loops of the two-dimensional echocardiography for the long axis and papillary short axis (acquired at 40 Hz) were stored on a hard disk and transferred to a workstation (EchoPac, Vingmed, General Electric) for post-processing. For each digital loop, a ROI was defined at the onset of the R-wave by manually identifying the endocardial and epicardial borders. The ROI was then discretized with a spatial mesh of acoustic clusters to be tracked on a frame-to-frame basis throughout a single cardiac cycle [7]. The end of systole was defined as the point at which the LV cross-sectional area was at a minimum. After the semi-automated grouping of acoustic clusters in accordance with six anatomical locations (**Figure 2.1A**), regional tracking quality was assessed, and the ROI was manually adjusted by the operator to improve tracking quality where necessary. Successful tracking of the ROI allows for the definition of segmental lengths, which are computed at end diastole (L_0) and continuously throughout the cardiac cycle (L). Local segmental strains (ε) and strain rates (γ) are then computed as:

$$\varepsilon = \frac{L-L_0}{L_0} = \frac{\Delta L}{L_0} \qquad (2.1)$$

$$\gamma = \frac{(\Delta L/\Delta t)}{L_0} \qquad (2.2)$$

where Δt is the relative time in the cardiac cycle. Peak strain, systolic strain rate, and diastolic strain rate were quantified in the three normal directions: circumferential (papillary short axis), radial (papillary short axis), and longitudinal (long axis). Circumferential and longitudinal segmental strains/strain rates were quantified at the

27

epicardial, mid-myocardial, and endocardial surfaces. Global strain values were calculated as the mean segmental strain observed in the 18 myocardial segments in the circumferential and longitudinal directions and six segments in the radial direction. Obtained segmental strain and strain rate data were assessed for intra-observer variance by calculating the intra-class correlation coefficient for a single operator under the assumption that systematic differences are relevant. The intra-class correlation coefficient for all measures of strain and strain rate ranged from 0.94 to 0.99.

2.3.4 Aggregate Regional Definitions

In this study, each pig had a total occlusion of the LAD. To facilitate data analysis, we defined the following aggregate regions: the MI region is all anterior and anteroseptum walls; the border zone is the apical and mid posterior, basal septal, and basal lateral walls; the remote region is the basal posterior and inferior walls. While the size of the MI region, and thus the size and location of the border zone, change over time post-MI, the use of consistent regions at all study time points allows for the continuous monitoring of local biomechanical changes throughout the myocardium.

2.3.5 Mean Wall Stresses

We modified a thick-walled ellipsoidal model proposed by Janz [24] to compute mean wall stresses. The mean circumferential wall stress (σ_C) was computed as:

$$\sigma_C = \frac{Pr^2}{2t(r+\frac{t}{2})} \qquad (2.3)$$

where (r) is the inner radius, (t) is the wall thickness, and (P) is the LV pressure. For the purposes of this study, (P) was assumed to equal zero at the onset on diastole and the PCWP at end-diastole.

The mean longitudinal wall stress (σ_L) was computed as:

$$\sigma_L = \frac{Pr^2}{2t(sin\theta)(r+\frac{t(sin\theta)}{2})} \qquad (2.4)$$

where (Φ) is the angle between the normal vector from the endocardium at the ROI and the axis of revolution in the truncated ellipsoid model.

2.3.6   Regional Diastolic Myocardial Stiffness

Obtained values for mean wall stresses and segmental strains at the onset of diastole and end-diastole enabled calculation of regional diastolic myocardial stiffness in both the circumferential and longitudinal directions. The slope of the line between these two points in the stress-strain plane, developed in either the circumferential or longitudinal direction and referenced to the defined anatomical locations, was used to compute the regional diastolic myocardial stiffness (K_{MR}) as:

$$\kappa_{MR} = \frac{\sigma_{ED}}{|\varepsilon_{D0}|} \qquad (2.5)$$

where σ_{ED} and ε_{D0} are the end diastolic mean wall stress and segmental strain at the onset of diastole, respectively.

2.3.7   Statistical Analysis

Data are reported as the mean ± standard error of the mean. A *post hoc* analysis of baseline (pre-MI) global stiffness values with an assumption of a 30% effect and sample size of eight yielded a statistical power of greater than 80%. The comparative analysis was performed with either a one-way or two-way analysis of variance followed by pair-wise comparisons using the LSD *post hoc* study. All statistical analyses were performed with SPSS software (version 24.0, SPSS Inc). A p-value less than 0.05 was considered statistically significant.

2.4   RESULTS

2.4.1 LV Function and Geometry

Assessments of LV function and geometry at baseline and at specific post-MI time points are shown in **Table 2.1**. At 28 days post-MI, LV EF fell by over 40%, LV EDV more than doubled, and PCWP increased by 80% relative to baseline values.

2.4.2 STE-Based Strain Measurements

Representative plots of mid-myocardial segmental strains **(Figure 2.1B)** demonstrate that STE provided a continuous strain measurement over the cardiac cycle at all specified anatomical locations. As depicted by a representative LV circumferential section, the MI region, border zone, and remote region are contained within the designated myocardial regions at 28 days post-MI, thus supporting the aggregate definition of these regions throughout the study (**Figure 2.2**). Spatial maps of peak segmental strains qualitatively show that post-MI changes varied throughout the myocardium and exhibited obvious directional dependence **(Figure 2.3)**. At three days post-MI, peak global strain in the radial and longitudinal directions decreased by approximately 40%, whereas reduction in the circumferential direction was not significant until 28 days post-MI.

The relative time at which peak strain occurred in the MI region increased by approximately 30%-40% with respect to baseline at three days post-MI in all directions, with these early changes in the circumferential and longitudinal directions largely maintained throughout the study observation period (**Figure 2.4**). Within the border zone, an approximate 30% increase in the relative time to peak strain occurred at all post-MI times in the radial direction, but significant increases in the circumferential and

30

longitudinal directions were only recorded at 28 days post-MI. The remote region exhibited the least pronounced changes, as the only significant deviations from baseline were found in the radial direction at 28 days post-MI.

2.4.3 Phasic Strain Rates

Spatial maps of segmental strain rates show that MI impacted both phases of the cardiac cycle and that the greatest reductions in strain rates primarily occurred within the MI region (**Figure 2.5**). Reductions of over 50% in global systolic strain rate were observed at three days post-MI in the radial and longitudinal directions but were not significant until 28 days post-MI in the circumferential direction. Global diastolic strain rates were relatively preserved post-MI with significant reductions observed only at 14- and 28-days post-MI in the longitudinal direction.

2.4.4 Mean Wall Stresses and Diastolic Myocardial Stiffness

End-diastolic mean wall stress monotonically increased throughout the 28-day observation period in both the circumferential and longitudinal directions with all regional values approximately doubling with respect to baseline by 28 days post-MI (**Figure 2.6**). Spatial maps of diastolic myocardial stiffness show that mechanical heterogeneity evidently increased post-MI (**Figure 2.7A**). Global diastolic myocardial stiffness underwent a greater than three-fold elevation by 14 days post-MI in the circumferential direction and three-fold elevation by three days post-MI in the longitudinal direction. In the longitudinal direction, significant diastolic myocardial stiffness elevations occurred in the MI region and border zone by three days post-MI and by 14 days post-MI in the remote region (**Figure 2.7B**). All three regions exhibited significantly elevated diastolic myocardial stiffness by 14 days post-MI in the circumferential direction. In the MI region,

31

diastolic myocardial stiffness in both directions was maximal at 14 days post-MI. In the longitudinal direction, an approximate 40% decrease in stiffness from this maximal value occurred between 14- and 28-days post-MI.

2.5   DISCUSSION

2.5.1   Study Overview

Changes in LV geometry and function invariably occur following MI in a multifactorial process termed post-MI remodeling [52,53]. Given the inherent spatial nonuniformity of post-MI remodeling, approaches for quantifying LV function in a global context can be problematic, and therefore assessment of regional biomechanics may provide improved insight into this process. The present study addressed this issue by serially examining LV strain and strain rates, indices of myocardial function, in defined myocardial regions post-MI. Using a large animal model of post-MI remodeling and STE-derived indices, the significant findings from this study were two-fold. First, myocardial strain and strain rate fell within the MI region at three days post-MI, consistent with a loss of viable myocardium and hence contractile capacity. However, while the reduction in strain patterns was confined initially within the MI region, this reduction nonuniformly extended into the viable LV myocardial regions over one-month post-MI. Second, when regional myocardial diastolic stiffness was computed using local stress-strain relationships, a biphasic change within the MI region was observed. Specifically, diastolic myocardial stiffness initially increased within the MI region but at later post-MI time points remained constant in the circumferential direction and significantly fell in the longitudinal direction. Despite these regional and directional differences, diastolic myocardial stiffness was

32

significantly elevated throughout the entire myocardium by 28 days post-MI. Thus, serial assessment of regional LV function post-MI identified that time- and region-dependent changes in myocardial mechanical properties occur over 28 days post-MI, potentially providing more sensitive response variables when evaluating disease progression and therapeutic interventions.

2.5.2 Previous Supportive Findings

STE-based strain measures in our study were comparable to previous large animal and clinical studies. Specifically, our baseline global strain values fell within normal ranges defined by a meta-analysis of over 2,500 human subjects [75]. Additionally, directional changes in peak strain observed in the MI region, border zone, and remote region track well with those reported in other large animal models [70,71]. Our data also support previous studies that found elevated MI region stiffness [76–79], including via sonomicrometry [58] and three-dimensional magnetic resonance [80]. Moreover, results from planar bi-axial mechanical testing on freshly excised square samples of remote and infarcted myocardium showed that MI region stiffness peaked at one- to two-weeks post-MI, followed by a period of decreasing stiffness [81].

2.5.3 Mechanistic Implications

The present study identified unique spatial, directional, and temporal variations in regional function during post-MI remodeling, which are associated with increased mechanical heterogeneity throughout the LV myocardium. We posit that this mechanical heterogeneity may be the biophysical stimulus that is translated into cellular and extracellular changes within the MI and surrounding region, ultimately contributing to MI expansion and eventually LV failure. For example, during the first 14 days post-MI, the

33

diastolic myocardial stiffness of the MI region and the neighboring border zone became increasingly disparate, exemplified by the nearly order-of-magnitude greater MI region stiffness in the longitudinal direction. Such abrupt spatial gradients in mechanical stiffness that emerge between the MI and viable regions likely induce localized elevations in myocardial wall stress and dyskinesis throughout the cardiac cycle, which in turn would stimulate further remodeling and the progressive expansion of the MI region [82]. The reduction in stiffness of the MI region observed at 28 days post-MI relative to 14 days post-MI may facilitate the continued expansion of the MI region as evidenced by the increase in LV EDV over that period. Furthermore, relative values of border zone/MI region stiffness at 14- and 28-days post-MI suggest that at the terminal time point, mechanical properties throughout the myocardium become more homogenous in both the circumferential and longitudinal directions. Such property homogenization may, in turn, suggest an approach to mechanical homeostasis by 28 days post-MI – commensurate with the plateau in MI region expansion reported in previous studies [57]. Conversely, the progressive stiffening of the hypertrophied remote region between 14 and 28 days may play a pivotal role in driving the elevations in PCWP which may, in turn, facilitate the LV dilation. To promote further association of regional mechanical property changes with global LV function, we consider as an index of LV chamber stiffness the ratio between PCWP and LV EDV. When computed using our data, this index at baseline is valued as 0.24 ± 0.04 and is found to be consistently reduced by 40% relative to baseline at 14- and 28-days post-MI. Antithetical changes in diastolic myocardial stiffness of the MI region and remote region between 14 and 28 days post-MI may explain the relatively constant index of LV chamber stiffness over this post-MI period. The coincidence between the

34

divergence of regional changes in myocardial mechanical properties and the development of congestive symptoms suggests that regional stiffness variations may be a key factor, and thus therapeutic target, in heart failure progression.

These biomechanical changes are also seemingly synchronized with deterministic biological processes that occur in and around the MI region. These changes include fibroblast proliferation and collagen deposition – resulting in the formation of a mature scar composed of extracellular matrix by 14 days post-MI [83]. This intermediate phase of post-MI remodeling also concurs with the highest disparity in fibrillar collagen content between the MI region and border zone and dynamic changes in protein expression profiles, which directly modulate the reparative response [84]. Furthermore, there is evidence that many of these regional biophysical changes are modulated by mechanosensitive cardiac cells that sense and respond to their local mechanical environment [85]. To that end, mechanical heterogeneity that emerges post-MI represents a biophysical response variable that can explain temporal and spatial variations in key biological processes that occur during post-MI remodeling.

2.5.4   Therapeutic Implications

While cause and effect relationships are difficult to discern with respect to synchronized biological versus biomechanical changes, our data support the regional modulation of myocardial mechanical properties as a potential therapeutic target. As suggested above, the increase in EDV from 14 to 28 days may be facilitated by a decrease in MI region stiffness, suggesting that treatment to maintain or increase MI region stiffness may blunt dilation. Similarly, the increase in PCWP from 14 to 28 days may be facilitated by an increase in remote region stiffness, suggesting that treatment to decrease remote

35

region stiffness may also blunt dilation. Indeed, previous studies show that biomaterials directly injected into the MI region acutely stiffen the myocardium and effectively curtail the adverse effects of post-MI remodeling [86,87]. Regional biomechanical assessment can be used to advance local biomaterial injection strategies, including the optimization of biomaterial mechanical properties, total amount, and spatial distribution upon injection, such that mechanical heterogeneity is limited in the early stages of post-MI remodeling. This general concept is supported by previous results obtained with finite element simulations, which predict that biomaterial injections concentrated within the border zone (as opposed to uniformly delivered throughout the MI region) attenuate myocardial wall stress and promote efficient pump function [88].

STE has been previously used to discriminate between infarcted and contractile myocardium post-MI [89]. Moreover, many studies have shown the utility of quantifying global values of STE-derived strain and strain rate with good feasibility, reproducibility, and accuracy in clinical and large animal populations [64–72]. In accordance with these prior studies, we found significant reductions in global myocardial strain and strain rate post-MI. While global strain has been extensively quantified in the post-MI context, regional measurements in our study suggest that the initially antithetical changes in the MI and remote regions likely weaken the sensitivity and diagnostic strength of traditional global metrics of function. Furthermore, this study demonstrates that STE-derived myocardial strain combined with traditional echocardiography and Doppler-derived hemodynamic parameters can be used to compute a regional diastolic myocardial stiffness. While an analogous technique has been applied to aortic aneurysms [90], we are the first to

36

noninvasively quantify regional diastolic stiffness using STE in the context of post-MI remodeling.

2.5.5 Study Limitations

Several study limitations must be considered for careful interpretation of the obtained results. Firstly, all metrics of LV function are dependent on load. To that end, the findings from this study only account for patient-specific variance in hemodynamics through the estimation of LV pressure at end-diastole (PCWP) and an assumption of negligible LV pressure at the onset of diastole. Additionally, as with all echocardiographic techniques, successful quantification of myocardial strain via STE is highly dependent on image quality. To translate this technology into a clinical setting, one must consider that the ability to capture echocardiographic images of sufficient quality is markedly impaired in obese patients or patients with respiratory disorders. However, we expect that the clinical utility of the regional tracking of segmental strains will markedly increase as the underlying technology becomes more reproducible and reliable. Furthermore, these findings were for an anteroapical MI location in a porcine model and thus may not hold true with different MI locations, severity of myocardial ischemia, and/or across species. Finally, biomechanical changes were only assessed over 28 days post-MI in our study. Although this period has been shown to exhibit significant collagen deposition in a porcine model [91], care must be taken when extrapolating these findings into long-term effects given evidence that there are changes in LV strain and strain rate that continue through 1-3 months post-MI [26].

2.5.6 Conclusion

Post-MI remodeling induced progressive changes in LV biomechanics that manifest as regional differences in myocardial strain and strain rate over 28 days post-MI. For the first time, the utility of STE was extended in a large animal model to quantify regional diastolic myocardial stiffness in a serial fashion post-MI. Finally, this study identified the biphasic and at times opposing nature of regional changes in myocardial diastolic stiffness, which in turn is a likely contributing factor for a "feed forward" mechanism for adverse LV post-MI remodeling. Future therapeutic strategies that mitigate this significant regional stiffness gradient between the MI and adjacent viable myocardium may be a potential target for attenuating post-MI remodeling.

2.6   ACKNOWLEDGEMENTS

2.7   TABLES

Table 2.1: Speckle tracking echocardiography enables quantification of myocardial segmental strain.

	Baseline	**3 Days**	**14 Days**	**28 Days**
EF [%]	69.1 ± 0.8	49.4 ± 2.7*	37.8 ± 2.3*†	37.5 ± 3.4*†
LV EDV [mL]	37.2 ± 1.5	59.3 ± 5.1*	77.2 ± 6.5*†	83.6 ± 6.4*†
PCWP [mmHg]	7.6 ± 0.6	9.3 ± 0.6*	12.2 ± 0.9*†	13.9 ± 1.1*†

* $p<0.05$ vs. Respective Baseline Value, † $p<0.05$ vs. Respective 3 days Value, EF: ejection fraction, LV EDV: left ventricular end diastolic volume, PCWP: pulmonary capillary wedge pressure (n=8, one-way analysis of variance with *post hoc* LSD comparisons).

(A)

IVS: Interventricular septum   P: Posterior
AS: Anterior septum   A: Anterior

(B)
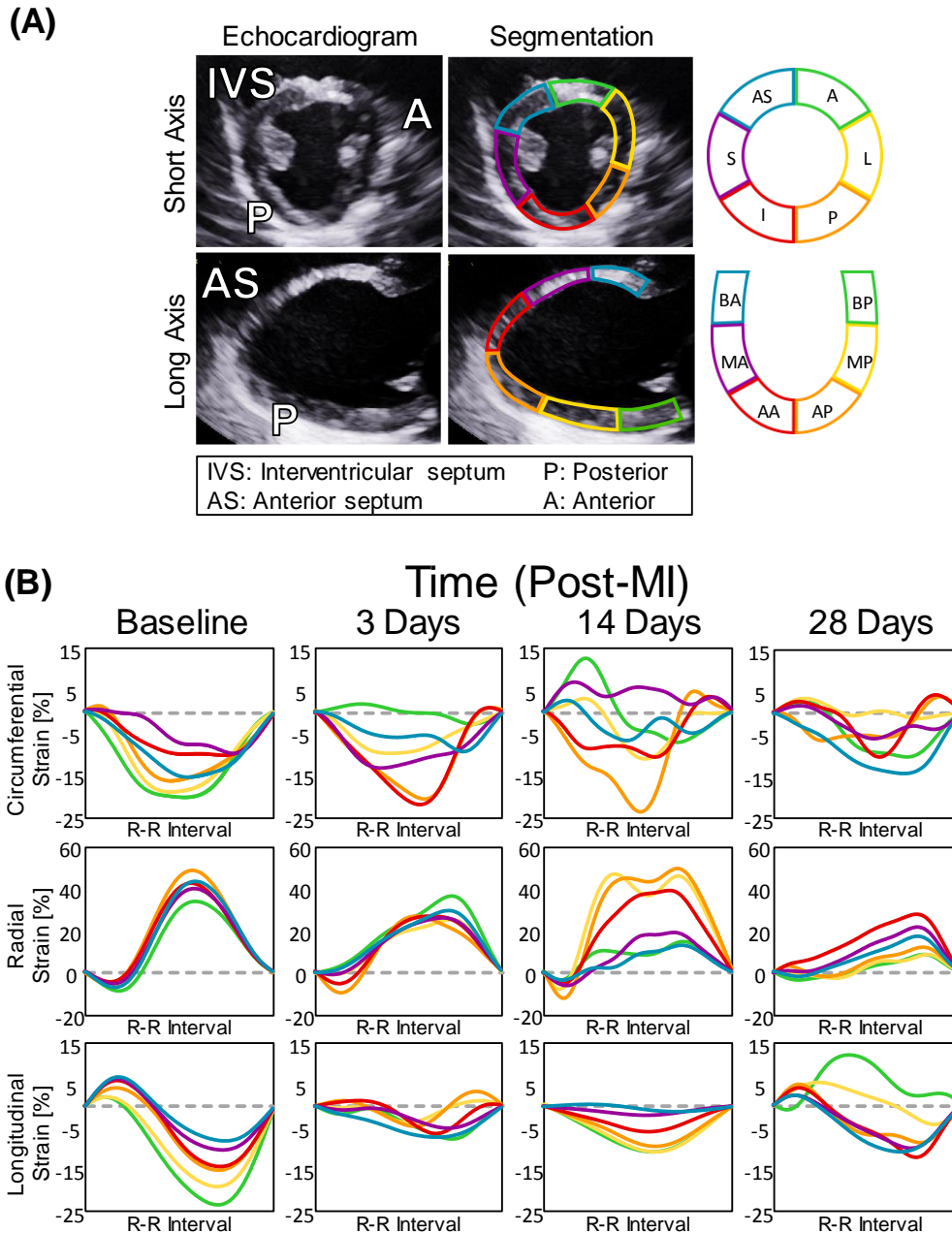
Figure 2.1: Speckle tracking echocardiography enables quantification of myocardial segmental strain.

(A) Representative echocardiographic images obtained 28 days post-MI (at end diastole) divided into six anatomical zones for speckle tracking. (B) Representative segmental strain curves of the LV mid-wall over one cardiac cycle at 28 days post-MI in the circumferential, radial, and longitudinal directions.
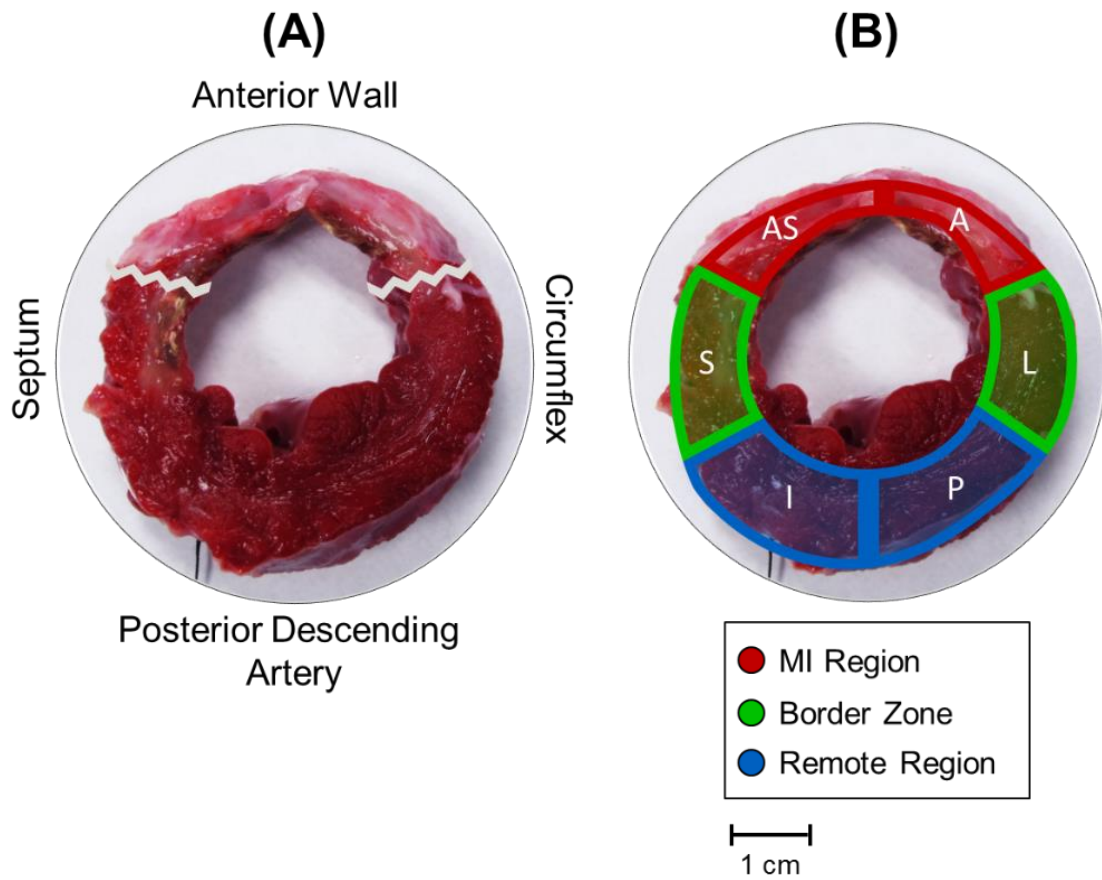
Figure 2.2: Definition of aggregate regions based on MI location
(A) Representative LV circumferential section cut across the central portion of the MI and stained with triphenyltetrazolium chloride shows the (B) agreement between designated aggregate MI region, border zone, and remote region at 28 days post-MI. The jagged line represents the edges of the MI region

ال،ارة للاستشارات

www.manaraa.com
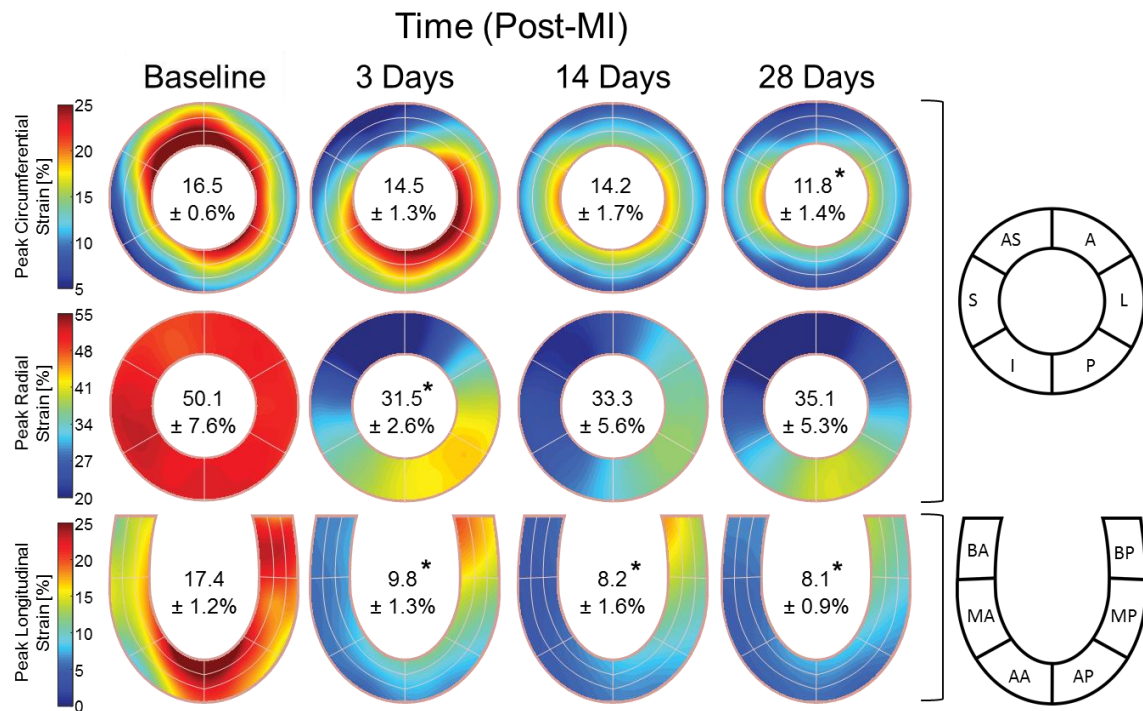
Figure 2.3: Peak myocardial strain
Spatial maps of the absolute value of peak myocardial segmental strain in the circumferential (top row), radial (middle row), and longitudinal (bottom row) directions at baseline and at three, 14, and 28 days post-MI. Inscribed values indicate the peak global strain reported as the mean absolute value ± standard error of the mean. * $p < 0.05$ vs. respective baseline value (n=8, one-way analysis of variance with post hoc LSD comparisons).
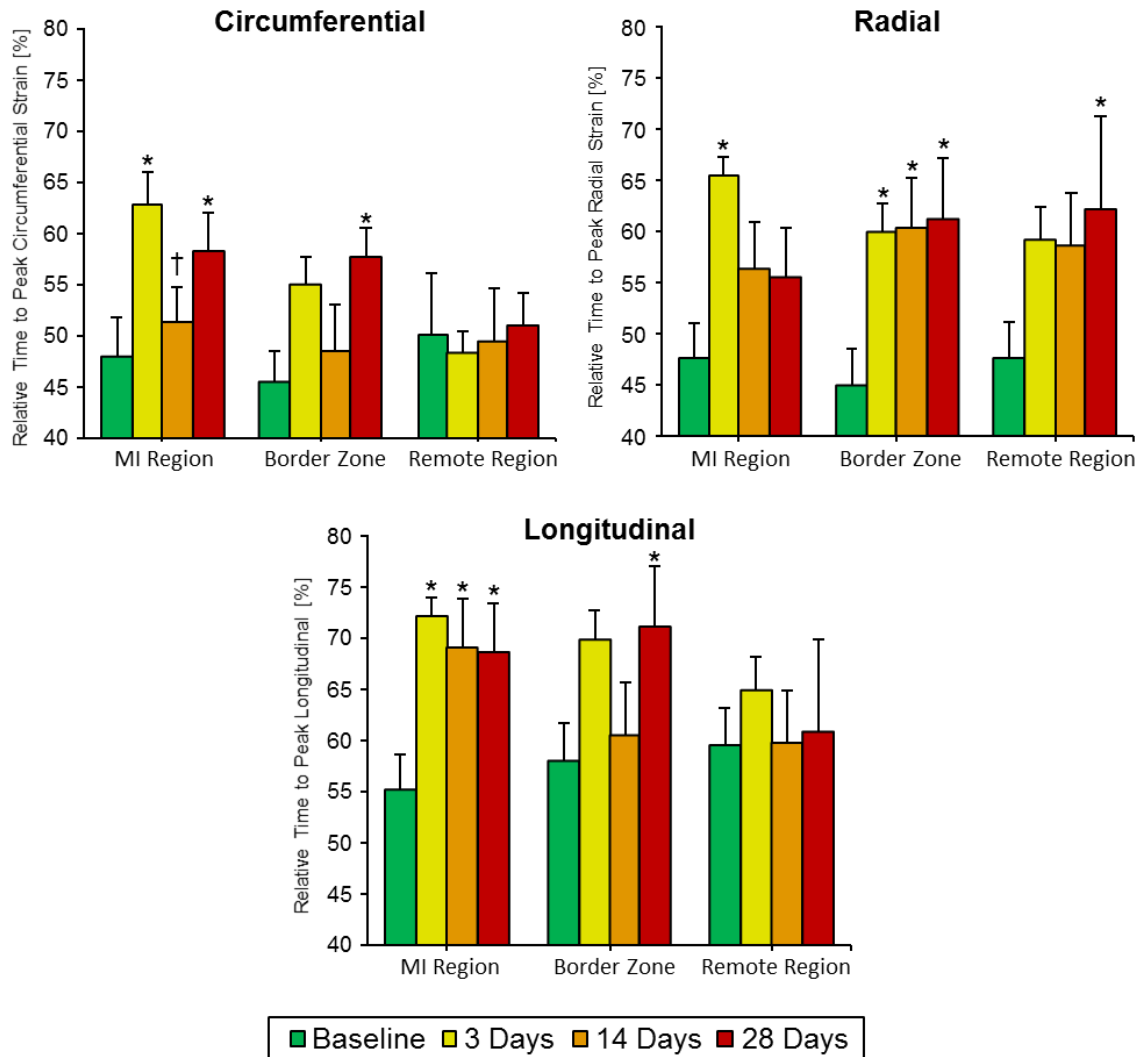
Figure 2.4: Relative time to peak myocardial strain
The relative time at which peak myocardial strain occurred for each region at baseline and at three, 14, and 28 days post-MI, with relative time defined as percent completion of one cardiac cycle; * $p<0.05$ vs. respective baseline value, † $p<0.05$ vs. respective three days value (n=8, one-way analysis of variance with *post hoc* LSD comparisons).
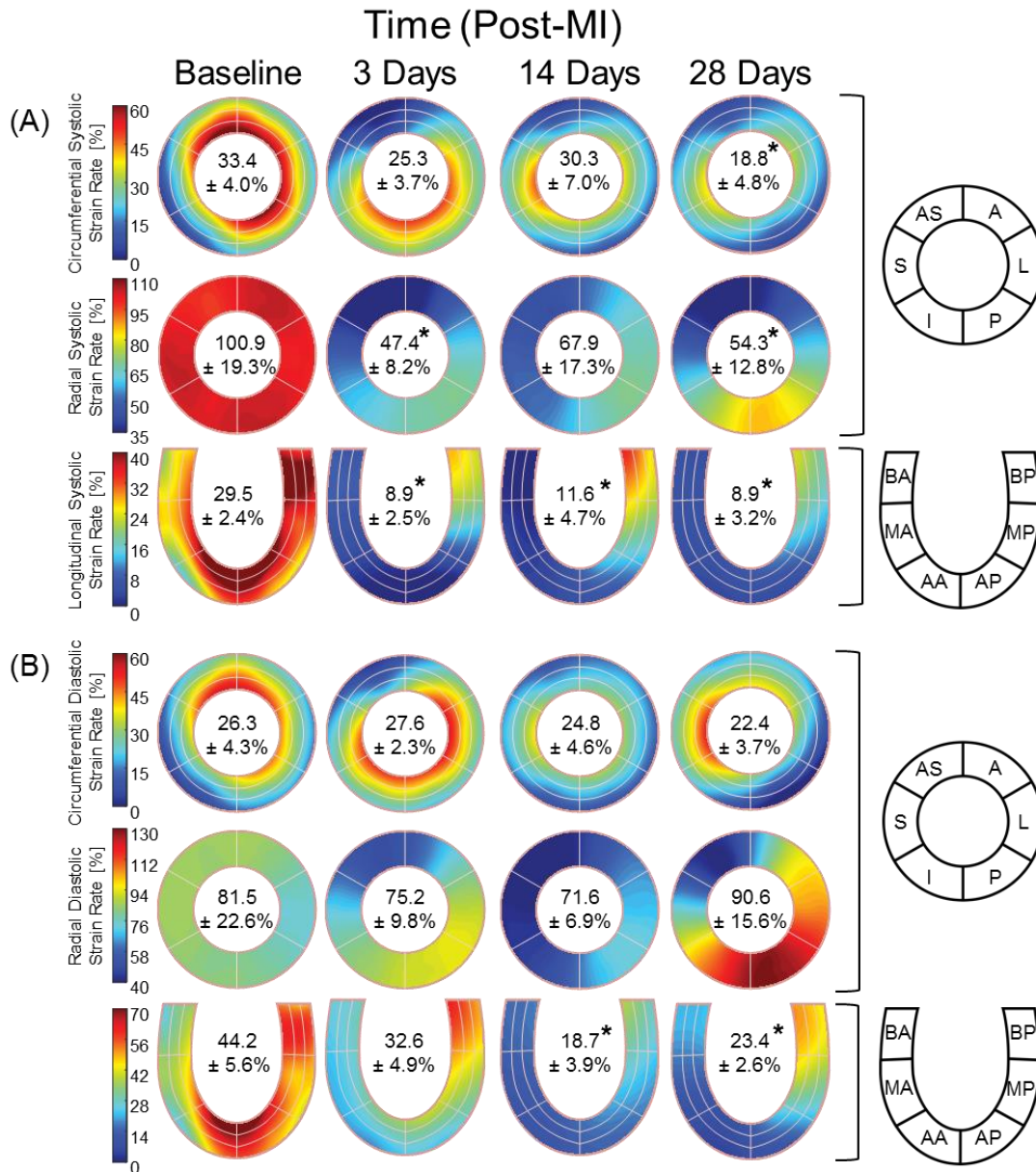
Figure 2.5: Phasic myocardial strain rate

Spatial maps of the absolute value of the (A) systolic and (B) diastolic myocardial segmental strain rates in the circumferential (top rows), radial (middle rows), and longitudinal (bottom rows) directions at baseline and at three, 14, and 28 days post-MI. Inscribed values indicate the global strain rate reported as the mean absolute value ± standard error of the mean. * $p<0.05$ vs. respective baseline value (n=8, one-way analysis of variance with *post hoc* LSD comparisons).
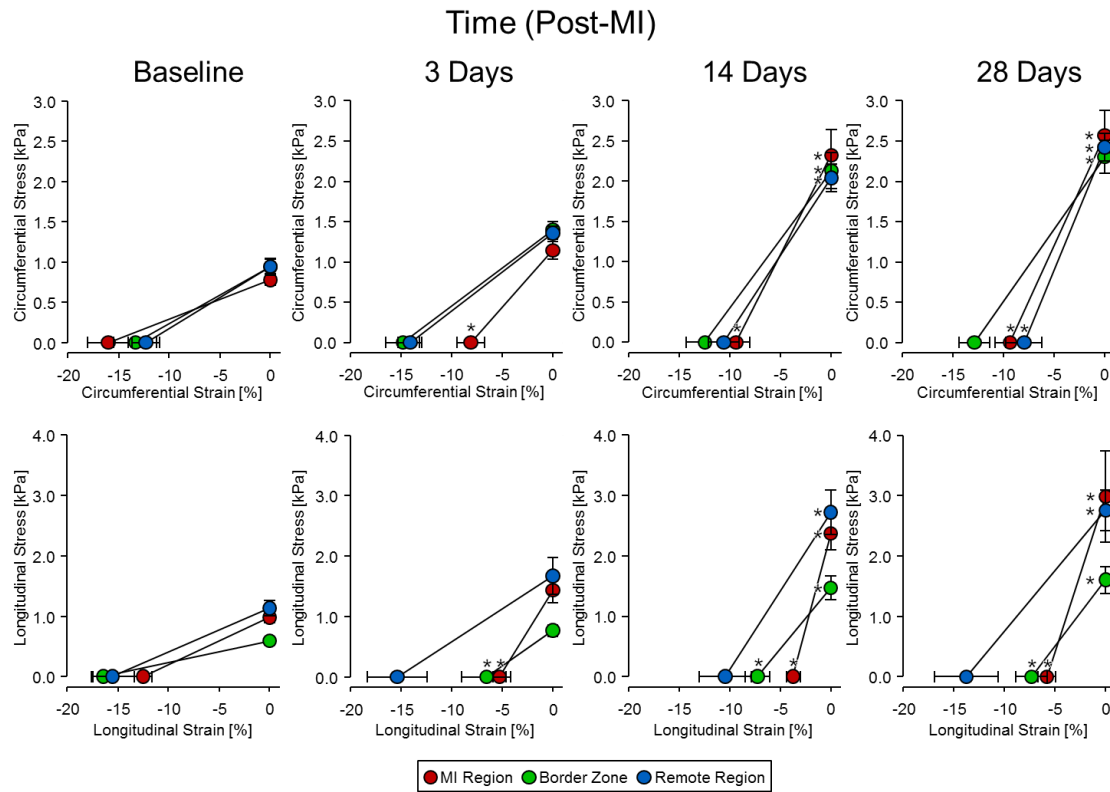
Figure 2.6: Stress-strain relations
Regional (MI region, border zone, and remote region) myocardial stress-strain relations were computed at early- and end-diastole in the circumferential and longitudinal directions at baseline and at three, 14, and 28 days post-MI. * $p<0.05$ vs. respective baseline stress or strain value (n=8, one-way analysis of variance with *post hoc* LSD comparisons).
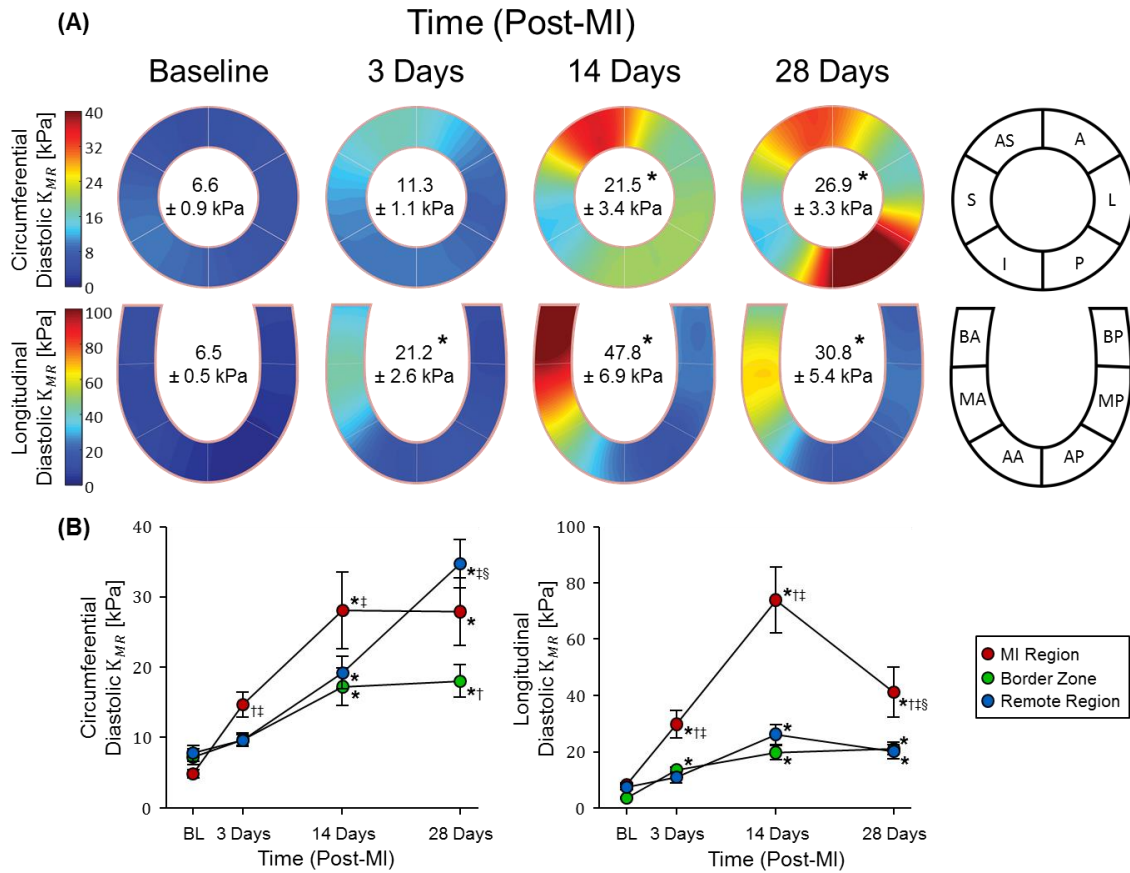
Figure 2.7: Diastolic myocardial stiffness
(A) Spatial maps of diastolic myocardial stiffness in the circumferential and longitudinal directions at baseline and at three, 14, and 28 days post-MI. Inscribed values indicate the myocardial stiffness reported as the mean value ± standard error of the mean. (B) Region-specific change in myocardial stiffness post-MI. * $p<0.05$ vs. respective baseline value, $\dagger$ $p<0.05$ vs. respective remote region value, $\ddagger$ $p<0.05$ vs. respective border zone value, $\S$ $p<0.05$ vs. respective 14-day post-MI value (n=8, two-way analysis of variance with *post hoc* LSD comparisons).

CHAPTER 3

CHANGES IN MYOCARDIAL MICROSTRUCTURE AND

MECHANICS WITH PROGRESSIVE LEFT VENTRICULAR

PRESSURE OVERLOAD [2]

---

[2] Torres W. M., Jacobs J., Doviak, H., Moore A., Freeburg L., Hoenes, A., Barlow S. C., Zile M. R., Shazly T., Spinale F. G. Changes in myocardial microstructure and mechanics with progressive left ventricular overload. To be submitted to *Circulation*.

3.1   ABSTRACT

Heart failure with preserved ejection fraction (HFpEF) secondary to left ventricular pressure overload (LVPO) is a leading cause of morbidity and mortality. Treatment options for HFpEF are limited by our poor understanding of disease phenotype and factors that underlie its progression. Our study seeks to assess the dynamic interplay between regional changes in myocardial geometry, microstructure, mechanical behavior, and mechanical properties that occur in response to progressive LVPO in a large animal model. LVPO was induced in mature pigs by progressive inflation of an implanted ascending aortic cuff for up to five weeks. Serial echocardiography was used to quantify left ventricle (LV) chamber stiffness and left atrial (LA) area, as well as regional myocardial strain and stiffness. Light microscopy and second harmonic imaging (SHG) were used to evaluate myocardial collagen content and microstructure. LVPO induced minimal perturbations in ejection fraction and peak systolic strains, but significant elevations in LV chamber stiffness, LA area, and regional myocardial stiffness. Analyses of myocardial collagen content and microstructure suggested that increased myocardial stiffness is promoted by not only an increase in collagen mass, but also a realignment of the collagen fibers and a reduction of their undulation. Myocardial microstructural and mechanical data were integrated to develop a novel index of local biomechanical adaptation to LVPO. Regression modeling suggest that this index, when obtained shortly after the onset of LVPO, is predictive of progressive increases in LV chamber stiffness. Our findings support the use of serial biomechanical analysis b to track the progression of HFpEF and present a translational method to stratify patient risk and assess the efficacy of pharmacological and therapeutic approaches.

3.2 INTRODUCTION

The rate and incidence of heart failure (HF) continues to escalate and recent statistics have identified this disease as the leading cause of morbidity and mortality – eclipsing all other chronic diseases.[30] While significant progress has been achieved in therapeutic retardation or elimination of other major illnesses such as cancer, these advancements have not been as forthcoming for HF. One contributory factor for this is that, unlike cancer which is classified by morphology, cell type, and molecular/genetic profiles, HF has been historically considered as a single entity fundamentally defined by symptomatology. However, it is also recognized that HF arises from distinctly different etiologies, which, in turn, have demonstrated distinctly different therapeutic responses and clinical outcomes.[31,32]

While the precise categorization of HF is continuously evolving, a generalized dichotomy can be made between patients presenting with or without significant left ventricular (LV) pump dysfunction. Specifically, if LV ejection fraction (EF) is below 45%, this is defined as HF with reduced EF (HFrEF), whereas if HF symptoms are present and EF is above this value, then it is defined as HF with a preserved EF (HFpEF). Using this HF classification scheme, it has been estimated that patients with these HF phenotypes are equally distributed.[31] Randomized clinical trials using combinatorial pharmacology or device-driven therapies have demonstrated significant improvement in HF progression and clinical outcomes in patients with HFrEF, but not in patients with HFpEF.[92–99] In addition, while the functional progression of HFrEF can be monitored by serial assessment of changes in EF, the natural history of HFpEF is not as easily tracked or well understood.[51,100]

49

As a result, advancements in the prognosis and strategic interventions for HFpEF have been met with challenges.

One rate limiting step in the research progress for HFpEF is a paucity of translationally relevant animal models that recapitulate key features of this HF phenotype.[101,102] Specifically, HFpEF can arise from progressive and prolonged LV pressure overload (LVPO) rather than from an acute pathological stimulus such as myocardial ischemia, which progresses to HFrEF.[103–106] In addition, a key component in the progression of HFpEF is the development of LV diastolic dysfunction, which requires sensitive measures of LV diastole and can be difficult to assess in a serial manner.[107,108] We have previously established a porcine model of progressive LVPO, which resulted in significant LV hypertrophy with stable EF, but with evidence for impaired diastolic function, consistent with the clinical phenotype of HFpEF.[109]

The overall goal of this study was to utilize this relevant pre-clinical model to parse out the relationship between the LV geometry, collagen microstructure, mechanical behavior, and mechanical properties in development of HFpEF. The central hypothesis of this study was that LV remodeling in response to LVPO is characterized by an increase in collagen mass and a change in the collagen microstructure. We posit that these changes will be the driving factor behind progressive changes in both LV chamber stiffness and myocardial mechanical properties. To that end, in the present study we employ a combinatorial approach of non-invasive imaging techniques along with an advanced optical analysis of the collagen microstructure to improve upon the current understanding of the mechanisms which give rise to the progression of HFpEF.

50

3.3 METHODS

The present study induced progressive LVPO in pigs for up to a 5 week period, over which regional myocardial strain and stiffness were quantified using speckle tracking echocardiography and, at the terminal time point, myocardial collagen content and microstructure using quantitative histomorphometry and second harmonic generation imaging.[7,57,61,110–113] These functional and serial results were then examined with a focus upon identifying factors that would contribute to and potentially predict changes in LV chamber stiffness, a hallmark of HFpEF progression.[47,50,109,114–119]

3.3.1 Aortic Cuff Placement

Yorkshire pigs (n=15, 15.8±0.6 kg, Hambone Farms, Orangeburg, SC) were anesthetized with isoflurane (3%/1.5L/min) and nitrous oxide (0.5L/min). Through a left thoracotomy, the pericardium was incised and a 12 mm inflatable silastic vascular cuff (Access Technologies, Skokie, IL) was secured around the supracoronary ascending aorta without inducing aortic constriction. A uniform length of silastic tubing was connected to a subcutaneous access port (Access Technologies, Skokie, IL) for subsequent serial hydraulic mediated expansion of the aortic cuff. The animals were allowed to recover for one week. Twelve age-matched referent control pigs were also used for comparative analyses. A prospective power analysis assuming a doubling of key response variables relative to the subject-matched baseline value and a standard error of measurement of 40% yielded a minimum study power of 0.80 for all experimental groups. All animals were treated and cared for in accordance with the National Institutes of Health *Guide for the Care and Use of Laboratory Animals* (*Eighth Edition*. Washington, DC: 2011) and all

51

experimental protocols were approved by Institutional Animal Care and Use Committees at the University of South Carolina.

3.3.2   Progressive Induction of LVPO

Following the one-week recovery period, the cuff was inflated through the access port (via 0.45 mL glycerol) to achieve a specific target gradient of 75 mmHg across the cuff and induce LVPO. At weekly intervals thereafter, the cuff was further inflated (0.25 mL increments) to cause a stepwise increase in the pressure gradient (25 mmHg increase/inflation). At either four (n=7) or five weeks (n=7) post-PO, the animals were again anesthetized (5% isoflurane) and the LV was harvested.

3.3.3   Standard Echocardiography

Standard echocardiography was performed weekly throughout the study (GE Vivid E9 with XDclear Ultrasound System: M5S (1.5-4.6 MHz) transducer probe). Left ventricular and left atrial dimensions and function were assessed by two-dimensional and M-mode echocardiographic studies. The transthoracic images were acquired from a right parasternal approach as well as an abdominal/sub xyphoid approach. The LV was imaged in the short- and long-axes. The short-axis views were taken at the level of the papillary muscles. End-diastolic volume (EDV), end-systolic volume (ESV), and EF were calculated using the biplane method of disks. Left atrial (LA) area was determined from the anteroposterior dimensions acquired from the parasternal long-axis view. Additionally, wall thickness and LV internal dimension were collected at early- and end-diastole for each of the six conventional echocardiogram segments of the LV in the parasternal long-axis and papillary level short-axis. Finally, following the convention established by Devereux and colleagues, LV mass was estimated from M-mode measurements.[4] Echocardiographic

studies under identical sedation/acquisition conditions were performed at weekly intervals until the terminal timepoint.

3.3.4 Definition of Normal Range for Left Ventricular mass

LV mass measurements (computed as described above) were collected from a cohort of 100 male Yorkshire pigs (body weights ranging from 13.4 kg to 33.1 kg) that were part of this laboratory's prior studies completed between 2012-2017. A normogram for LV mass as a function of body weight was generated by fitting a linear regression through the resultant data set with a 95% confidence interval. This normogram provides a basis to assess pressure-induced elevations in LV mass with due account of normal growth.

3.3.5 Terminal Evaluation of Global and Regional Left Ventricular Function

In a subset of referent control (n=5) and banded (n=5) pigs, LV pressure and dimensions were obtained. Briefly, the pigs were anesthetized with fentanyl (50 µg) and propofol (100 mg), and a cardiac catheter introducer with a side-arm (9F, Medtronic, Minneapolis, MN) connected to a pressure transducer was placed in the right carotid artery and advanced to the ascending aorta. After which, a multi-lumened thermodilution catheter (7.5F, Baxter Healthcare Corp., Irvine, CA) was advanced through the right external jugular vein and positioned in the pulmonary artery. Pulmonary capillary wedge pressure, a surrogate for end-diastolic pressure (P_{ED}), was measured using conventional methods.[120] Afterwards, a microtipped transducer (7.5F, Millar Instruments Inc., Houston, TX) was placed in the LV through a small apical stab wound. Pressure data was recorded at a sampling frequency of 100 Hz and digitized (Ponemah, Harvard Bioscience Inc., Holliston, MA). Following the placement of the instrumentation, an ultrasound transducer (GE Vivid E9 with XDclear Ultrasound System: M5S (1.5-4.6 MHz) transducer probe) was positioned

for transthoracic imaging of the LV short-axis and measurement of continuous LV volume and wall thickness.[121] Steady-state LV function was determined with simultaneous acquisition of pressure and echocardiographic data with the ventilator temporarily suspended in order to prevent respiratory artifact. Following steady-state measurements, LV preload was altered with sequential occlusion and release of the inferior vena cava with vascular ligature. Again, simultaneous pressure and echocardiographic data were collected during occlusion and release.

After data acquisition was complete, the digitized pressure and LV dimension data were aligned using the R-wave of the simultaneously recorded ECG from each modality. The aligned pressure and dimension data for the steady-state and caval occlusion cardiac cycles were used to determine the regional myocardial stiffness constant and LV chamber stiffness, respectively, using the methods derived by Mirsky and Pasipoularides.[21,22]

3.3.6 Non-Invasive Estimation of End-Diastolic Pressure and Chamber Stiffness

While direct measurements of LV pressure and chamber stiffness via cardiac catheterization have been accepted as the gold standard, non-invasive estimates of these response variables were necessary in order to track the progression of disease and LV remodeling. Accordingly, obtained measurements of pulmonary capillary wedge pressure and temporally-matched LA area measurements in a subset of referent control (n=5) and banded (n=8) animals were used to identify an expression for non-invasive estimation of end-diastolic pressure, specifically $P_{ED} = 1.88e^{0.16(LA\ area)}$ (R^2=0.91). After applying this regression-based non-invasive estimation of P_{ED} to the entire study cohort, a non-invasive surrogate of LV chamber stiffness (K_C^*) was computed as the ratio between P_{ED} and EDV.[122]

54

3.3.7 Speckle Tracking Echocardiography

Three consecutive digital loops of the two-dimensional echocardiography for the long-axis and short-axis were stored on a hard disk and transferred to a workstation (EchoPac, Vingmed, General Electric) for post-processing. For each echocardiographic digital loop, a region of interest (ROI) was defined at the onset of the R-wave by manually tracing the endocardial and epicardial borders. The ROI was then discretized with a spatial mesh of acoustic clusters to be tracked on a frame-to-frame basis throughout the cardiac cycle (R-R interval).[7] The end of systole was defined as the point at which the LV cross-sectional area was at a minimum. After the semi-automated grouping of acoustic clusters in accordance with six predetermined anatomical locations, regional tracking quality was assessed, and the ROI was manually adjusted by the operator to improve tracking quality where necessary. Successful tracking of the ROI allows for the definition of segmental lengths, which are computed at end diastole (L_0) and continuously throughout the cardiac cycle (L). Local segmental strains (ε) and strain rates (γ) are then computed as:

$$\varepsilon = \frac{L - L_0}{L_0} = \frac{\Delta L}{L_0} \quad (3.1)$$

$$\gamma = \frac{(\Delta L / \Delta t)}{L_0} \quad (3.2)$$

where Δt is the relative time in the cardiac cycle. Peak strain and diastolic strain rate were quantified in the two normal directions, circumferential (short-axis) and longitudinal (long-axis), at the endocardial, mid-wall, and epicardial surfaces. Global strain values were calculated from the total length of all six segments. Obtained segmental strain and strain rate data were assessed for intra-observer variance by calculating the intra-class correlation coefficient for a single operator under the assumption that systematic differences are

55

relevant. The intra-class correlation coefficient for all measures of strain and strain rate ranged from 0.94 to 0.99.

3.3.8 Mean Wall Stresses

We modified a thick-walled ellipsoidal model proposed by Janz to compute mean wall stresses.[24] The mean circumferential wall stress (σ_C) was computed as:

$$\sigma_C = \frac{Pr^2}{2t(r+\frac{t}{2})} \quad (3.3)$$

where (r) is the inner radius, (t) is the wall thickness, and (P) is the LV pressure. For the purposes of this study, (P) was assumed to equal zero at the onset on diastole and the PCWP at end-diastole.

The mean longitudinal wall stress (σ_L) was computed as:

$$\sigma_L = \frac{Pr^2}{2t(sin\theta)(r+\frac{t(sin\theta)}{2})} \quad (3.4)$$

where (Φ) is the angle between the normal vector from the endocardium at the ROI and the axis of revolution in the truncated ellipsoid model.

3.3.9 Regional Diastolic Myocardial Stiffness

Obtained values for mean wall stresses and segmental strains at the onset of diastole and end-diastole enabled calculation of regional diastolic myocardial stiffness in both the circumferential and longitudinal directions. The slope of the line between these two points in the stress-strain plane, developed in either the circumferential or longitudinal direction and referenced to the defined anatomical locations, was used to compute the regional diastolic myocardial stiffness (K_{MR}) as:

$$\kappa_{MR} = \frac{\sigma_{ED}}{|\varepsilon_{Do}|} \quad (3.5)$$

56

where σ_{ED} and ε_{D0} are the end diastolic mean wall stress and segmental strain at the onset of diastole, respectively.

3.3.10 Second-Harmonic Generation Imaging

Upon terminal heart harvest, a 1-inch thick bisection of the left ventricle was fixed in 10% formalin – preserving the native orientation and configuration of the collagen fibers – and refrigerated for histological evaluation. The LV lateral free-wall myocardium was later sectioned into thin, 200 µm sections using a vibratome and placed on the motorized stage of a multiphoton microscope (Leica TCS SP8 MP, Leica Microsystems). Short-pulsed infrared lasers were used to create non-linear polarization effects in the form of second-harmonic generation (SHG) signals at a magnification of 25x. Images were acquired for a fixed sample area of 0.2 mm^2 at depth intervals of 1.5 µm.

3.3.11 Automated Tracing of Individual Collagen Fibers

Two-dimensional images acquired from the multiphoton microscope were converted to 8-bit greyscale and virtually stacked in three-dimensions using the Amira software package.[123] For the fully-automated tracing of individual collagen fibers, we modified the previously described techniques developed for electron tomography,[124,125] which have been packaged into the XTracing filament detection extension available for Amira. In brief, this tracing algorithm consists of two main steps: template matching and a line search approach. A correlation field is generated by computing the cross-correlation of the voxels in the three-dimensional stack with a cylindrical template. This cylindrical template mimics a short collagen fiber segment with a mask radius of 5 µm and a length of 20 µm. The correlation was computed for each voxel on a NVIDIA Quadro M2000 graphics processing unit. The line search approach was then used to iteratively identify the

voxels on the centerline of each collagen fiber. From an initial seed point, a search cone spanning 20 µm and 45 degrees was used to identify candidate points that were scored on the basis of continuity, curvature, and deviations from the orientation field. The line search stops when the search cone fails to identify candidate points with scores above the minimum threshold.

3.3.12 Characterization of the Collagen Structure

Each collagen fiber was evaluated with respect to orientation and undulation. Two angles were used to define the fiber orientation. The azimuthal angle (φ) refers to angle from the positive radial axis of the fiber's projection on the longitudinal-radial plane, where $\varphi=0°$ is then the radial direction. The elevation angle (ϑ) refers to the angle from the positive circumferential axis of the fiber's projection on the circumferential-longitudinal plane, where $\vartheta=0°$ and $\vartheta=90°$ correspond with the circumferential and longitudinal directions, respectively. Fiber undulation (u) is defined as the ratio between the path length (l_p) and the end-to-end length (l_e) of a given fiber.

$$u = \frac{l_p}{l_e} \qquad (3.6)$$

3.3.13 Collagen Content by Light Microscopy

LV septal and lateral sections were stained with picrosirius red (PSR) and viewed with polarized light at a magnification of 40x. Five fields were chosen at random from the mid-myocardium. Fields with large blood vessels were excluded from the analysis. Collagen volume fraction (CVF) was calculated as the area stained by PSR divided by the total area of interest using ImageJ software.[126]

3.3.14 Statistical Analysis

Data are reported as the mean ± standard error of the mean. Comparative analyses were performed using a one-way analysis of variance followed by pair-wise comparisons using the least significant difference *post hoc* study. For the assessment of the relative change from baseline, a t-test was performed whereby significance of the transformed data were determined using a null hypothesis of a zero-mean value. For SHG collagen fiber characterization, at each timepoint, all values of φ, ϑ, and u were pooled and binned into 100 equally sized bins. The resulting frequency distributions were subjected to a Kruskal-Wallis one-way analysis of variance for non-parametric comparisons across different timepoints. A multiple linear regression model with inputs derived at one-week post-PO was used to predict the relative change in K_C^* at two-weeks, three-weeks, four-weeks, and five-weeks post-PO, and the p-value and t-statistic were calculated for each of the input variables. A Spearman's rank correlation analysis was used to interrelate experimental response variables at four- and five-weeks post-PO. All statistical analyses were performed with SPSS software (version 24.0, SPSS Inc) or MATLAB (version R2018a, The MathWorks Inc). A p-value of less than 0.05 was considered statistically significant.

3.4   RESULTS

3.4.1   Left Ventricular Geometry and Systolic Function

The progressive hydraulic inflation of the aortic cuff resulted in significant hypertrophy of the LV as compared to an age-matched referent control LV as a result of the narrowing of the aortic lumen (**Figure 3.1A**). This hypertrophic response, growth that

59

superseded that which can be expected due to normal growth, occurred in a time-dependent fashion over five weeks (**Figure 3.1B**). In contrast, the ratio of LV EDV to body weight was preserved and systolic function, assessed by LV ejection fraction, was modestly increased relative to baseline at both four- and five-weeks post-PO. Significant increases in the LV mass/volume ratio and LA area were observed. The effects of PO on LV function and geometry are summarized in **Figure 3.2**.

3.4.2   Left Ventricular Diastolic Function

Following established convention, chamber stiffness was determined from pressure-volume relations at the four- or five-week post-PO terminal timepoint and age-matched referent control pigs (**Figure 3.3A**). Significant increases in chamber stiffness were observed in the banded animals (**Figure 3.3B**). Similarly, increases in the previously-defined non-invasive surrogate for chamber stiffness (K_C^*) were observed in the banded animals relative to baseline observations by one-week post-PO and progressive increases through five-weeks post-PO. Post-processing via Pearson correlation analysis yielded significant correlation between these two measurements of chamber stiffness ($\rho=0.75$, $p<0.05$). As such, for the duration of the results and discussion, we will use K_C^* as the predominant measure of LV chamber stiffness because it can be measured in a serial manner.

3.4.3   Left Ventricular Collagen Content and Organization

Photomicrographs of picrosirius red-stained slides enabled quantification of myocardial collagen content (**Figure 3.4**). CVF was indistinguishable at four- versus five-weeks post-PO, but both were more than doubled compared to the referent control value. The increase in collagen content was coupled with significant changes in collagen fiber

60

microstructure (**Figure 3.5**). In all three layers of the LV, observed fiber undulation distributions indicated a significantly higher coincidence of less wavy fibers at five-weeks post-PO compared to referent control (**Figure 3.5B**). In terms of ECM organization, collagen fiber angle distributions on the circumferential-longitudinal plane in the epicardium and endocardium were significantly shifted towards the circumferential axis by five weeks and four weeks post-PO, respectively (**Figure 3.5C**). Collagen fiber angle distributions on the radial-longitudinal plane were mostly preserved during the five weeks of this study (**Figure 3.5D**).

3.4.4   Assessment of Biomechanical Behavior and Properties

STE was used to serially track LVPO-induced changes in regional peak strain, diastolic strain rate, and diastolic myocardial stiffness (**Figure 3.6**). Peak strain, taken as an index of regional systolic function, is generally preserved in the longitudinal direction and moderately elevated in the circumferential direction by one-week post-PO. Regional diastolic function, assessed via diastolic strain rate, was found to be impaired in the longitudinal direction with a reduction relative to baseline values observed in the endocardium and mid-myocardium by three-weeks or four-weeks post-PO, respectively. In contrast, circumferential diastolic strain rate was mostly preserved. LVPO was found to have a significant effect on diastolic myocardial stiffness in both the circumferential and longitudinal directions. Regional measurements of diastolic myocardial stiffness were validated against the measurements obtained from the invasive catheterization measurements defined above and a significant correlation between the two was observed ($\rho=0.70$, $p<0.05$). The global diastolic myocardial stiffness, taken as the average stiffness computed among all defined regions, significantly increased by four-weeks post-PO in the

61

circumferential direction and by two-weeks post-PO in the longitudinal direction, with progressive increases subsequently occurring in both directions.

3.4.5   Correlation Between Regional Composition and Biomechanical Behavior and Properties

A correlation matrix was developed to relate the relative change in biomechanical response metrics and geometrical, compositional, and microstructural features of the myocardium at the terminal study timepoints (**Figure 3.7**). Surprisingly, subject-specific changes in wall thickness and collagen content did not significantly correlate with the changes in biomechanical response metrics, while ECM microstructure did so in an intuitive manner. Specifically, a reduction in fiber undulation ($u{\rightarrow}1$) was correlated with increased myocardial stiffness in all three layers of the LV. Furthermore, an inverse correlation was observed between the elevation angle and myocardial stiffness – linking a preferential fiber orientation towards the circumferential axis ($\vartheta{\rightarrow}0°$) to higher circumferential myocardial stiffness.

3.4.6   Predicting Changes in LV Chamber Stiffness

To develop an index of biomechanical adaptation of the myocardium to LVPO, we examined the subject-specific relationship between regional changes in diastolic myocardial stiffness and wall thickness. Specifically, we computed the slope of a linear regression in the circumferential stiffness-thickness plane ($\partial K_{MR}/\partial H$) developed with measurements from the six defined myocardial regions at one-week post-PO (**Figure 3.8A**). The observed inverse relationship, when computed for an individual subject, is posited as an index of adaptation in the sense that the more negative the slope, the more the myocardium has mechanically-compensated for increased wall thickness such that the

62

concomitant increase in K_C^* is less severe. This index of adaptivity was combined with the measurement of the current chamber stiffness ($K_{C,1-week}^*$) in a multiple linear regression model of the form:

$$K_{C,pred.}^* = a\frac{\partial K_{MR}}{\partial H} + b\left(K_{C,1-week}^*\right) + c(T) + d, \qquad (3.7)$$

where a, b, c, and d were fitting parameters and T was the time (in days) of the echocardiographic analysis after the initial placement of the aortic cuff. A post-hoc Pearson correlation analysis of the predicted change in chamber stiffness versus the experimentally measured result demonstrates a strong correlation between the two numbers (**Figure 3.8B**) (ρ=0.75, R^2=0.57, p<0.05). After the determination of the t-statistic for each of the four fitting coefficients, all were deemed to be statistically significant with a significance level of 5% (0.05).

3.5   DISCUSSION

3.5.1   Study Overview

The clinical syndrome of HFpEF burdens over three million patients in the United States alone and carries a five-year mortality rate of approximately 50%.[30,31,127] While there are viable pharmacological and therapeutic options available for those suffering from HFrEF, HFpEF treatments are limited by our poor understanding of disease phenotype, etiology, and progression.[51,92–100] The present study seeks to address this knowledge gap with a series of regional measurements of myocardial mechanics and microstructure in a porcine model of LVPO with retained systolic function. Using a combination of non-invasive serial measurements and *ex-vivo* analysis, the significant and noteworthy findings

63

from this study were three-fold. First, our results show that in addition to the expected increase in LV K_C^*, progressive changes in regional diastolic myocardial stiffness occur over five-weeks post-PO and provide a promising basis for improved clinical phenotyping of HFpEF. Second, elevated myocardial stiffness following LVPO is modulated by not only increased collagen content, but also changes in collagen fiber alignment and undulation. Third, through pig-specific analysis of regional changes in myocardial stiffness and wall thickness shortly following the onset of LVPO, we have identified a novel method to predict the extent of adverse LV chamber stiffening observed at later times post-PO. Thus, using a pre-clinical model we have shown the viability of serial biomechanical analysis as a basis to track the progression of HFpEF and present a translational method to stratify patient risk and assess the efficacy of pharmacological and therapeutic approaches.

3.5.2 Serial Tracking of Myocardial Biomechanics and Mechanical Properties

While the progression of HFpEF can be difficult to assess and track in a clinical setting, this animal model resulted in LV hypertrophy and hallmark characteristics of HFpEF in accord with previous studies.[109] From a biomechanical perspective, hypertrophy is the primary adaptive response of the myocardium to LVPO that mitigates the concomitant increase in wall stress.[128,129] Partially as a result of hypertrophy, progressive and significant elevations in diastolic K_C^* also occur over the time course of this study – again falling in line with a multitude of prior studies.[47,109,114,115,130,131] However, a comparison of late study time points (four- versus five-weeks post-PO) suggests that structural stiffness elevations are not simply governed by the addition of myocardial mass, but also the local mechanical stiffening of the myocardium itself. While the co-dependence of aberrant LV structural mechanics on both myocardial geometry and mechanical

64

properties is expected in all modes of HF, our results provide novel directional and regional detail on PO-induced elevations in diastolic myocardial stiffness (K_{MR}) and, importantly, inform temporal relation to elevations in K_C^*.[18,109,130,132,133] Despite the substantial changes in geometry, K_{MR}, and K_C^*, baseline peak strain and diastolic strain rate were largely retained. While there are a number of recent clinical studies which suggest that HFpEF is marked by a reduction of global longitudinal strain, this study (along with others) shows modest, if any, early changes in regional or global strain and diastolic strain rate. This finding suggests that global longitudinal strain values may be used to sub-classify HFpEF in the early stages of disease progession.[111,134–137]

3.5.3   Microstructural changes with LVPO

A consensus has emerged that the extracellular matrix (ECM) is extensively altered in the case of HFpEF secondary to LVPO.[138] These changes, primarily excessive ECM deposition by fibroblasts and changes in the relative balance between matrix metalloproteinases (MMPs) and the tissue inhibitors of the MMPs, are not readily reversible and contribute to impaired diastolic function.[138–142] This excessive ECM deposition, most notably increased collagen content, has been associated with the progressive stiffening of the LV and myocardium.[143–146] While we too observe LVPO-induced increases in CVF, correlation analyses suggest that changes in collagen fiber microstructure further modulate myocardial stiffness at later post-PO time points. As first established in the context of vascular mechanics, the inherent undulation of tissue-embedded collagen fibers implies a gradual contribution to load-bearing under increasing tension.[147] Likewise in the myocardium, a collagen fiber with relatively less undulation will be recruited to load-bearing at relatively lower loads (pressure), and thus lead to

65

increased K_{MR}. Our regional analysis indeed showed correlation between the reductions in fiber undulation and increases in K_{MR}. We posit that in the cycle of degradation and synthesis of collagen that occurs secondary to LVPO, the newly deposited collagen is embedded in the ECM under a higher degree of tension due to the elevated intraventricular pressure, which in turn reduces mean undulation and increases passive stiffness. We also show significant collagen fiber realignment concordant with disease progression. Much like previously reported findings of the infarcted myocardium, we observe that LVPO-induced hypertrophy is associated with an increased circumferential alignment of collagen fibers.[34] Taken together, these findings suggest that changes in fiber microstructure and alignment contribute to the recorded elevations in both circumferential and longitudinal K_{MR}.

3.5.4   Early Stratification of Subject-Specific Risk

It is accepted that soft tissue growth and remodeling are adaptive responses to cope with sustained changes in the local mechanical environment (i.e. stresses and strains) of mechanosensitive cells.[148–151] In 1995, Fung proposed a kinematic mass-stress relationship with the fundamental idea that every biological tissue has mechanisms by which to maintain a certain homeostatic stress state.[152] Thus, elevations in stress (possibly due to increased loading) would result in a compensatory increase in mass, while reductions in stress would result in the opposite – effectively restoring the tissue to its native homeostatic stress state. While modulation of growth facilitates the maintenance of the local homeostatic stress state, we posit that in an optimally adaptive tissue, local changes in mass must also be coupled with proportionally opposing changes in local stiffness so as to maintain structural compliance. As it applies to the present study, at one-week post-PO, we

66

observed that local wall thickening coincides with relatively less local stiffening (or even reductions in local stiffness) throughout the myocardium. Based on this notion of optimal adaptation, we take the degree to which an inverse thickening-stiffening relation is manifest to reflect the overall LV adaptive capacity of the individual subject. We defined a related index of biomechanical adaptation and showed that it, along with K_C^* also obtained at this early time point, can be used to predict subsequent elevations in K_C^* (**Figure 3.7**). Though it does little to address the underlying mechanisms, the proposed model may prove to be a clinically-relevant means to predict an individual patient's progression to HFpEF and therefore may influence clinical decision making in regard to disease prevention or management.[50,116–119] Furthermore, these findings give rise to a potential target for future studies as we seek to understand the epidemiological mechanisms which drive the varying degrees of biomechanical adaptive capacity on a subject-to-subject basis.

3.5.5   Study Limitations and Summary

For the first time, a serial characterization of myocardial mechanics and the organization/configuration of collagen within the ECM has been performed in a large animal model of LVPO. Furthermore, we present a novel mechanics-based method to predict the subject-specific severity of LV chamber stiffening, a central component of the HFpEF phenotype. However, several study limitations should be considered upon evaluation of our conclusions. Firstly, although the porcine model employed in our study enabled unique measurements with potential to advance the phenotyping of HFpEF, this animal model does not emulate any of the co-morbidities typically observed in patients with HFpEF (i.e. metabolic or renal dysfunction). Additionally, while the indices of diastolic dysfunction (i.e. LA area, LV chamber stiffness) suggest that these animals are

on a trajectory to HFpEF, the study was completed prior to a robust symptomatic development of HFpEF. Finally, while this study provides a promising method to predict HFpEF progression based on early observations of LV biomechanics, we did not explore the extent to which our results/predictions would vary in the context of a therapeutic intervention. Future studies in a clinical setting would be needed to further validate our findings and importantly evaluate the translational potential of using early changes in LV biomechanics following the onset of LVPO to predict those patients at greatest risk for the development and progression of HFpEF.

3.6   ACKNOWLEDGEMENTS
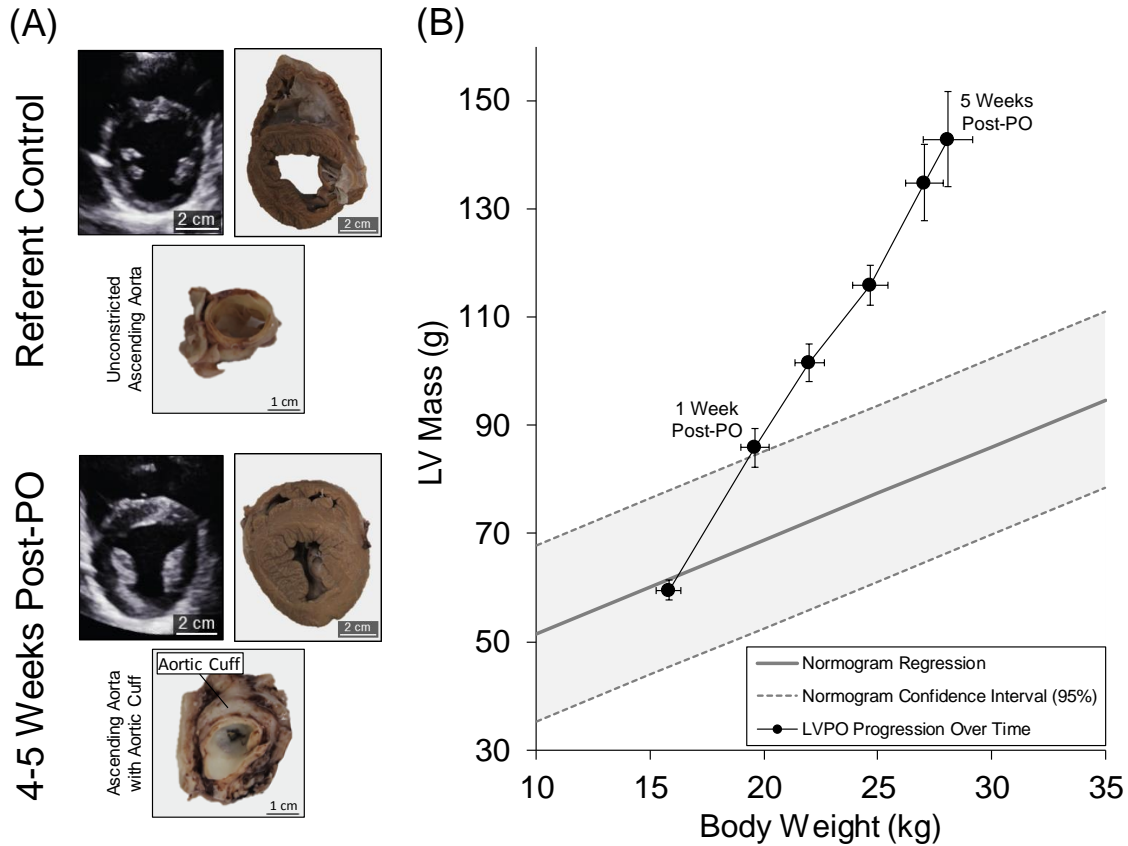
Figure 3.1: Pressure overload-induced hypertrophy of the LV
(A) Representative transthoracic echocardiographic views of the LV short-axis at the level of the papillary muscle along with preserved bisections of the intact ventricles and ascending aorta for both study groups. A clear and obvious thickening of the LV occurred as a result of LVPO. The aortic cuff significantly reduced the cross-sectional area of the aortic lumen. (B) LV mass obtained at baseline and over five-weeks post-PO superimposed on a normogram of LV mass relative to body weight. The observed increase in LV mass indicates a pressure-induced hypertrophic response. (BL – three-weeks post-PO: n=15; four-weeks post-PO: n=14; five-weeks post-PO: n=7)

69

www.manaraa.com
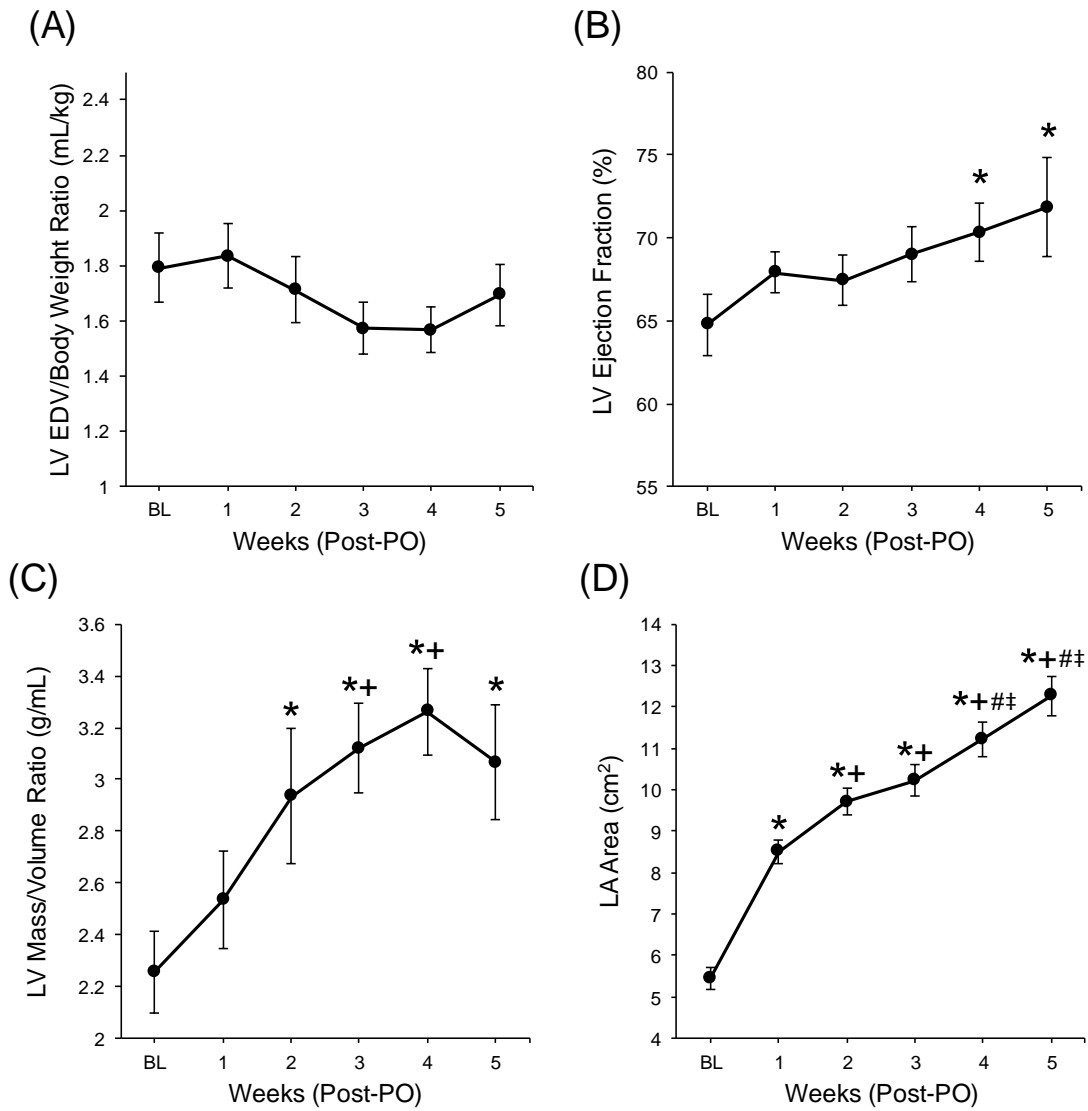
Figure 3.2: Echocardiographic indices of the progression to HFpEF.
(A) Baseline values of LV end-diastolic volume/body weight ratio, (B) LV ejection fraction, (C) LV mass/volume ratio were largely maintained over the study period, and (D) LA Area progressively increased over five-weeks post-PO. * $p<0.05$ vs. baseline value, [+] $p<0.05$ vs. one-week value, [#] $p<0.05$ vs. two-weeks value, [‡] $p<0.05$ vs. three-weeks value. (BL – three-weeks post-PO: n=15; four-weeks post-PO: n=14; five-weeks post-PO: n=7)

70
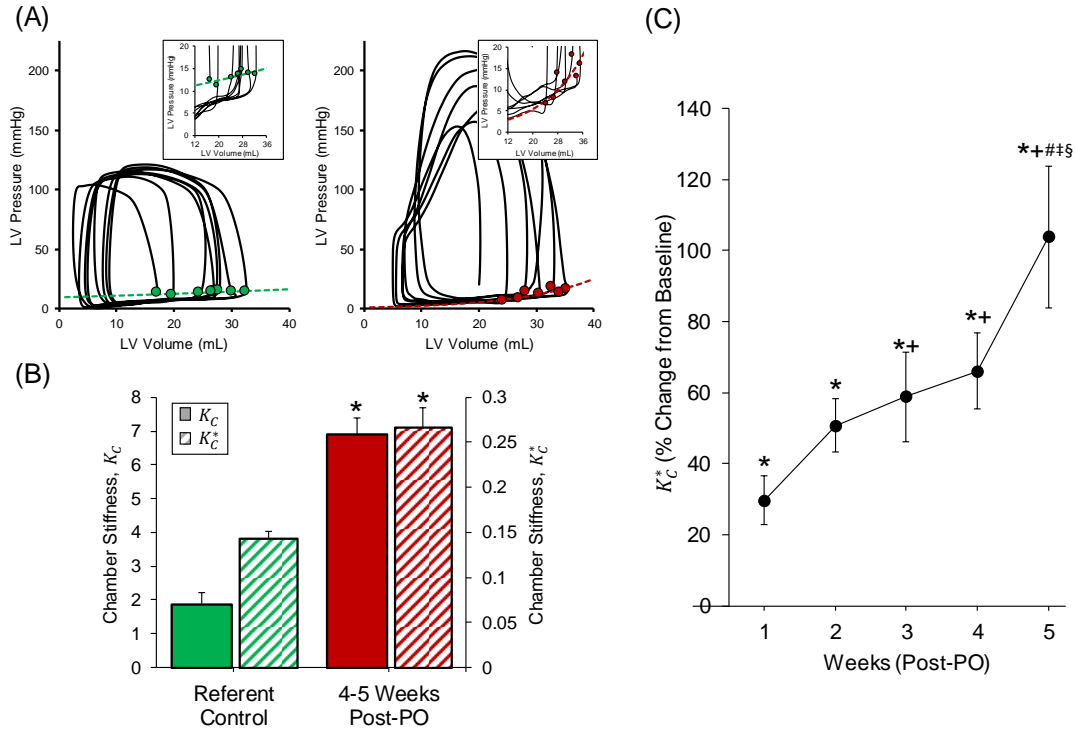
Figure 3.3: Evaluation of left ventricular chamber stiffness.
(A) Gold-standard techniques were used to derive measurements of left ventricular chamber stiffness in a subset of referent control (n=5) and pigs four- or five-weeks post-PO (n=5) from pressure-volume relationships. A significant reduction in LV chamber compliance was observed in the animals four- to five-weeks post-PO – as evidenced by the included representative examples. (B) A non-invasive surrogate of LV chamber stiffness (K_C^*) was generated and validated against the gold-standard measurements of chamber stiffness. While differing in magnitude, a correlative response was observed between the two measurements. (C) This non-invasive measurement of chamber stiffness allows for the serial assessment of diastolic function and demonstrates progressive stiffening of the LV chamber through the five weeks of the study. * $p<0.05$ vs. baseline value, $+$ $p<0.05$ vs. one-week value, $\#$ $p<0.05$ vs. two-weeks value, $\ddagger$ $p<0.05$ vs. three-weeks value, $\S$ $p<0.05$ vs. four-weeks value. (BL – three-weeks post-PO: n=15; four-weeks post-PO: n=14; five-weeks post-PO: n=7)

71
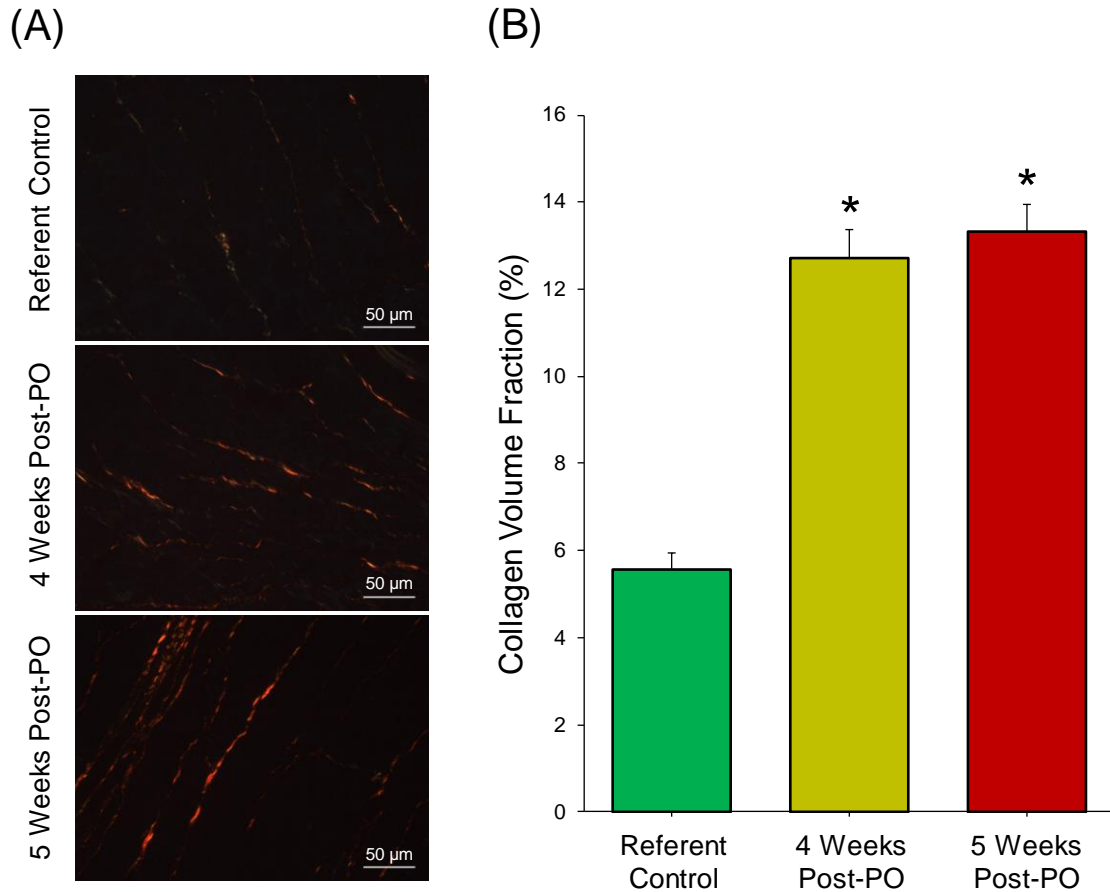
Figure 3.4: Quantification of collagen content.
(A) Transmural sections of the LV mid-myocardium were stained with picrosirius red and imaged at 40x magnification. (B) Collagen volume fraction (CVF) was computed for samples corresponding to referent control (n=7), four-weeks post-PO (n=6), and five-weeks post-PO (n=7). * $p<0.05$ vs. referent control value.
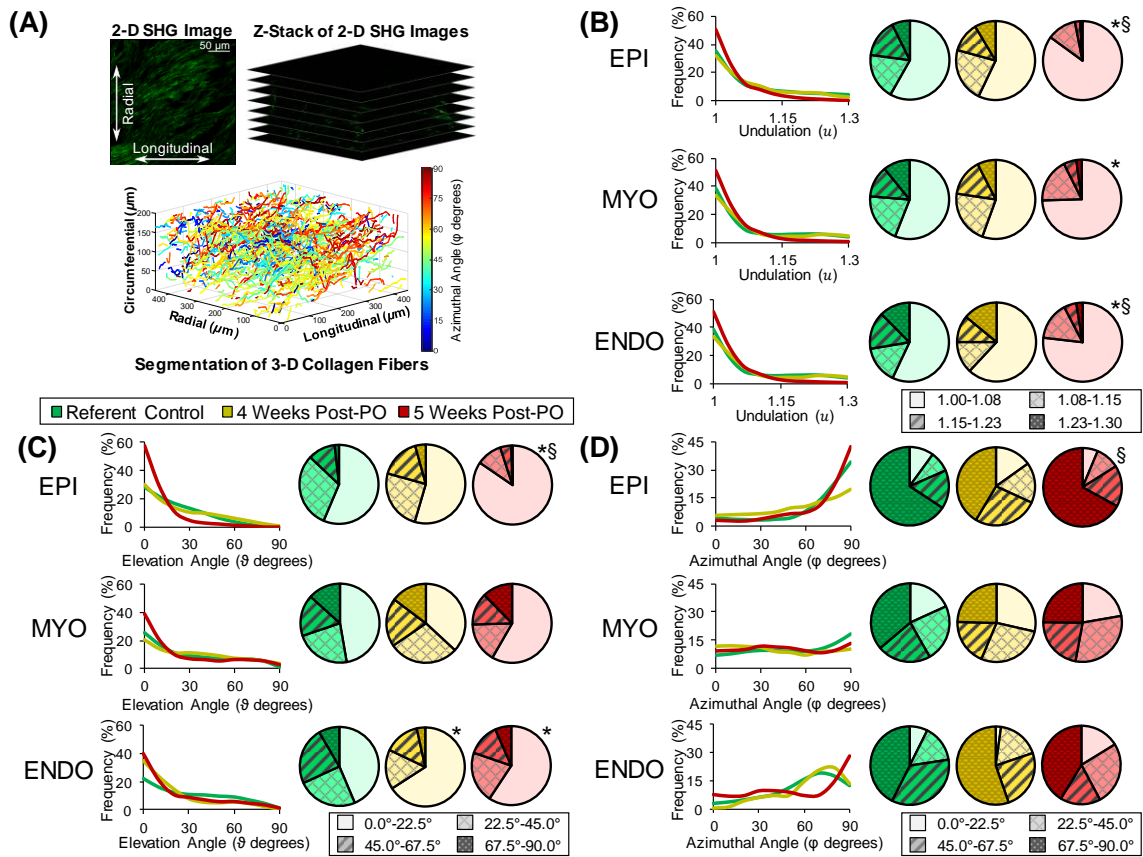
Figure 3.5: Characterization of collagen fiber structure and orientations.
(A) Three-dimensional stacks of two-dimensional images acquired from second harmonic generation enabled reconstruction of collagen fibers and subsequent representation as vectors in a Cartesian coordinate system for samples corresponding to referent control (n=5), four-weeks post-PO (n=6), and five-weeks post-PO (n=7). (B) Regional fiber undulation (u) distributions were computed for the epicardium (EPI), mid-myocardium (MYO), and endocardium (ENDO) based on reconstructed fiber geometries. Two fiber-specific angles were computed to quantify fiber orientation. (C) The elevation angle, ϑ, was computed from the circumferential-longitudinal plane. An angle of $\vartheta=0°$ indicates fiber alignment with the circumferential axis. (D) The azimuthal angle, φ, was computed from the longitudinal-radial plane. An angle of $\varphi=0°$ indicates fiber alignment with the radial axis. * $p<0.05$ vs. referent control value, § $p<0.05$ vs. four-weeks value.
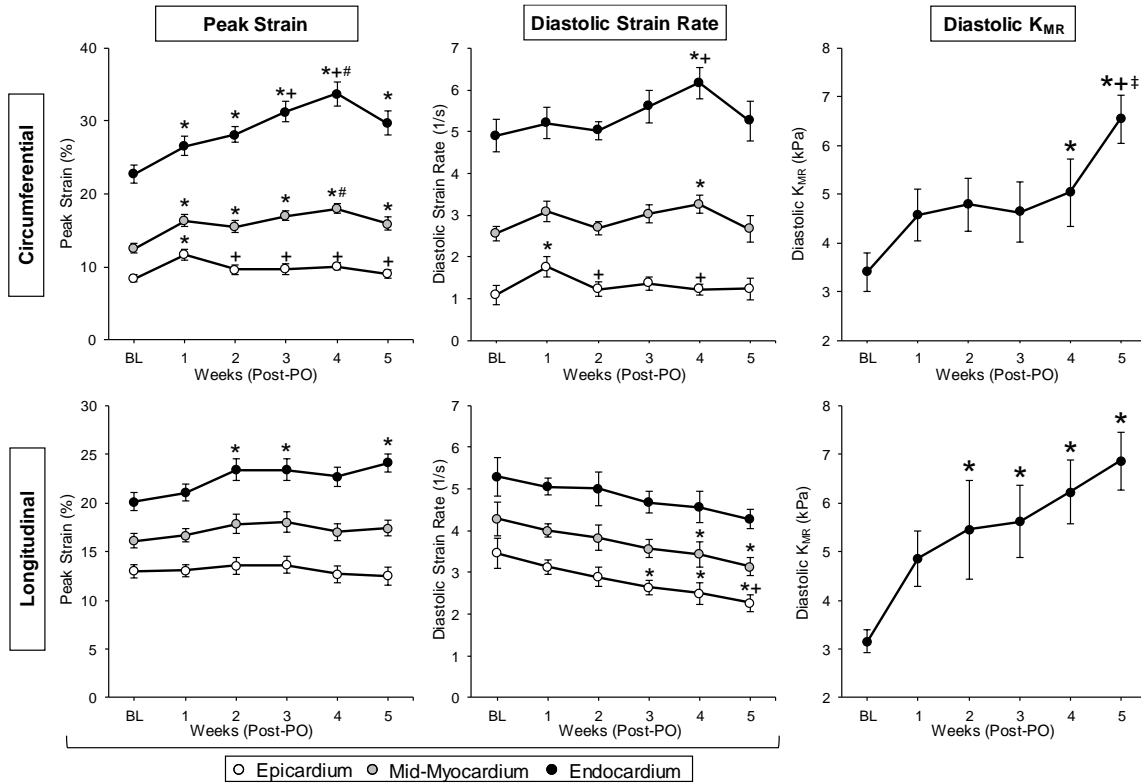
Figure 3.6: Biomechanical response and properties.
Peak strain (left column) and diastolic strain rate (middle column) underwent similar changes in the epicardium, mid-myocardium, and endocardium over five weeks post-PO. The mean regional diastolic myocardial stiffness ($|\kappa_{MR}|$ right column) was found to progressively increase over five-weeks post-PO in both the circumferential and longitudinal directions. * $p<0.05$ vs. baseline value, $^+$ $p<0.05$ vs. one-week value, ‡ $p<0.05$ vs. three-weeks value. (BL − three-weeks post-PO: n=15; four-weeks post-PO: n=14; five-weeks post-PO: n=7)

74

		Peak Strain (%)	Diastolic Strain Rate (1/s)	Diastolic K_{MR} (kPa)
Thickness (mm)		0.17	0.35	0.34
CVF (%)		-0.08	-0.04	0.32
λ	EPI	0.19	0.07	-0.68 *
	MYO	0.45	0.24	-0.58 *
	ENDO	0.24	0.22	-0.57 *
ϑ (deg)	EPI	0.32	0.32	-0.62 *
	MYO	0.40	0.27	-0.48
	ENDO	0.29	0.06	-0.35
φ (deg)	EPI	-0.07	-0.03	0.13
	MYO	0.24	0.18	-0.35
	ENDO	0.12	0.19	-0.29

Spearman's Rank Correlation (ρ): 0.70, 0.35, 0.00, -0.35, -0.70
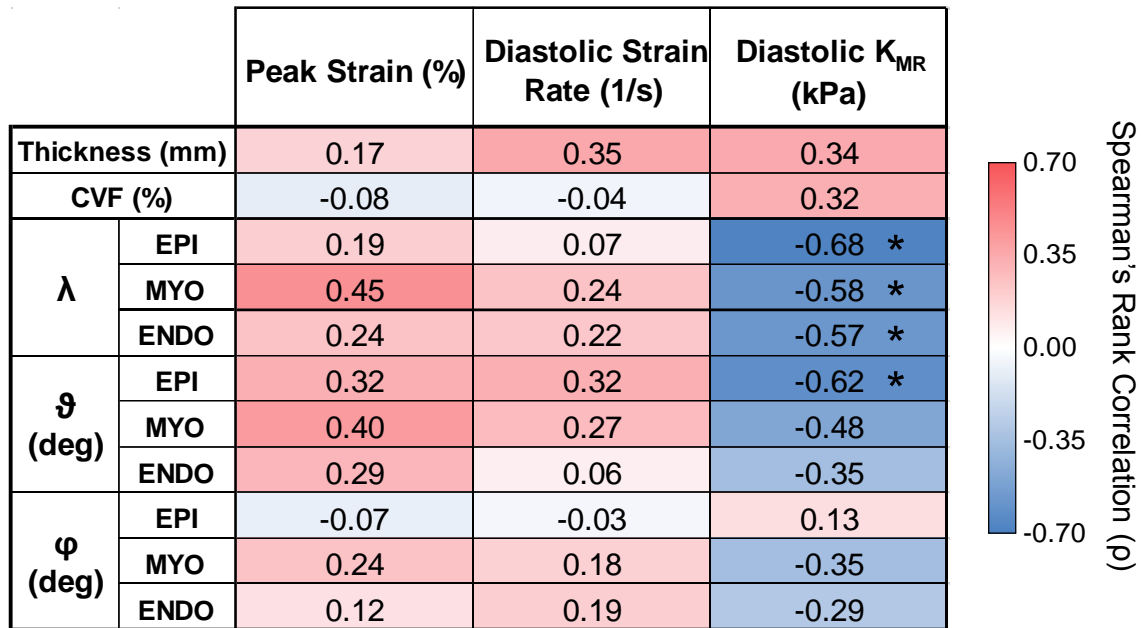
Figure 3.7: Biomechanical, geometrical, compositional, and microstructural correlations.
A Spearman's rank correlation analysis was used to interrelate region-matched biomechanical response variables (peak strain, diastolic strain rate, and diastolic myocardial stiffness (K_{MR})) with geometrical (wall thickness), compositional (collagen volume fraction (CVF)), and microstructural (collagen undulation (u) and orientation (ϑ and φ)) response variables. All correlations refer to the terminal study timepoint (four-weeks post-PO: n=6; five-weeks post-PO: n=7). * $p<0.05$ for Spearman's rank correlation coefficient (ρ). (EPI: epicardium; MYO: mid-myocardium; ENDO: endocardium)
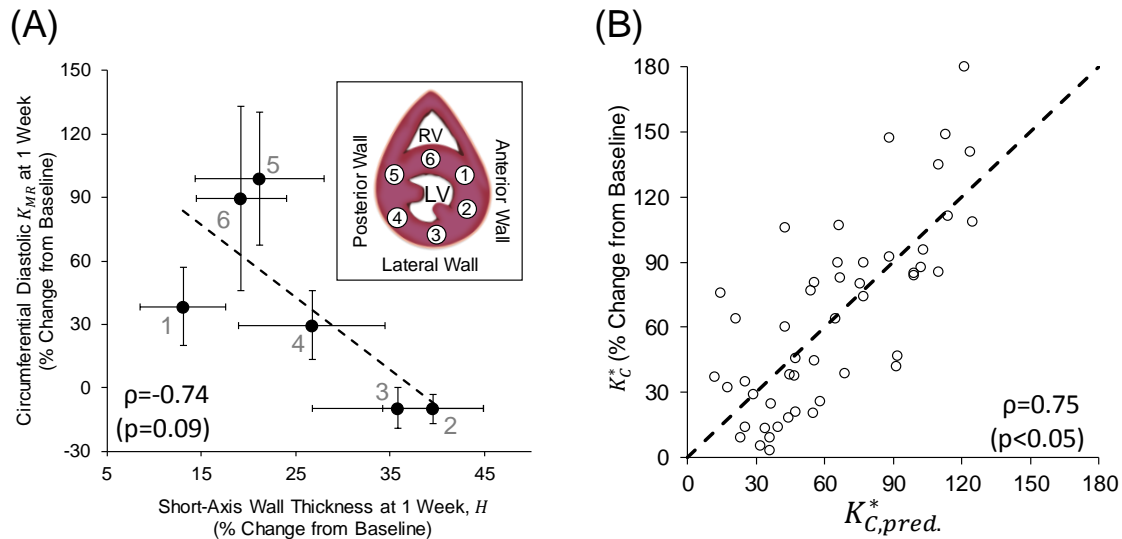
Figure 3.8: A method for predicting the late PO-induced increase in LV chamber stiffness based on early measurements of LV geometry, local material stiffness, and LV chamber stiffness.

(A) Region-matched changes in wall thickness and circumferential diastolic myocardial stiffness obtained at one-week post-PO (K_{MR}), reported as the mean values among all animals (n=14) in the circumferential direction. The observed inverse correlation is indicative of adaptive remodeling that mitigates increased wall stress with PO, whereby we propose the degree of subject-specific adaptivity is related to the degree to which local wall thickening is compensated for by a relatively muted increase in local diastolic myocardial stiffness. (B) A predicted value for changes in LV chamber stiffness relative to baseline ($K_{C,pred.}^*$) at three-weeks, four-weeks, and five-weeks post-PO was generated through multiple linear regression modeling of subject-specific response variables using LV chamber stiffness (K_C^*) and ($\partial K_{MR}/\partial H$) taken at one-week post-PO as input variables. $K_{C,pred.}^*$ significantly correlated with the experimentally measured values, suggesting that measurements obtained at one-week post-PO can predict the severity of subsequent LV chamber stiffening.

76

CHAPTER 4

ECHOCARDIOGRAPHIC QUANTIFICATION OF THE PASSIVE

MECHANICAL PROPERTIES OF THE LEFT VENTRICULAR

MYOCARDIUM [3]

---

[3] Torres W. M., Spinale F. G., Shazly T. Echocardiographic quantification of the passive mechanical properties of the left ventricular myocardium. Submitted to *Journal of the American Society of Echocardiography* on March 1st, 2019.

4.1 ABSTRACT

Advancing assessment of the rate and extent of left ventricular (LV) remodeling holds great value for heart failure (HF) diagnosis and prognosis. While global longitudinal myocardial strain determined by speckle-tracking echocardiography (STE) has been considered as a remodeling response variable, reported strain measures are limited by the masking of regional differences and a dependency on hemodynamic load. Our study entails a novel extension of two-dimensional STE to quantify the regional passive mechanical properties of the LV myocardium – providing a clinically accessible, load-independent response variable that reflects the LV remodeling process. An inverse finite element analysis was employed with a pattern search optimization algorithm to identify regional indices of passive myocardial stiffness based on STE-derived regional longitudinal strains and wall geometries. Our framework was applied in two distinct porcine models of early LV remodeling, specifically following myocardial infarction and onset of LV pressure overload. Obtained results elucidate regional and temporal changes in passive myocardial stiffness throughout early LV remodeling in both animal models. Changes in passive myocardial stiffness demonstrate enhanced sensitivity as compared to changes in global strain, and strongly correlate with conventional indices of LV remodeling. Regional passive myocardial stiffness can be noninvasively determined via STE data processing using an inverse finite element framework and provides a sensitive index of LV remodeling with potential to aid in HF diagnosis and prognosis.

4.2   INTRODUCTION

Heart failure (HF) is a clinical syndrome which most commonly arises from two potentially overlapping physiological causes: impaired left ventricular (LV) ejection performance or impaired LV filling. In terms of HF phenotyping, impaired LV ejection performance is defined as HF with reduced ejection fraction (HFrEF) while impaired LV filling with a stable ejection performance is defined as HF with preserved ejection fraction (HFpEF). These HF phenotypes emerge from distinctly different etiologies, whereby HFrEF commonly occurs secondary to myocardial injury/ischemia and HFpEF arises from a chronic LV pressure overload such as hypertension. In both HFrEF and HFpEF, the LV undergoes progressive changes in geometry, composition, and mechanical properties collectively known as LV remodeling.[52,56,153–156] While nominally an adaptive response, LV remodeling underlies HF progression, and consequently its serial assessment holds great value in HF diagnosis and prognosis.[157–160]

Although commonly used in a clinical setting, global measures of LV function such as ejection fraction or volumes can be insensitive to early changes in LV performance and thus fail to identify HF development and progression. Alternatively, the assessment of regional function through the quantification of LV myocardial strain, defined as the fractional change in length of a myocardial segment relative to its baseline length, has gained traction recently as a comparatively sensitive index of LV remodeling.[161] Developments in ultrasound-based imaging technology enable serial quantification of LV myocardial strain in a clinical setting. Specifically, speckle-tracking echocardiography (STE) tracks segmental length changes via the relative movement of intrinsic acoustic markers of the LV to quantify regional myocardial strain.[7] The analysis of both global

79

(fractional change in total segmental length) and regional longitudinal strain using STE can provide diagnostic information in disease states ranging from myocardial infarction to cardiotoxicity.[64,65,122,134,137]

Despite the demonstrated clinical utility of STE for the assessment of LV remodeling, there are clear factors limiting its clinical adoption.[162] Firstly, most clinical use of STE has been focused on global longitudinal strain despite the availability of regional measures – significantly narrowing the field of diagnostic information by masking potentially distinct regional changes.[161,163,164] Secondly, obtained strain measurements are highly dependent on hemodynamics (e.g. blood pressure, heart rate) and assumptions used to calculate LV wall geometry.[165,166] Not fully accounting for these factors diminishes the value of serial STE-based measurements and inter-subject comparisons.

The objective of the current study is to minimize the load-dependency of STE-based measurements and more effectively leverage the full field of speckle data to assess LV remodeling. To this end, we integrate STE-derived measures of regional LV geometry and myocardial strain along with an estimation of the mechanical load (i.e. ventricular pressure) within an inverse finite-element framework to compute regional passive myocardial mechanical properties. STE data from porcine models of both ischemia reperfusion and LV pressure overload are processed in our inverse framework to generate spatiotemporal maps of a passive myocardial stiffness index and the diastolic myocardial stress throughout early LV remodeling.

4.3   MATERIALS AND METHODS

4.3.1   Large Animal Models of HFrEF and HFpEF

For both models of LV failure, mature pigs (Yorkshire, 20-22 kg) were utilized whereby HFrEF was induced by intracoronary induction of ischemia-reperfusion while HFpEF was induced by LV pressure overload due to progressive ascending aortic stenosis.[73,109] Briefly, for the HFrEF protocol, the pigs (n=8) were anesthetized (isoflurane, 3%/1.5L/min; nitrous oxide, 0.5L/min) and an angioplasty balloon catheter (5F Launcher guiding catheter, 0.058-in. HIS, Medtronic, Minneapolis, MN) was placed within the left anterior descending artery, immediately below the first obtuse marginal branch, under fluoroscopic guidance (Arcadis Varic C-Arm, Siemens, Munich, DE). After 90 minutes of coronary occlusion, the balloon was deflated and the catheter system was removed. This approach resulted in a reproducible apical anterior myocardial infarction, and over time a reduction in LV ejection fraction (LVEF) – thus recapitulating the HFrEF phenotype.[73,122] For HFpEF induced by LV pressure overload, pigs (n=9) were anesthetized as described above, and the ascending aorta accessed through a left thoracotomy. An inflatable silastic vascular cuff (12mm, Access Technologies, Skokie, IL) was secured around the supracoronary ascending aorta and connected to a subcutaneous access port. Serial hydraulic-mediated cuff inflation was initiated following a one-week recovery period, in which the cuff was inflated through the access port (via 0.45 mL glycerol) to achieve a specific target gradient of 75 mmHg across the cuff and induce LV pressure overload. At weekly intervals thereafter, the cuff was further inflated (0.25 mL increments) to cause a stepwise increase in the pressure gradient (25 mmHg increase/inflation).

81

All animals were treated and cared for in accordance with the National Institutes of Health *Guide for the Care and Use of Laboratory Animals* (*Eighth Edition*. Washington, DC: 2011) and all experimental protocols were approved by Institutional Animal Care and Use Committees at the University of South Carolina.

4.3.2   Serial Echocardiographic Studies

The day before animals underwent either coronary occlusion or placement of the aortic cuff, the pigs were sedated (diazepam, 200 mg), placed in a custom-designed sling, and transthoracic echocardiographic studies were performed (GE Vivid E9 with XDclear Ultrasound System; M5S (3.3 MHz, 40 FPS) transthoracic probe). Two-dimensional echocardiographic cine loops were acquired from a transthoracic right parasternal approach. The left atrium (LA) and LV were imaged in both the short- and long-axis views. Pulse-wave and tissue Doppler studies were performed to determine flow velocities and pressure gradients.[167]

The pigs were then returned to the laboratory for follow-up imaging studies under identical conditions and approaches, whereby the HFrEF pigs were returned for imaging studies at 14 and 28 days post-coronary occlusion and the HFpEF pigs were returned to the laboratory at 7, 14, 21, and 28 days for both imaging studies and serial hydraulic-mediated expansion of the aortic cuff under echocardiographic guidance and sterile conditions as described previously.[109]

4.3.3   Post-Acquisition Analysis of LV Function and Geometry

The digital echocardiographic images were transferred to a workstation for offline analysis (EchoPac, Vingmed, GE). LV end-diastolic volume (EDV) and LVEF were calculated using the biplane method of disks. LA area was determined from the

82

anteroposterior dimensions acquired from the parasternal long axis view. For each digital loop, a region of interest (ROI) was defined at the onset of the R-wave by manually identifying the endocardial and epicardial borders. The ROI was then discretized with a spatial mesh of acoustic clusters to be tracked on a frame-to-frame basis throughout a single cardiac cycle.[7] Quantitative strain analysis (Q-analysis) was performed, regional tracking quality was assessed, and the ROI was manually adjusted by the operator to improve tracking quality where necessary. Successful tracking of the ROI allowed for the definition of segmental lengths which were computed at end-diastole (L_0) and continuously throughout the cardiac cycle (L). Segmental strains (ε) were then computed as:

$$\varepsilon = \frac{L - L_0}{L_0} = \frac{\Delta L}{L_0}, \qquad (4.1)$$

where the reference length refers to the end-to-end length in the longitudinal direction of a particular echocardiographic segment (i.e. basal posterior, mid posterior, apical posterior, apical anterior septum, mid anterior septum, or basal anterior septum) or, in the case of global longitudinal strain, the end-to-end length of the mid-myocardium in the longitudinal direction (i.e. from the basal posterior, to the apex, and then to the basal anterior septum). Subsequently, spatial coordinates of the mid-myocardial nodes were exported for each frame of the digital loop. Additionally, wall thickness was collected at early- and end-diastole for each of the six conventional echocardiographic segments. Pulmonary capillary wedge pressure (PCWP) was subsequently calculated using the method proposed by Nagueh *et al* in 1997.[168]

4.3.4   Formulation of the Finite-Element Mesh

The initial, unloaded, LV configuration was generated from the position of the mid-myocardial nodes at the onset of diastole, the point at which the cross-sectional area was

83

at a minimum. For each mid-myocardial node, a thickness was defined by computing a cubic spline interpolation between the known thicknesses at the onset of diastole of the six echocardiographic segments. Endocardial and epicardial nodes were subsequently generated based on the position of the mid-myocardial nodes and estimated thicknesses. The finite-element mesh was constructed from this reference geometry composed of a monolayer of eight-node trilinear hexahedral elements with two elements spanning the distance between each of the mid-myocardial nodes and eight elements spanning the distance between the pairs of endocardial and epicardial nodes (**Figure 4.1A-C**). This process was also completed for the end-diastolic configuration to enable calculation of the objective function as detailed below (**Figure 4.1D-F**).

4.3.5   Material Model and Boundary Conditions

The LV myocardium was modeled as a transversely isotropic Mooney-Rivlin solid, a model well-suited for biological soft tissues with a preferred fiber direction.[169] The uncoupled strain energy function is:

$$W = F_1\big(\widetilde{I_1}, \widetilde{I_2}\big) + F_2\big(\tilde{\lambda}\big) + \frac{K}{2}[\ln(J)]^2, \qquad (4.2)$$

where K is the bulk modulus-like penalty parameter and J is the determinant of the deformation gradient tensor. The function $F_1\big(\widetilde{I_1}, \widetilde{I_2}\big)$, a function of the first and second invariants of the deviatoric right Cauchy-Green deformation tensor, represents the material response of the isotropic Mooney-Rivlin ground substance matrix of the form:

$$F_1\big(\widetilde{I_1}, \widetilde{I_2}\big) = S[C_1(\widetilde{I_1} - 3)] + S[C_2(\widetilde{I_2} - 3)] + \frac{K}{2}[\ln(J)]^2 \qquad (4.3)$$

84

where C_1 and C_2 are the material coefficients and S is the regional stiffness index. $F_2(\tilde{\lambda})$, a function of the fiber stretch ratio, represents the contribution from the fiber family with a strain energy of the following form:

$$F_2(\tilde{\lambda}) = \begin{cases} 0 & \tilde{\lambda} \leq 1 \\ C_3 \left[e^{-C_4} \left(Ei(C_4\tilde{\lambda}) - Ei(C_4) \right) - \ln \tilde{\lambda} \right] & 1 < \tilde{\lambda} < \lambda_m \\ C_5(\tilde{\lambda} - 1) + C_6 \ln \tilde{\lambda} & \tilde{\lambda} \geq \lambda_m \end{cases} \quad (4.4)$$

where C_3 scales the exponential term, C_4 is the fiber crimping coefficient, C_5 is the modulus of the straightened fibers, and λ_m is the stretch at which the fibers are straightened. Furthermore, $Ei(\cdot)$ is the exponential integral function and C_6 is determined from stress continuity requirements. The fiber orientation was specified for each element to be 15° relative to the longitudinal axis on the longitudinal-radial plane with a λ_m of 1.10. The remaining material parameters, barring the regional stiffness index, were valued in accordance with prior work on biaxial testing on excised canine hearts.[17] The regional stiffness index, S, was determined from the optimization scheme described in the following section.

Two quasi-static structural mechanics steps were defined as follows. In step one, a prescribed translation was applied to the basal nodes from the undeformed configuration to the expected position at end-diastole as determined from STE. In step two, the basal node positions were fixed, and the end-diastolic pressure was applied to the endocardial surface.[170] To mimic the tethering effects of the right ventricle and the pericardium, an opposing pressure was applied to the basal and mid-ventricular epicardial nodes with a magnitude of 25% of that of the intraventricular pressure.[171,172] The solution was computed using the PARDISO linear solver within the FEBio application.[173,174]

85

4.3.6   Identification of Material Properties

An objective function (Π) of the form:

$$\Pi = \left(\frac{A\prime - A}{A} + \sum_{i=1}^{6}\left(\frac{\varepsilon_i' - \varepsilon_i}{\varepsilon_i}\right) + \frac{\bar{t}\prime - \bar{t}}{\bar{t}}\right) \times 100\% \quad (4.5)$$

was developed as a function of the actual end-diastolic area (A), regional strain (ε_i) relative to the undeformed mesh, and mean wall thickness ($\bar{t}$) determined from the end-diastolic mesh (**Figure 4.1F**). Additionally, A', ε_i', and $\overline{t'}$ represent the end-diastolic area, regional strain relative to the undeformed mesh, and mean wall thickness computed from the deformed FE model, respectively. The factors entering the optimization scheme were the stiffness indices (S) defined at the center of each of the six conventional anatomical segments of the LV. A cubic spline interpolation was used to define a continuous distribution of stiffness indices between the six segments. A pattern search optimization algorithm, ideal for the minimization of a non-differentiable objective function, was employed to identify an optimal set of stiffness indices coincident with the global minimum of the objective function. The pattern search algorithm was terminated when a successful poll resulted in a change in the objective function of less than 1E-6 (**Figure 4.2**).

The optimization process was conducted on a workstation with an eight-core processor (3.7 GHz) and 32 GB of RAM. After optimization was complete, a final simulation with a refined FE mesh and assigned regional values of S was performed, thus facilitating the calculation of the first principal stress field.

4.3.7   Statistical Analysis

Data are reported as the mean ± standard error of the mean. Comparative analyses between the two groups were performed using a two-way analysis of variance followed by

86

pair-wise comparisons using the least significant difference *post hoc* study. A Pearson correlation analysis was used to interrelate classical echocardiographic indices with those derived from regional inverse analyses. A p-value of less than 0.05 was considered statistically significant. All statistical analyses were performed in MATLAB (version R2018a, The MathWorks Inc).

4.4   RESULTS

4.4.1   Left Ventricular Function and Geometry

LV function and geometry at baseline and at the two specified time points (14 and 28 days) are shown in **Table 4.1**. In the HFrEF group, LVEF was reduced and LV dilation occurred; consistent with the HFrEF phenotype. In the HFpEF group, LVEF and LV volume were unchanged, whereas LA area increased; consistent with the HFpEF phenotype. Spatial mapping of regional LV longitudinal strain showed an overall reduction in the HFrEF group, with the greatest reductions occurring in the mid- and apical-anterior regions. In marked contrast, regional LV longitudinal strain remained comparatively preserved in the HFpEF group (**Figure 4.3A**). Global LV longitudinal strain fell by approximately 50% from baseline at both 14 and 28 days in the HFrEF group, whereas there was no change in the HFpEF group (**Figure 4.3B**). The relative heterogeneity of LV strain, reflected by the coefficient of variation among regional strains, more than doubled in the HFrEF group by 28 days but remained unchanged in the HFpEF group (**Figure 4.3B**).

87

4.4.2 Inverse Estimation of Regional Stiffness Indices

For each case, the pattern search optimization algorithm was initiated, and the relative error in regional strain, mean wall thickness, and LV area was quantified through the objective function (Π) for each set of stiffness indices defined by the algorithm. A global minimum of the objective function was reached through iterative refinement of the stiffness indices for all cases with an average convergence time of 48.6±3.4 minutes. The minimum objective function values obtained for the HFrEF group at both 14 days and 28 days were found to be significantly elevated relative to baseline values (Π=11.8±1.4 (baseline) vs. Π=28.3±7.7 (14 days) and Π=35.3±6.9 (28 days), p<0.05). In contrast, insignificant changes in the obtained minimum objective function values were observed in the HFpEF group between baseline and 28 days. Elevated objective function values in the HFrEF group are an expected consequence of the increasingly heterogeneous wall geometry and mechanical behavior associated with the induced LV remodeling.

Changes in myocardial passive stiffness of the HFrEF group exhibited obvious regional dependence, exemplified at 28 days by the nearly order-of-magnitude higher stiffness index in the infarcted apical anterior region as compared to the remote myocardium (80.6±14.9 vs. 8.6±2.7) (**Figure 4.4A**). The global stiffness index, defined as the spatial-average of the passive regional stiffness indices, reached a maximum at 14 days in the HFrEF group and remained elevated relative to baseline at 28 days (**Figure 4.4B**). While changes in the global stiffness index in the HFpEF group were attenuated in comparison to the HFrEF group, a greater than three-fold increased relative to baseline was observed at 28 days. The relative heterogeneity of stiffness, taken as the coefficient of

variation among regional stiffness indices, was significantly elevated in the HFrEF group relative to both baseline and the HFpEF group at both 14 and 28 days (**Figure 4.4B**).

4.4.3 Myocardial Wall Stress

Subsequent simulations that incorporate the identified local stiffness indices allowed for quantification of the 1st principal stress field at end-diastole. At both 14 and 28 days, the maximal regional stress observed in the HFrEF group was coincident with the location of the ischemic injury, while a qualitatively more uniform stress distribution was observed in the HFpEF group (**Figure 4.5A**). The global 1st principal stress, defined as the spatial-average of 1st principal stress, was elevated relative to baseline in both groups at 14 and 28 days, with significantly higher stresses in the HFrEF group compared to the HFpEF group (**Figure 4.5B**).

4.4.4 Correlation Analysis

A correlation matrix was developed for each group to relate established indices of global function and geometry to computed biomechanical indices (**Figure 4.6**). In the HFrEF group, global LV longitudinal strain positively correlated with LVEF and negatively correlated with LV volume and LA area. Inverse relations were observed when these indices were correlated with global stiffness index and global 1st principal stress. Conversely in the HFpEF group, there was no correlation between global LV longitudinal strain and LV ejection fraction, volume, or LA area. Notably, LA area, an index of progressive HF, exhibited strong positive correlations with the computed global stiffness index and global 1st principal stress in both the HFrEF and HFpEF groups.

89

4.5   DISCUSSION

The structural and functional milestones for the development and progression to heart failure (HF) are changes in LV structure and function – commonly termed myocardial remodeling. This process is manifested at the regional myocardial level, and thus, approaches which can identify and be sensitive to changes in regional myocardial mechanics would allow for early detection in patients at risk for HF progression. While past studies using magnetic resonance imaging and post-processing algorithms have identified the potential relevance of assessing regional mechanics in patients with developing HF, this approach can be problematic. Firstly, this imaging approach is not amenable to point-of-care application and analysis. Secondly, this imaging approach is not readily amenable to repeated, serial measurements in terms of screening and identifying HF progression. Accordingly, the major significance of this study was to put-to-practice a methodology and framework to quantify myocardial mechanical properties based on post-processing of typically available echocardiographic data.

While HF is a term which applies to the spectrum of symptoms, it is important to phenotype the underlying HF process. In that regard, it is now recognized by consensus that HFrEF and HFpEF are two distinct phenotypes, with differing etiologies, trajectories to HF, and, most importantly, distinctly different forms of LV dysfunction. To that end, we developed a novel approach to quantify myocardial mechanical properties and applied it to relevant large animal models of HFrEF and HFpEF. Our results demonstrated the utility of this approach in terms of serial measurements and revealed distinctly different patterns of regional myocardial mechanical changes in HFrEF and HFpEF. This work underscores the

90

need for sensitive assessments of LV regional mechanical performance to identify the development and progression of these HF phenotypes.

4.5.1   Building Upon Prior Studies

Even though the present study developed a regional LV stiffness index which is unique to this study, relative comparisons to other studies can be made. Specifically, elevations in the LV stiffness index with HFrEF, which peaked at 14 days post-MI, reflect similar trends in mechanical property indices reported in both *in-vivo* and *ex-vivo* studies.[57,76,79,81,122,175] Furthermore, the more progressive increases in this LV stiffness index with HFpEF is in agreement with observations made in both small and large animal models of LV pressure overload-induced hypertrophy.[18,132,133,176] However, it should be emphasized that the increased LV stiffness index in both HFrEF and HFpEF does not imply similar biological or physiological underpinnings. Specifically, in HFrEF secondary to MI, the predominant contribution to the increased global LV stiffness index was contained within the MI regions; reflective of scar formation and collagen accumulation. Contrarily in HFpEF, the LV stiffness index was due to a more global shift; reflective of the more diffuse collagen accumulation (i.e. fibrosis). The present study demonstrated that these distinctly different patterns of LV myocardial stiffness could be identified in both a spatial and temporal fashion.

4.5.2   Clinical Translation

The approaches applied to these preclinical large-animal models was then put-to-practice in terms of deployment as a complete software application (**Figure 4.7A**) using a de-identified transthoracic echocardiographic study (privacy policies set forth by the Department of Veteran's Affairs Cooperative Studies) of a patient with defined HFpEF

(i.e. elevated LV filling pressure and LA enlargement). Using the methodological approaches described herein, the heterogeneous distribution of stiffness indices and 1st principal Cauchy stress was computed (**Figure 4.7B-D**). As presented, this technology can be directly translated into a clinical setting as a complement to current standard-of-care echocardiography studies.

4.5.3   Future Directions

While this proof-of-concept study was completed on a workstation as a post-processing step for previously acquired images, it is feasible to translate this methodology to a server or cloud-computing framework to allow for direct incorporation into standard echocardiography machines. The FE solver and optimization algorithm employed in this study utilize parallelization of computational cores. Therefore, incorporating this framework into a many-threaded computational platform will drastically improve computational time – increasing the likelihood of translating this analysis in a clinical setting.[162] Furthermore, it is reasonable to assume an evolution of this technology which bypasses the inverse FE optimization all-together. Once this technology has been applied to enough cases, there will be a large library of evidence detailing the dynamic interplay between regional passive mechanical property changes and various forms of heart disease. A future evolution of this technology could be developed as a form of artificial intelligence informed by a supervised machine learning algorithm to predict the evolution of regional myocardial stiffness and stresses for a given patient based on the body of evidence previously collected from other patients.

4.5.4 Methodological Limitations

The present study demonstrates that an inverse methodology can be reasonably performed to estimate the passive mechanical properties of the LV myocardium relevant to a clinical context. However, several methodological limitations must be considered. First, while our results are in qualitative agreement with previously reported findings, *in-vivo* quantification of mechanical properties should be validated against results obtained from *ex-vivo* mechanical testing and modeling. Furthermore, given the inherent mechanical nonlinearity of the myocardium, the resultant passive stiffness indices refer only to a specific (low pressure) component of the overall myocardial mechanical response. Additionally, prior studies have shown shifts in the predominant collagen fiber orientation and undulation as a consequence of disease progression and relative position in the LV.[34,177] While this study assumes a constant fiber angle on the longitudinal-radial plane and a constant degree of fiber undulation, future iterations of the model will incorporate these known variations. Finally, the model is limited to two-dimensions and exhibits sensitivity to the applied boundary conditions. Future work will be focused on translating this framework to three-dimensions and the application of increasingly realistic boundary conditions.

4.5.5 Conclusion

The methods and framework proposed herein promote passive myocardial mechanical property identification, and therefore could help evaluate the rate and extent of LV remodeling in the context of heart disease. This type of noninvasive, point-of-care analysis has the potential to significantly improve cardiovascular disease diagnostics and inform clinicians and researchers on patient-specific disease progression.

93

4.6   ACKNOWLEDGMENTS

4.7 TABLES

Table 4.1: Echocardiographic estimation of indices of left ventricular geometry and function

Treatment	Day	LVEF (%)	EDV/BW (mL/kg)	LA Area (cm^2)
Baseline (17)	0	64.6 ± 1.3	1.6 ± 0.1	6.2 ± 0.3
HFrEF (8)	14	37.8 ± 2.3*	2.8 ± 0.2*	10.1 ± 0.4*
	28	37.5 ± 3.4*	2.6 ± 0.2*	11.0 ± 0.4*
HFpEF (9)	14	63.8 ± 1.0	1.6 ± 0.2	9.9 ± 0.5*
	28	66.1 ± 1.0	1.5 ± 0.1	11.3 ± 0.5*

Values are means ± SE. * $p < 0.05$ vs. the respective baseline value. (LVEF: left ventricular ejection fraction; EDV: end diastolic volume; BW: body weight; LA: left atrium)
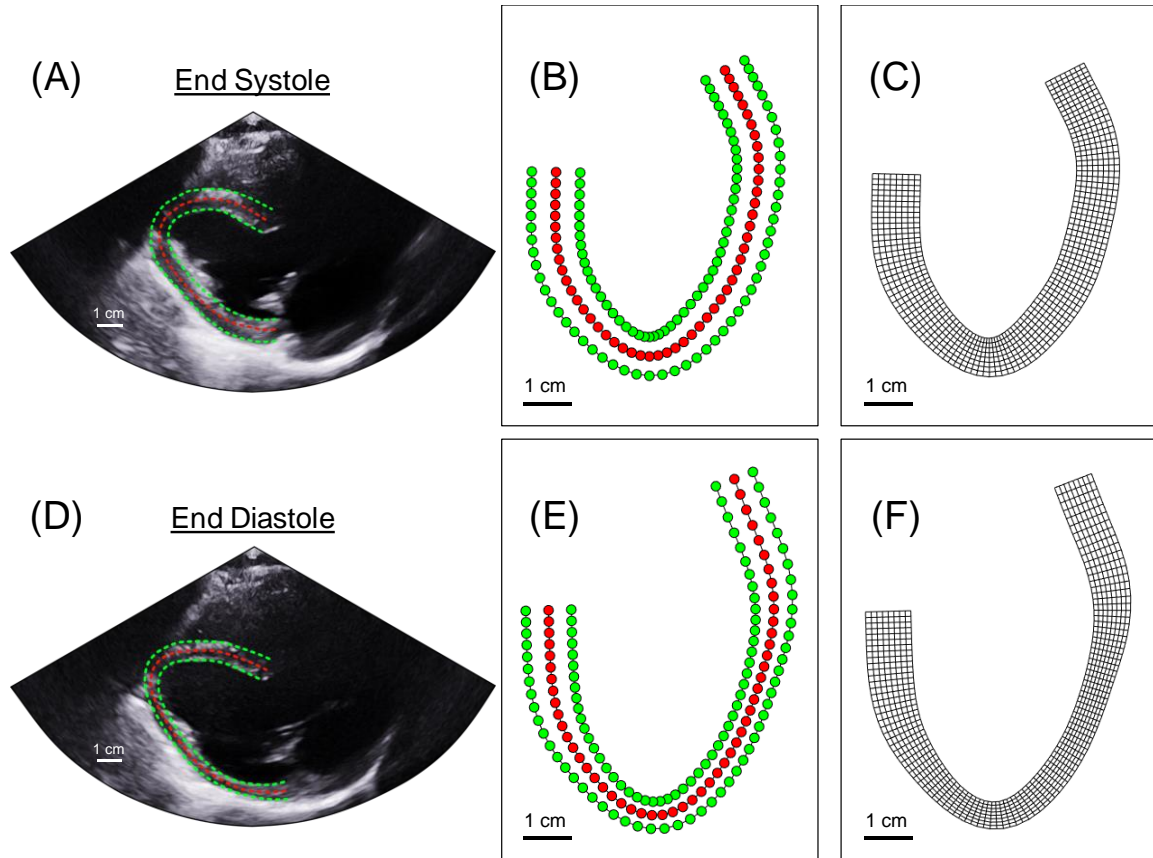
Figure 4.1: Formulation of the finite element mesh.
(A, D) At both end-systole and end-diastole, quantitative strain analysis was performed on LV long-axis echocardiographic images. **(B, E)** Epicardial, mid-myocardial, and endocardial nodes were defined from the mid-myocardial strain analysis position data and regional thickness measurements. **(C, F)** A eight-node trilinear hexahedral FE mesh was formulated with two elements spanning the distance between each of the mid-myocardial nodes and eight elements spanning the distance between the pairs of endocardial and epicardial nodes

96

Figure 4.2: Inverse methodology to identify mechanical properties from STE.
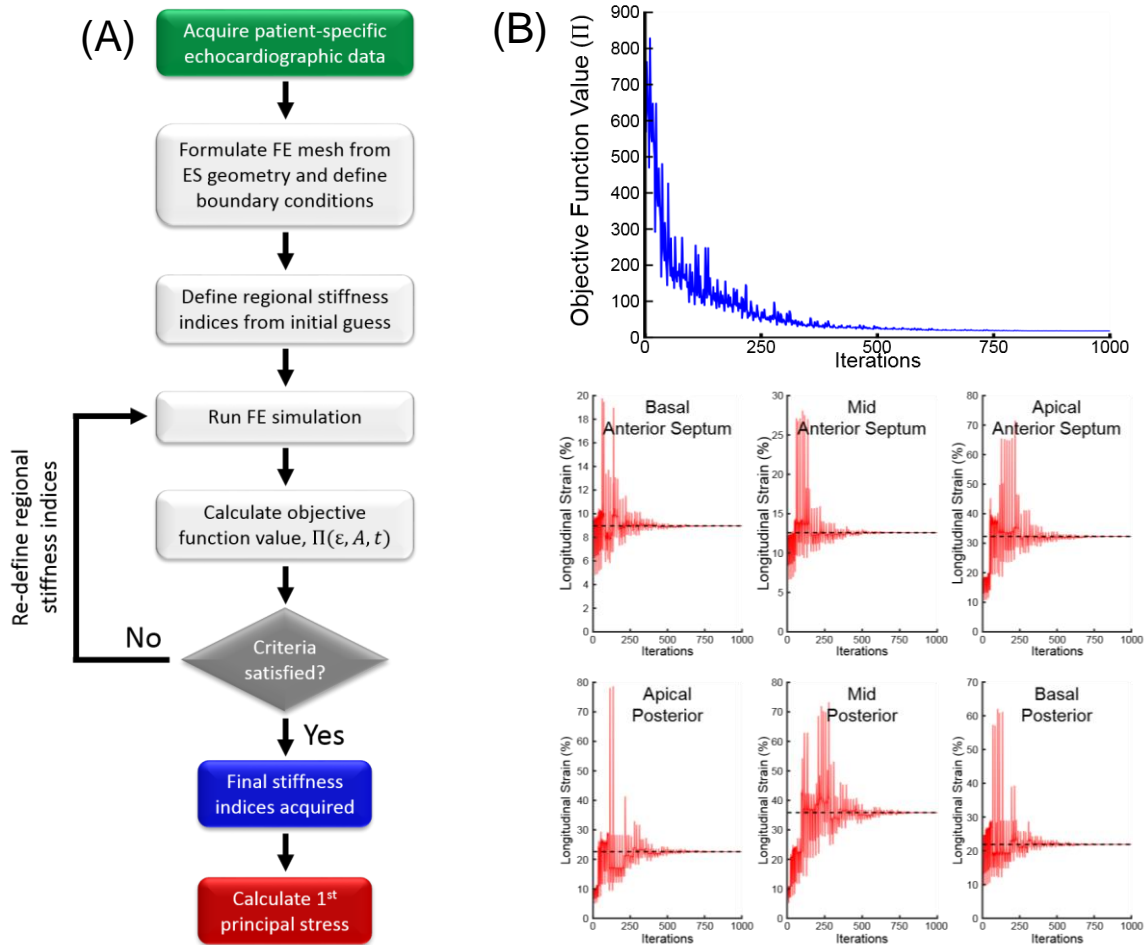**(A)** From the echocardiographic cine loops, mid-myocardial position data, regional wall thickness, and estimations of PCWP were acquired. A FE model is generated from the initial end-systolic geometry and boundary conditions are defined for two quasi-static simulation steps. An initial guess for the regional stiffness indices is defined and the converged solution was attained from a PARDISO linear FE solver. **(B)** The objective function (Π) value is determined and evaluated against the stopping criteria. If stopping criteria is not met, regional stiffness indices were re-defined from the pattern search optimization algorithm. After the stopping criteria is satisfied, a final regional distribution of stiffness indices is acquired, and end-diastolic longitudinal and radial stress are calculated. The pattern search optimization algorithm iteratively explored combinations of regional stiffness indices until a minimum value of the objective function (Π) was attained. As the objective function is minimized, the regional strain computed from the FE model converged upon the experimentally measured regional strain.
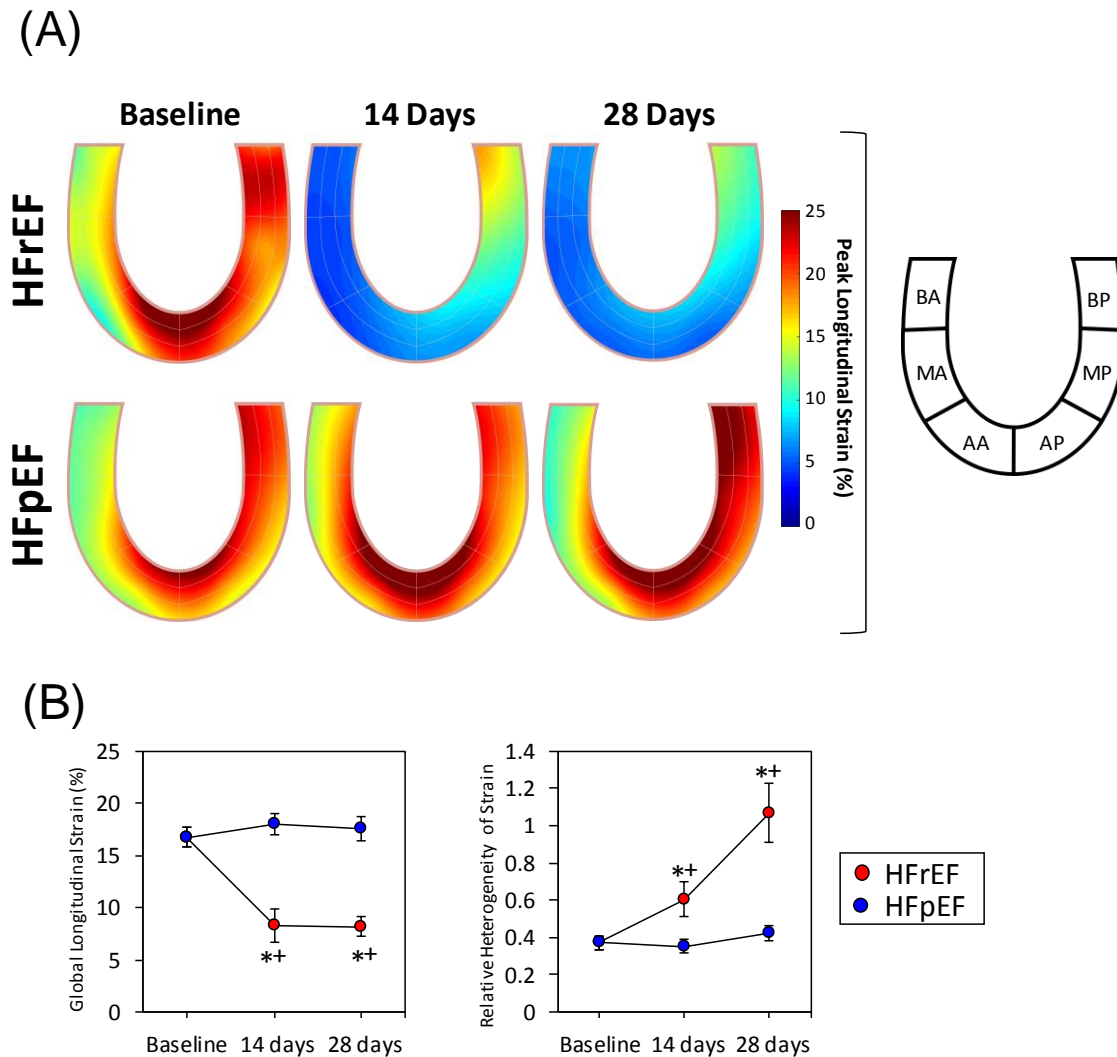
Figure 4.3: Changes in peak longitudinal strain throughout disease progression.
(**A**) Spatial maps of the absolute value of the peak LV longitudinal segmental strain determined directly from quantitative STE were generated for each of the two study groups at baseline as well as 14 and 28 days after the onset of disease. (**B**) The global LV longitudinal strain, taken as the fractional change in the total length of the LV cross-section, was determined for each subject over time. The relative heterogeneity of strain, taken as the coefficient of variation between each of the regional measurements, was determined for each subject over time. * $p < 0.05$ vs. respective baseline value; [+] $p < 0.05$ vs. respective HFpEF value.
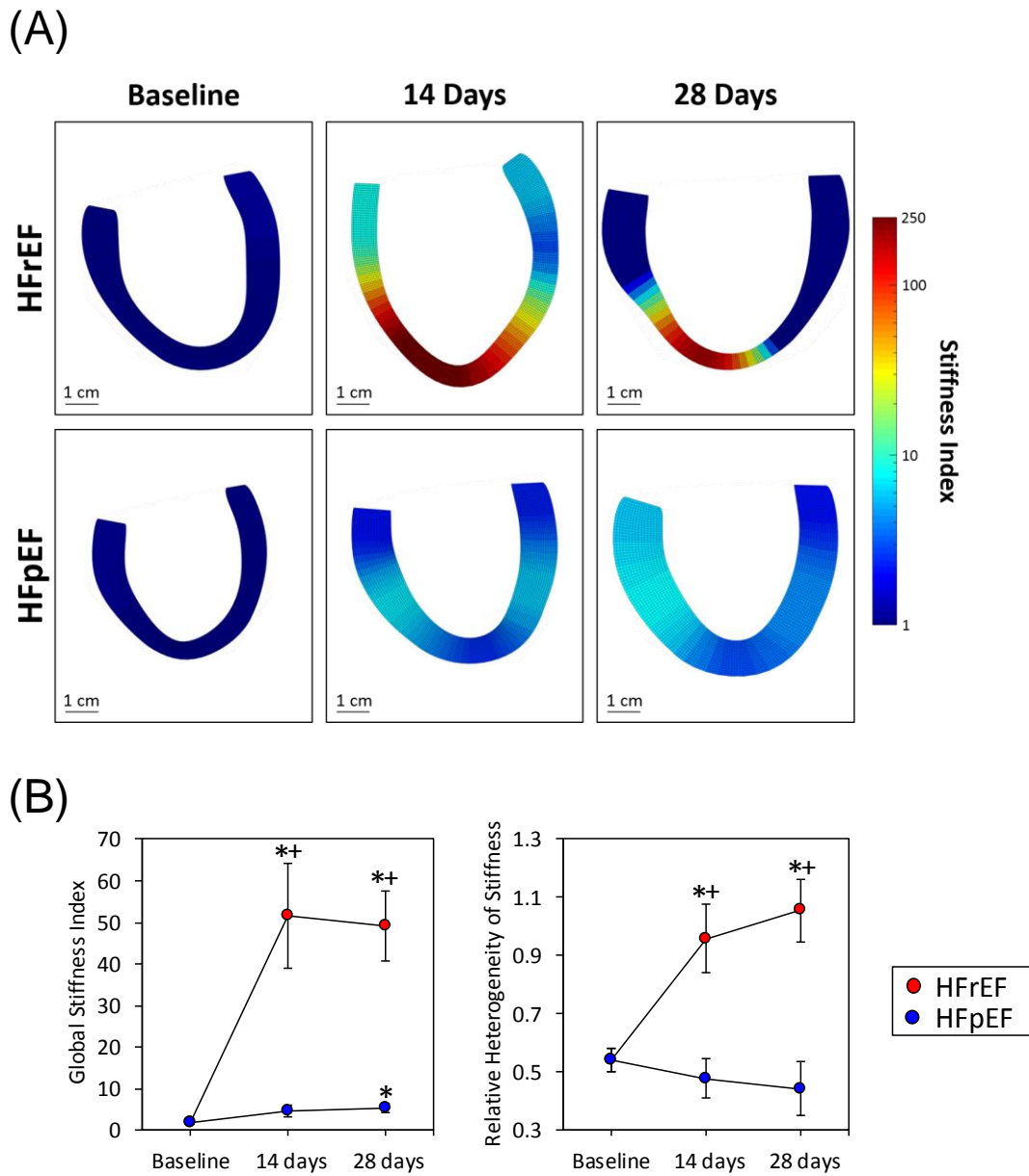
Figure 4.4: Dynamic changes in regional mechanical stiffness throughout disease progression.
The inverse method of identifying mechanical properties was applied to each subject at baseline as well as 14 and 28 days after the onset of disease. **(A)** Representative cases of both heart disease models demonstrate heterogeneous regional changes in mechanical stiffness as the disease progresses. **(B)** The spatially-averaged global stiffness index was determined for each subject over time. Additionally, the relative heterogeneity of stiffness, taken as the coefficient of variation for each subject, was determined for each subject over time. * $p < 0.05$ vs. respective baseline value; + $p < 0.05$ vs. respective HFpEF value.

99
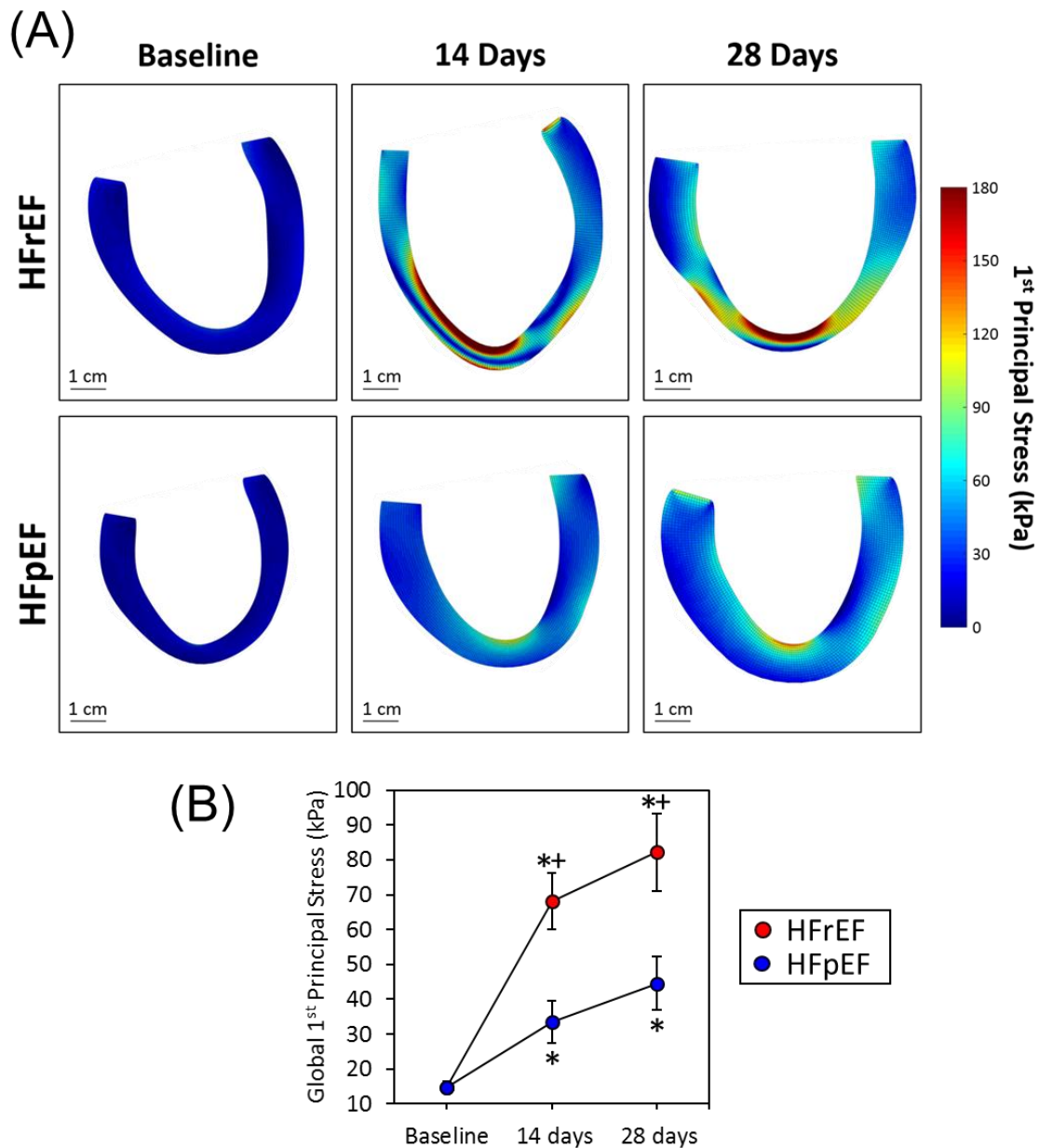
Figure 4.5: Determination of end diastolic myocardial wall stress.
The 1st principal stress throughout the myocardium was computed for each subject at baseline as well as 14 and 28 days after the onset of disease. **(A)** Representative cases of both heart disease models demonstrate the spatial variance of 1st principal stress and the extent to which this is altered throughout the progression of the disease. **(B)** The spatial-average of 1st principal stress (i.e. global 1st principal stress) was determined for each subject over time. * $p<0.05$ vs. respective baseline value; + $p<0.05$ vs. respective HFpEF value.
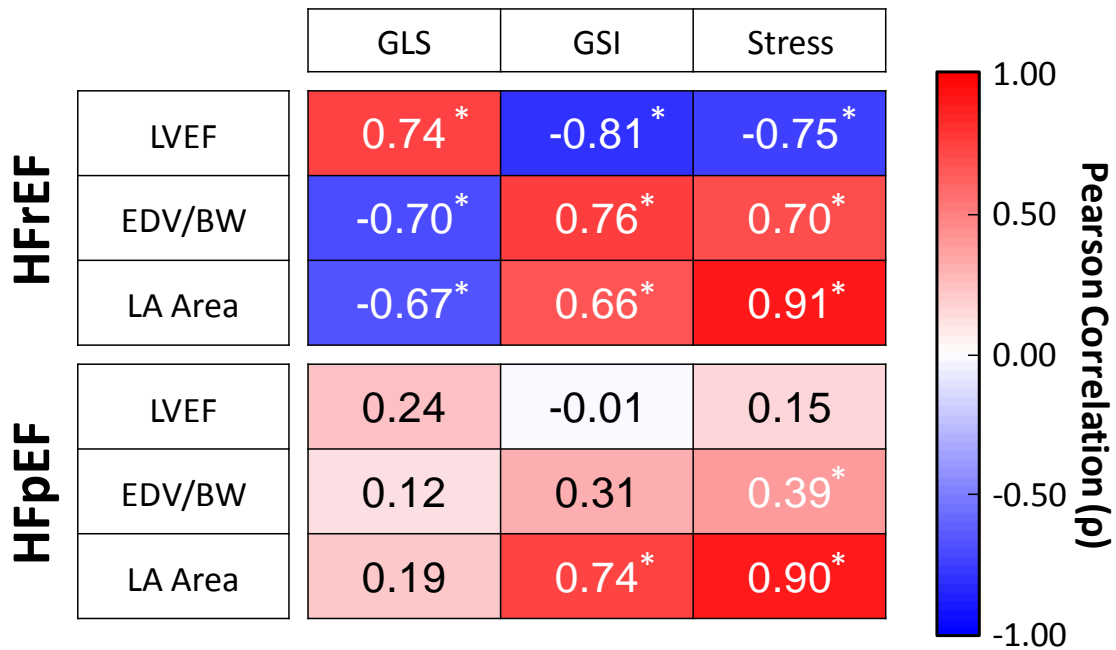
**Figure 4.6: Correlation between biomechanics and global indices of geometry and function.**

A Pearson correlation was used to interrelate standard echocardiographic response variables (LVEF, EDV/BW, and LA Area) with patient-matched changes in biomechanical response variables (GLS, GSI, and Stress) in each disease model. * $p<0.05$ for the Pearson correlation coefficient (ρ). (LVEF: left ventricular ejection fraction; EDV: end-diastolic volume; BW: body weight; LA: left atrium; GLS: global LV longitudinal strain; GSI: global stiffness index; Stress: spatial-average of 1st principal stress)

المنارة للاستشارات

www.manaraa.com
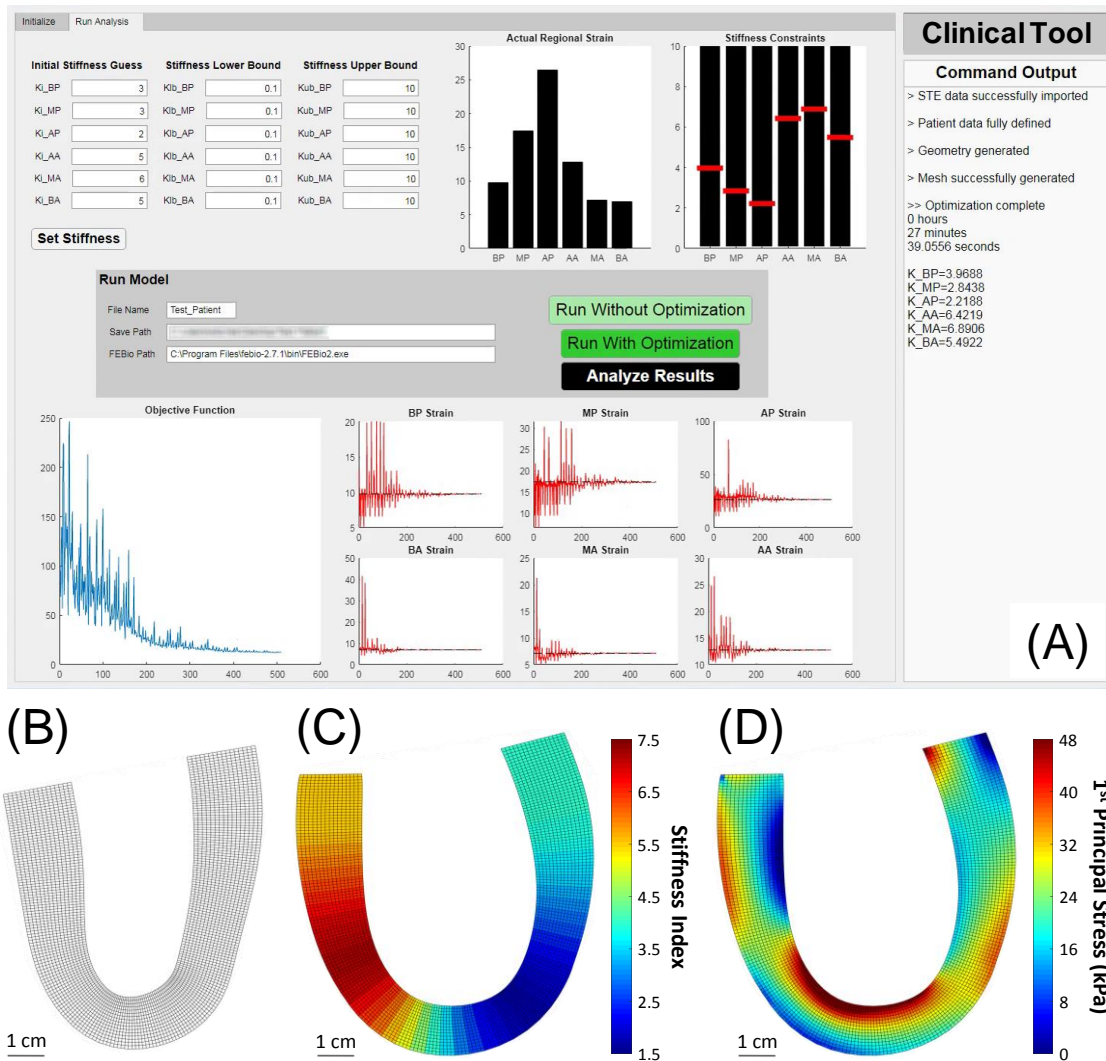
Figure 4.7: Clinical translation of methodology.
(A) This methodological process was compiled within a novel software application designed for clinical use and applied on transthoracic echocardiographic images obtained from a human subject. Quantitative strain analysis was performed, **(B)** a FE mesh was generated from the end-systolic geometry, and **(C)** the inverse method of identifying mechanical properties was applied to identify a distribution of stiffness indices. **(D)** Post-processing of the FE results allows for the calculation of first principal stress at end-diastole.

CHAPTER 5

THESIS SUMMARY AND CONCLUSION

5.1   MAJOR CONTRIBUTIONS TO THE FIELD

The seminal principal of biomechanics is the fact that the structure and function of a given tissue is a consequence of its mechanobiological environment. As the incidence of heart failure continues to rise along with the aging population in the United States, a comprehensive understanding of the mechanobiological factors that influence the progression of the disease will be of vital importance. To that end, we employed a multi-disciplinary approach to study the dynamic interplay between myocardial geometry, the collagen microstructure, mechanical behavior, and mechanical properties in response to both myocardial infarction and left ventricular pressure overload. The significant and noteworthy contributions to the field were two-fold. First, we pioneered a non-invasive approach to quantify the mechanical properties of the LV myocardium using STE. We accomplished this first through the use of stress-strain relations and a modified thick-walled ellipsoid model. We then improved upon this with an inverse finite element framework to identify the heterogeneous field of mechanical properties for both large animal models of heart failure. This work was put to practice in a prospective analysis of a HFpEF patient after deployment of the methodology into an all-inclusive software package. Second, in both models of heart failure, we identified potential therapeutic targets.

103

Our analysis of the mechanical properties in the post-MI LV (Chapter 2) showed a significant drop in mechanical stiffness in the non-viable MI region between 14- and 28-days post-MI and increases in the stiffness of the viable remote myocardium over that same period of time. These observations were coincident with increases in end diastolic volume and LV filling pressure. While it is difficult to discern cause-and-effect relationships between structural and mechanical changes, these findings underscore the potential therapeutic benefits of mechanically stabilizing the MI region early in the remodeling process (e.g. with biomaterial injections). Furthermore, the correlative analysis performed between microstructural changes and mechanical changes in the pressure-overloaded LV (Chapter 3) revealed that the reorganization of the microstructure further modulates the increase in mechanical stiffness late in the remodeling process. Specifically, we observed a reduction in fiber undulation and preferential orientation in the circumferential direction that resulted in elevated passive stiffness of the myocardium. Future work focused on limiting this microstructural reorganization could potentially improve diastolic filling by restoring the native compliance of the LV.

5.2   FUTURE WORKS

The immediate future of these works is to expand upon the multi-photon SHG imaging and inverse finite element analysis approach to develop a structure-motivated platform to identify the constitutive properties of the post-MI LV. We have performed an initial analysis of the collagen structure in the MI region three (n=3), seven (n=3), 14 (n=4), and 28 (n=3) days post-MI from a porcine model of left anterior descending artery ligation along with a cohort of referent control samples (n=3) (**Figure 5.1A**). Three-dimensional analysis of the collagen fiber network showed a relative increase in frequency of lower

values of undulation in all three layers studied as early as three days post-MI. This trend is shown to peak at 14 days post-MI which coincides with the time at which the infarcted myocardium has been shown to reach peak passive mechanical stiffness.[81,122] Furthermore, this analysis confirms previously reported claims that collagen fibers become more circumferentially aligned after MI with the majority of fibers found to be within approximately 20° of the circumferential axis at 28 days post-MI.[34] The azimuthal fiber angle and undulation in each of the epicardium, mid-myocardium, and endocardium has been incorporated into a multi-layered finite element model of the two-dimensional LV (**Figure 5.1B**). A modification of the framework introduced in Chapter 4 will be applied to these models so as to allow for the identification of the full set of parameters of the transversely-isotropic Mooney-Rivlin constitutive model. Furthermore, this analysis will shed further light on the extent to which the reorganization of the microstructure influences the passive mechanical properties of the post-MI LV.

Furthermore, while the work presented in Chapter 4 specifically relates to the LV, the same methodology can be extended to other soft tissues within the body. This extension would be contingent on two factors: (1) access to an image modality which would allow for the successful tracking of the tissue deformation in response to a given load and (2) an accurate estimation of the *in-vivo* load exerted on the tissue. Candidate applications of potentially high clinical value include assessment of thoracic or abdominal aortic aneurysms. First, the irregular geometries of these structures negate the use of analytical approaches to identify constitutive model parameters and challenge the quantification of wall stress distributions. Furthermore, STE and magnetic resonance have been previously applied to track aortic deformation during and after ventricular ejection.[178,179] Finally,

105

doppler echocardiography can be used to generate a reasonable estimation of aortic pressure.[180] Given the fact that surgical repair of aortic aneurysms carries a mortality rate approaching 10%,[181] this detailed mechanical analysis would provide surgeons with complimentary data for patient risk stratification and surgical decision making.
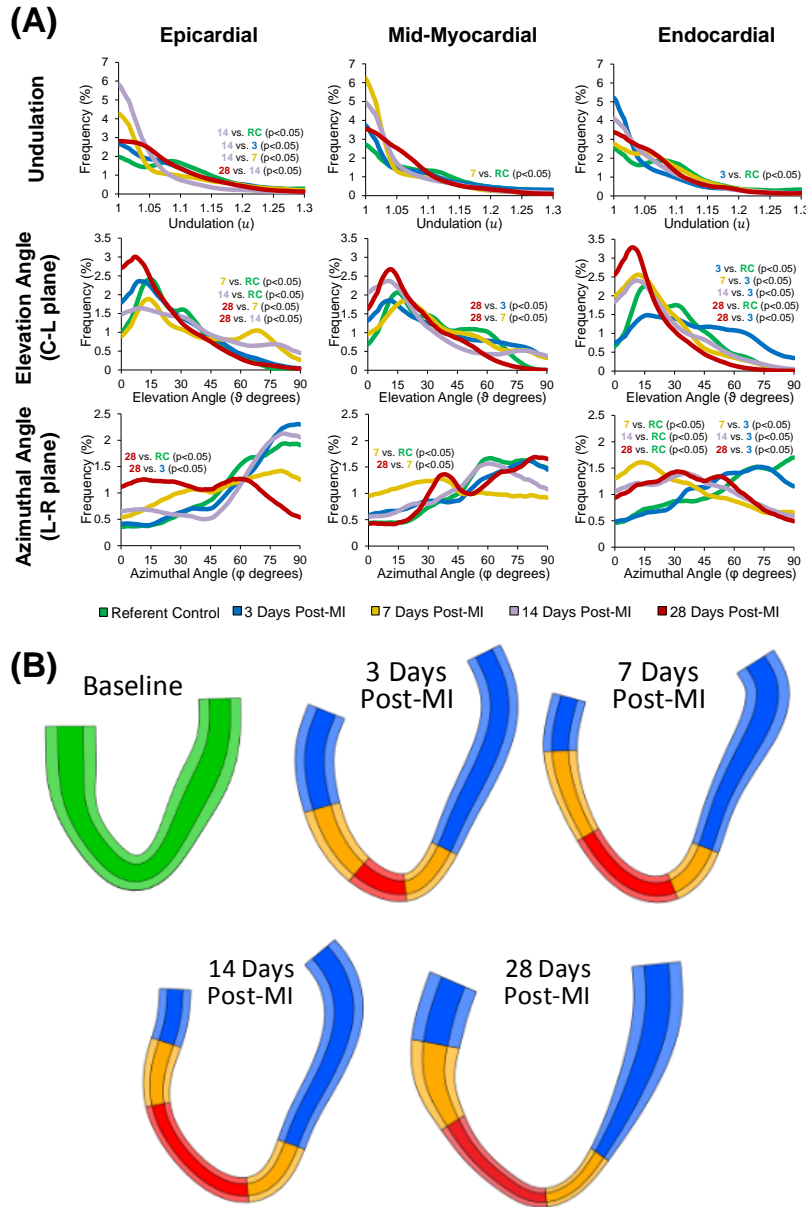
Figure 5.1: Structure-motivated model enables a transient analysis of the heterogeneous mechanical properties of the post-MI left ventricle.
(A) Regional undulation was computed for the epicardial, mid-myocardial, and endocardial sections of the MI region. Elevation angle, ϑ, was computed from the circumferential-longitudinal plane. An angle of $\vartheta=0°$ is defined as a fiber perfectly aligned with the circumferential axis. Azimuthal angle, φ, was computed from the longitudinal-radial plane. An angle of $\varphi=0°$ is defined as a fiber perfectly aligned with the radial axis. (B) Two-dimensional computational models were generated from echocardiographic images with spatial discretization of the remote myocardium (blue), border zone (orange), and the MI region (red). Future inverse finite element analysis will allow for the identification of the full set of parameters of the transversely-isotropic Mooney-Rivlin constitutive model.

107

www.manaraa.com

REFERENCES

1.	Konstam MA, Kramer DG, Patel AR, Maron MS, Udelson JE. Left ventricular remodeling in heart failure: Current concepts in clinical significance and assessment. *JACC Cardiovasc Imaging* [Internet]. 2011;4:98–108. Available from: http://dx.doi.org/10.1016/j.jcmg.2010.10.008

2.	Cheitlin MD, Armstrong WF, Aurigemma GP, Beller GA, Bierman FZ, Davis JL, Douglas PS, Faxon DP, Gillam LD, Kimball TR, Kussmaul WG, Pearlman AS, Philbrick JT, Rakowski H, Thys DM. ACC/AHA/ASE 2003 guideline update for the clinical application of echocardiography: Summary article. *J Am Soc Echocardiogr*. 2003;16:1091–1110.

3.	Lang RM, Badano LP, Mor-Avi V, Afilalo J, Armstrong A, Ernande L, Flachskampf FA, Foster E, Goldstein SA, Kuznetsova T, Lancellotti P, Muraru D, Picard MH, Rietzschel ER, Rudski L, Spencer KT, Tsang W, Voigt JU. Recommendations for cardiac chamber quantification by echocardiography in adults: An update from the American society of echocardiography and the European association of cardiovascular imaging. *Eur Heart J Cardiovasc Imaging*. 2015;16:233–271.

4.	Devereux RB, Alonso DR, Lutas EM, Gottlieb GJ, Campo E, Sachs I, Reichek N. Echocardiographic assessment of left ventricular hypertrophy: Comparison to necropsy findings. *Am J Cardiol*. 1986;57:450–458.

5.	Klein AL, Gillebert TC, Flachskampf FA, Oh JK, Lancellotti P, Appleton CP, Dokainish H, Marino P, Byrd BF, Nagueh SF, Edvardsen T, Alexandru Popescu B, Waggoner AD, Smiseth OA. Recommendations for the Evaluation of Left Ventricular Diastolic Function by Echocardiography: An Update from the American Society of Echocardiography and the European Association of Cardiovascular Imaging. *Eur Hear J – Cardiovasc Imaging*. 2016;17:1321–1360.

6.	Quiñones MA, Otto CM, Stoddard M, Waggoner A, Zoghbi WA. Recommendations for quantification of Doppler echocardiography: A report from the Doppler quantification task force of the nomenclature and standards committee of the American Society of Echocardiography. *J Am Soc Echocardiogr* [Internet]. 2002;15:167–184. Available from: http://linkinghub.elsevier.com/retrieve/pii/S089473170245599X

7.	Leitman M, Lysyansky P, Sidenko S, Shir V, Peleg E, Binenbaum M, Kaluski E,

Krakover R, Vered Z. Two-dimensional strain - A novel software for real-time quantitative echocardiographic assessment of myocardial function. *J Am Soc Echocardiogr*. 2004;17:1021–1029.

8.   Mor-Avi V, Lang RM, Badano LP, Belohlavek M, Cardim NM, Derumeaux G, Galderisi M, Marwick T, Nagueh SF, Sengupta PP, Sicari R, Smiseth OA, Smulevitz B, Takeuchi M, Thomas JD, Vannan M, Voigt JU, Zamorano JL. Current and evolving echocardiographic techniques for the quantitative evaluation of cardiac mechanics: ASE/EAE consensus statement on methodology and indications endorsed by the Japanese society of echocardiography. *Eur J Echocardiogr*. 2011;12:167–205.

9.   Axel L, Dougherty L. MR imaging of motion with spatial modulation of magnetization. *Radiology* [Internet]. 1989;171:841–845. Available from: http://pubs.rsna.org/doi/10.1148/radiology.171.3.2717762

10.   Azhari H, Weiss JL, Rogers WJ, Siu CO, Zerhouni E a, Shapiro EP. Noninvasive quantification of principle strains in normal canine hearts using tagged MRI images in 3D. *Am J Physiol* [Internet]. 1993;264:H205-16. Available from: http://www.ncbi.nlm.nih.gov/pubmed/8430847

11.   Marcu CB, Beek AM, Rossum AC Van. Clinical applications of cardiovascular magnetic resonance imaging. 2006;911–917.

12.   Pinto JG, Fung YC. Mechanical properties of the heart muscle in the passive state. *J Biomech*. 1973;6:597–606.

13.   Pinto JG, Fung YC. Mechanical properties of the stimulated papillary muscle in quick-release experiments. *J Biomech*. 1973;6:617–630.

14.   Demer LL, Yin FCP. Passive Biaxial Mechanical Properties of Isolated Canine Myocardium. *J Physiol*. 1983;339:615–630.

15.   Lin DHS, Yin FCP. A Multiaxial Constitutive Law for Mammalian Left Ventricular Myocardium in Steady-State Barium Contracture or Tetanus. *J Biomech Eng*. 1998;120:504–517.

16.   Guccione JM, McCulloch AD, Waldman LK. Passive Material Properties of Intact Ventricular Myocardium Determined From a Cylindrical Model. *J Biomech Eng*. 1991;113:42–55.

17.   Novak VP, Yin FCP, Humphrey JD. Regional Mechanical Properties of Passive Myocardium. 1994;

18.   Yin FC, Spurgeon H a, Weisfeldt ML, Lakatta EG. Mechanical properties of myocardium from hypertrophied rat hearts. A comparison between hypertrophy induced by senescence and by aortic banding. *Circ Res*. 1980;46:292–300.

19.   Humphrey JD, Strumpf RK, Yin FCP. Determination of a Constitutive Relation for Passive Myocardium: I. A New Functional Form. *J Biomech Eng* [Internet].

109

1990;112:333. Available from:
http://biomechanical.asmedigitalcollection.asme.org/article.aspx?doi=10.1115/1.2891193

20.   Humphrey JD. Cardiovascular Solid Mechanics: Cells, Tissues, and Organs. 2002.

21.   Mirsky I, Pasipoularides A. Clinical Assessment of Diastolic Function. *Prog Cardiovasc Dis*. 1990;4:291–318.

22.   Tomita M, Spinale F, Crawford FA, Zile MR. Changes in Left Ventricular Volume , Mass , and Function During the Development and Regression of Supraventricular Tachycardia-Induced Cardiomyopathy. *Circulation*. 1991;83:635–645.

23.   Zile MR, Tomita M, Ishihara K, Nakano K, Lindroth J, Spinale F, Swindle M, Carabello BA. Changes in diastolic function during development and correction of chronic LV volume overload produced by mitral regurgitation. *Circulation*. 1993;87:1378–1388.

24.   Janz RF. Estimation of Local Myocardial Stress. *Am J Physiol*. 1982;242:H875–H881.

25.   Wenk JF, Sun K, Zhang Z, Soleimani M, Ge L, Saloner D, Wallace AW, Ratcliffe MB, Guccione JM. Regional left ventricular myocardial contractility and stress in a finite element model of posterobasal myocardial infarction. *J Biomech Eng*. 2011;133:044501.

26.   McGarvey JR, Mojsejenko D, Dorsey SM, Nikou A, Burdick JA, Gorman JH, Jackson BM, Pilla JJ, Gorman RC, Wenk JF. Temporal Changes in Infarct Material Properties: An In Vivo Assessment Using Magnetic Resonance Imaging and Finite Element Simulations. *Ann Thorac Surg* [Internet]. 2015;100:582–589. Available from: http://linkinghub.elsevier.com/retrieve/pii/S0003497515003963

27.   Wenk JF, Eslami P, Zhang Z, Xu C, Kuhl E, Gorman JH, Robb JD, Ratcliffe MB, Gorman RC, Guccione JM. A Novel Method for Quantifying the In-Vivo Mechanical Effect of material Injected into a Myocardial Infarction. *Ann Thorac Surg*. 2011;92:935–941.

28.   Dorri F. A Finite Element Model of the Human Left Ventricular Systole, Taking Into Account the Fibre Orientation Pattern.

29.   Costa KD, Holmes JW, McCulloch AD. Modelling cardiac mechanical properties. *Philos Trans A Math Phys Eng Sci*. 2001;359:1233–1250.

30.   Benjamin EJ, Blaha MJ, Chiuve SE, Cushman M, Das SR, Deo R, De Ferranti SD, Floyd J, Fornage M, Gillespie C, Isasi CR, Jim'nez MC, Jordan LC, Judd SE, Lackland D, Lichtman JH, Lisabeth L, Liu S, Longenecker CT, MacKey RH, Matsushita K, Mozaffarian D, Mussolino ME, Nasir K, Neumar RW, Palaniappan L, Pandey DK, Thiagarajan RR, Reeves MJ, Ritchey M, Rodriguez CJ, Roth GA, Rosamond WD, Sasson C, Towfghi A, Tsao CW, Turner MB, Virani SS, Voeks

110

JH, Willey JZ, Wilkins JT, Wu JHY, Alger HM, Wong SS, Muntner P. Heart Disease and Stroke Statistics'2017 Update: A Report from the American Heart Association. Circulation. 2017;

31. Bursi F, Weston SA, Redfield MM, Jacobsen SJ, Pakhomov S, Nkomo VT, Meverden RA, Roger VL. Systolic and Diastolic Heart Failure in the Community. *JAMA*. 2006;

32. Bronzwaer JGF, Paulus WJ. Diastolic and systolic heart failure: Different stages or distinct phenotypes of the heart failure syndrome? *Curr Heart Fail Rep*. 2009;6:281–286.

33. Roger VL, Herges RM, Hodge DO, Jacobsen SJ, Owan TE, Redfield MM. Trends in Prevalence and Outcome of Heart Failure with Preserved Ejection Fraction. *N Engl J Med*. 2006;355:251–259.

34. Holmes JW, Borg TK, Covell JW. Structure and Mechanics of Healing Myocardial Infarcts. *Annu Rev Biomed Eng*. 2005;7:223–253.

35. Feild BJ, Russell RO, Dowling JT, Rackley CE. Regional left ventricular performance in the year following myocardial infarction. *Circulation* [Internet]. 1972;46:679–89. Available from: http://www.ncbi.nlm.nih.gov/pubmed/5072769

36. Capasso JM, Li P, Zhang X, Anversa P. Heterogeneity of ventricular remodeling after acute myocardial infarction in rats. *Am J Physiol* [Internet]. 1992;262:H486-95. Available from: http://www.ncbi.nlm.nih.gov/pubmed/1539707

37. Mukherjee R, Brinsa TA, Dowdy KB, Scott AA, Baskin JM, Deschamps AM, Lowry AS, Escobar GP, Lucas DG, Yarbrough WM, Zile MR, Spinale FG. Myocardial infarct expansion and matrix metalloproteinase inhibition. *Circulation*. 2003;107:618–625.

38. Corday E, Kaplan L, Meerbaum S, Brasch J, Costantini C, Lang TW, Gold H, Rubins S, Osher J. Consequences of coronary arterial occlusion on remote myocardium: Effects of occlusion and reperfusion. *Am J Cardiol*. 1975;36:385–394.

39. Bogen DK, Needleman A, McMahon TA. An analysis of myocardial infarction. The effect of regional changes in contractility. *Circ Res*. 1984;55:805–815.

40. Chan W, Duffy SJ, White DA, Gao XM, Du XJ, Ellims AH, Dart AM, Taylor AJ. Acute left ventricular remodeling following myocardial infarction: Coupling of regional healing with remote extracellular matrix expansion. *JACC Cardiovasc Imaging*. 2012;5:884–893.

41. Eaton LW, Weiss JL, Bulkley BH, Garrison JB, Weisfeldt ML. Regional cardiac dilation after acute myocardial infarction. *N Engl J Med*. 1979;300:57–62.

42. Mirsky I, Pfeffer JM, Pfeffer M a, Braunwald E. The contractile state as the major determinant in the evolution of left ventricular dysfunction in the spontaneously

hypertensive rat. *Circ Res* [Internet]. 1983;53:767–78. Available from: http://www.ncbi.nlm.nih.gov/pubmed/6640863

43. Wiegner a W, Allen GJ, Bing OH. Weak and strong myocardium in series: implications for segmental dysfunction. *Am J Physiol* [Internet]. 1978;235:H776-83. Available from: http://www.ncbi.nlm.nih.gov/pubmed/736165

44. Zimmerman SD, Karlon WJ, Holmes JW, Omens JH, Covell JW. Structural and mechanical factors influencing infarct scar collagen organization. *Am J Physiol Heart Circ Physiol* [Internet]. 2000;278:H194-200. Available from: http://www.ncbi.nlm.nih.gov/pubmed/10644599

45. Omens JH, Milkes DE, Covell JW. Effects of pressure overload on the passive mechanics of the rat left ventricle. *Ann Biomed Eng*. 1995;23:152–163.

46. Zile MR, Baicu CF, Gaasch WH. Diastolic Heart Failure — Abnormalities in Active Relaxation and Passive Stiffness of the Left Ventricle. *N Engl J Med* [Internet]. 2004;350:1953–1959. Available from: http://www.nejm.org/doi/abs/10.1056/NEJMoa032566

47. Grossman W, Mclaurin LP, Stefadouros MA. Left Ventricular Stiffness Associated with Chronic Pressure and Volume Overloads in Man. *Circ Res*. 1974;35:793–800.

48. Spinale FG, Tomita M, Zellner JL, Cook JC, Crawford F a, Zile MR. Collagen remodeling and changes in LV function during development and recovery from supraventricular tachycardia. *Am J Physiol*. 1991;261:H308–H318.

49. Zile MR, Baicu CF, Ikonomidis JS, Stroud RE, Nietert PJ, Bradshaw AD, Slater R, Palmer BM, Van Buren P, Meyer M, Redfield MM, Bull DA, Granzier HL, LeWinter MM. Myocardial stiffness in patients with heart failure and a preserved ejection fraction contributions of collagen and titin. 2015.

50. Miyoshi H, Oishi Y, Mizuguchi Y, Iuchi A, Nagase N, Ara N, Oki T. Effect of an increase in left ventricular pressure overload on left atrial-left ventricular coupling in patients with hypertension: A two-dimensional speckle tracking echocardiographic study. *Echocardiography*. 2013;30:658–666.

51. Vaduganathan M, Patel RB, Michel A, Shah SJ, Senni M, Gheorghiade M, Butler J. Mode of Death in Heart Failure With Preserved Ejection Fraction. *J Am Coll Cardiol*. 2017;69:556–569.

52. McKay RG, Pfeffer MA, Pasternak RC, Markis JE, Come PC, Nakao S, Alderman JD, Ferguson JJ, Safian RD, Grossman W. Left ventricular remodeling after myocardial infarction: a corollary to infarct expansion. *Circulation* [Internet]. 1986;74:693–702. Available from: http://www.ncbi.nlm.nih.gov/pubmed/3757183

53. Pfeffer MA, Braunwald E. Ventricular Remodeling After Myocardial Infarction: Experiment Observations and Clinical Implications. *Circulation*. 1990;81:1161–1172.

54.   G.J. T, J.O. H. Predictors of clinical course, coronary anatomy and left ventricular function after recovery from acute myocardial infarction. *Circulation* [Internet]. 1980;62:960–970. Available from: http://ovidsp.ovid.com/ovidweb.cgi?T=JS&PAGE=reference&D=emed1ab&NEWS=N&AN=1981002174

55.   Verma A, Meris A, Skali H, Ghali JK, Arnold JMO, Bourgoun M, Velazquez EJ, McMurray JJ V, Kober L, Pfeffer MA, Califf RM, Solomon SD. Prognostic Implications of Left Ventricular Mass and Geometry Following Myocardial Infarction. *JACC Cardiovasc Imaging*. 2008;1:582–591.

56.   Gaasch WH, Zile MR. Left ventricular structural remodeling in health and disease: With special emphasis on volume, mass, and geometry. *J Am Coll Cardiol*. 2011;58:1733–1740.

57.   Romito E, Shazly T, Spinale FG. In vivo assessment of regional mechanics post-myocardial infarction: A focus on the road ahead. *J Appl Physiol*. 2017;123:728–745.

58.   Romito E, Doviak H, Logdon C, Freels P, Shazly T, Spinale FG. Sonomicrometry-Based Analysis of Post-Myocardial Infarction Regional Mechanics. *Ann Biomed Eng* [Internet]. 2016;44:3539–3552. Available from: http://link.springer.com/10.1007/s10439-016-1694-3

59.   Gorman JHI, Gupta KB, Streicher JT, Gorman RC, Jackson BM, Ratcliffe MB, Bogen DK, Edmunds L.H. J. Dynamic three-dimensional imaging of the mitral valve and left ventricle by rapid sonomicrometry array localization. *J Thorac Cardiovasc Surg*. 1996;112:712–726.

60.   Zerhouni EA, Parish DM, Rogers WJ, Yang A, Shapiro EP. Human heart: tagging with MR imaging--a method for noninvasive assessment of myocardial motion. *Radiology* [Internet]. 1988;169:59–63. Available from: http://pubs.rsna.org/doi/10.1148/radiology.169.1.3420283

61.   Strotmann JM, Hatle L, Sutherland GR. Doppler myocardial imaging in the assessment of normal and ischemic myocardial function--past, present and future. *Int J Cardiovasc Imaging*. 2001;17:89–98.

62.   Urheim S, Edvardsen T, Torp H, Angelsen B, Smiseth OA. Myocardial Strain by Doppler Echocardiography Validation of a New Method to Quantify Regional Myocardial Function. *Circulation* [Internet]. 2000;102:1158–1164. Available from: http://circ.ahajournals.org/cgi/doi/10.1161/01.CIR.102.10.1158

63.   Thomas G. Tissue Doppler echocardiography - a case of right tool, wrong use. *Cardiovasc Ultrasound*. 2004;2:12.

64.   Choi JO, Cho SW, Song Y Bin, Cho SJ, Song BG, Lee SC, Park SW. Longitudinal 2D strain at rest predicts the presence of left main and three vessel coronary artery disease in patients without regional wall motion abnormality. *Eur J Echocardiogr*.

113

2009;10:695–701.

65. Stanton T, Leano R, Marwick TH. Prediction of all-cause mortality from global longitudinal speckle strain: Comparison with ejection fraction and wall motion scoring. *Circ Cardiovasc Imaging*. 2009;2:356–364.

66. Haugaa KH, Grenne BL, Eek CH, Ersbøll M, Valeur N, Svendsen JH, Florian A, Sjøli B, Brunvand H, Køber L, Voigt JU, Desmet W, Smiseth OA, Edvardsen T. Strain echocardiography improves risk prediction of ventricular arrhythmias after myocardial infarction. *JACC Cardiovasc Imaging*. 2013;6:841–850.

67. Chan J, Hanekom L, Wong C, Leano R, Cho GY, Marwick TH. Differentiation of Subendocardial and Transmural Infarction Using Two-Dimensional Strain Rate Imaging to Assess Short-Axis and Long-Axis Myocardial Function. *J Am Coll Cardiol*. 2006;48:2026–2033.

68. Gjesdal O, Helle-Valle T, Hopp E, Lunde K, Vartdal T, Aakhus S, Smith HJ, Ihlen H, Edvardsen T. Noninvasive separation of large, medium, and small myocardial infarcts in survivors of reperfused ST-elevation myocardial infarction: a comprehensive tissue Doppler and speckle-tracking echocardiography study. *Circ Cardiovasc Imaging*. 2008;1.

69. Reant P, Labrousse L, Lafitte S, Bordachar P, Pillois X, Tariosse L, Bonoron-Adele S, Padois P, Deville C, Roudaut R, Dos Santos P. Experimental Validation of Circumferential, Longitudinal, and Radial 2-Dimensional Strain During Dobutamine Stress Echocardiography in Ischemic Conditions. *J Am Coll Cardiol*. 2008;51:149–157.

70. Sun JP, Niu J, Chou D, Chuang HH, Wang K, Drinko J, Borowski A, Stewart WJ, Thomas JD. Alterations of Regional Myocardial Function in a Swine Model of Myocardial Infarction Assessed by Echocardiographic 2-Dimensional Strain Imaging. *J Am Soc Echocardiogr*. 2007;20:498–504.

71. Sun QW, Zhen L, Wang Q, Sun Y, Yang J, Li YJ, Li RJ, Ma N, Li ZA, Wang LY, Nie SP, Yang Y. Assessment of Retrograde Coronary Venous Infusion of Mesenchymal Stem Cells Combined with Basic Fibroblast Growth Factor in Canine Myocardial Infarction Using Strain Values Derived from Speckle-Tracking Echocardiography. *Ultrasound Med Biol*. 2016;42:272–281.

72. Bachner-Hinenzon N, Malka A, Barac Y, Meerkin D, Ertracht O, Carasso S, Shofti R, Leitman M, Vered Z, Adam D, Binah O. Strain Analysis in the Detection of Myocardial Infarction at the Acute and Chronic Stages. *Echocardiography*. 2016;33:450–458.

73. Barlow SC, Doviak H, Jacobs J, Freeburg LA, Perreault PE, Zellars KN, Moreau K, Villacreses CF, Smith S, Khakoo AY, Lee T, Spinale FG. Intracoronary delivery of recombinant TIMP-3 after myocardial infarction: effects on myocardial remodeling and function. *Am J Physiol - Hear Circ Physiol* [Internet]. 2017;313:H690–H699. Available from:

http://ajpheart.physiology.org/lookup/doi/10.1152/ajpheart.00114.2017

74. Lindsey ML, Bolli R, Canty JM, Du X-J, Frangogiannis NG, Frantz S, Gourdie RG, Holmes JW, Jones SP, Kloner RA, Lefer DJ, Liao R, Murphy E, Ping P, Przyklenk K, Recchia FA, Schwartz Longacre L, Ripplinger CM, Van Eyk JE, Heusch G. Guidelines for experimental models of myocardial ischemia and infarction. *Am J Physiol Circ Physiol* [Internet]. 2018;314:H812–H838. Available from: http://www.physiology.org/doi/10.1152/ajpheart.00335.2017

75. Yingchoncharoen T, Agarwal S, Popović ZB, Marwick TH. Normal ranges of left ventricular strain: A meta-analysis. *J Am Soc Echocardiogr*. 2013;26:185–191.

76. Hess OM, Koch R, Bamert C, Krayenbuehl HP, Policlinic M. Regional wall stiffness during acute myocardial ischaemia in the canine left ventricle *. 1980;435–444.

77. Ross JJ. Is There a True Increase in Myocardial Stiffness with Acute Ischemia? *Am J Cardiol*. 1989;63:87E–91E.

78. Hayashida W, Van Eyll C, Rousseau MF, Pouleur H, The SOLVD Investigators. Regional remodeling and nonuniform changes in diastolic function in patients with left ventricular dysfunction: Modification by long-term enalapril treatment. *J Am Coll Cardiol* [Internet]. 1993;22:1403–1410. Available from: http://dx.doi.org/10.1016/0735-1097(93)90550-K

79. Park T, Nagueh SF, Khoury DS, Kopelen HA, Akrivakis S, Nasser K, Ren G, Frangogiannis NG, Helen A. Impact of myocardial structure and function postinfarction on diastolic strain measurements : implications for assessment of myocardial viability. 2005;77030:724–731.

80. Arunachalam SP, Arani A, Baffour F, Rysavy JA, Rossman PJ, Glaser KJ, Lake DS, Trzasko JD, Manduca A, Mcgee KP, Ehman RL, Araoz PA. Regional assessment of in vivo myocardial stiffness using 3D magnetic resonance elastography in a porcine model of myocardial infarction. *Magn Reson Med*. 2017;00.

81. Gupta KB, Ratcliffe MB, Fallert M a, Edmunds LH, Bogen DK. Changes in passive mechanical stiffness of myocardial tissue with aneurysm formation. *Circulation*. 1994;89:2315–2326.

82. Guccione JM, Moonly SM, Moustakidis P, Costa KD, Moulton MJ, Ratcliffe MB, Pasque MK. Mechanism underlying mechanical dysfunction in the border zone of left ventricular aneurysm: a finite element model study. *Ann Thorac Surg*. 2001;71:654–662.

83. Jugdutt BI, Joljart MJ, Khan MI. Rate of Collagen Deposition During Healing and Ventricular Remodeling After Myocardial Infarction in Rat and Dog Models. *Circulation*. 1996;94:94–101.

115

84.   Dobaczewski M, Gonzalez-Quesada C, Frangogiannis NG. The extracellular matrix as a modulator of the inflammatory and reparative response following myocardial infarction. *J Mol Cell Cardiol* [Internet]. 2010;48:504–511. Available from: http://dx.doi.org/10.1016/j.yjmcc.2009.07.015

85.   Baxter SC, Morales MO, Goldsmith EC. Adaptive changes in cardiac fibroblast morphology and collagen organization as a result of mechanical environment. *Cell Biochem Biophys*. 2008;51:33–44.

86.   Mukherjee R, Zavadzkas JA, Saunders SM, Mclean JE, Jeffords LB, Htl CB, Stroud RE, Leone AM, Koval CN, Rivers WT, Basu S, Sheehy A, Michal G, Spinale FG. Targeted Myocardial Microinjections of a Biocomposite Material Reduces Infarct Expansion in Pigs. *Ann Thorac Surg*. 2008;86:1268–1276.

87.   Dorsey SM, McGarvey JR, Wang H, Nikou A, Arama L, Koomalsingh KJ, Kondo N, Gorman JH, Pilla JJ, Gorman RC, Wenk JF, Burdick J a. MRI evaluation of injectable hyaluronic acid-based hydrogel therapy to limit ventricular remodeling after myocardial infarction. *Biomaterials* [Internet]. 2015 [cited 2015 Sep 1];69:65–75. Available from: http://linkinghub.elsevier.com/retrieve/pii/S0142961215006638

88.   Wall ST, Walker JC, Healy KE, Ratcliffe MB, Guccione JM. Theoretical impact of the injection of material into the myocardium: A finite element model simulation. *Circulation*. 2006;114:2627–2635.

89.   Collier P, Phelan D, Klein A, Fuster V. A Test in Context: Myocardial Strain Measured by Speckle-Tracking Echocardiography. *J Am Coll Cardiol*. 2017;6.

90.   Alreshidan M, Shahmansouri N, Chung J, Lash V, Emmott A, Leask RL, Lachapelle K. Obtaining the biomechanical behavior of ascending aortic aneurysm via the use of novel speckle tracking echocardiography. *J Thorac Cardiovasc Surg* [Internet]. 2017;153:781–788. Available from: http://linkinghub.elsevier.com/retrieve/pii/S0022522316316804%0Ahttp://www.ncbi.nlm.nih.gov/pubmed/28094007

91.   Ishikawa K, Kawase Y, Ladage D, Chemaly ER, Tilemann L, Fish K, Sanz J, Garcia MJ, Hajjar RJ. Temporal changes of strain parameters in the progress of chronic ischemia: With comparison to transmural infarction. *Int J Cardiovasc Imaging*. 2012;28:1671–1681.

92.   Komajda M, Carson PE, Hetzel S, McKelvie RS, McMurray JJV V, Ptaszynska A, Zile MR, Demets D, Massie BM. Factors associated with outcome in heart failure with preserved ejection fraction: findings from the Irbesartan in Heart Failure with Preserved Ejection Fraction Study (I-PRESERVE). *Circ Heart Fail*. 2011;4:27–35.

93.   Zile MR, Gaasch WH, Anand IS, Haass M, Little WC, Miller AB, Lopez-Sendon J, Teerlink JR, White M, McMurray JJ, Komajda M, McKelvie R, Ptaszynska A, Hetzel SJ, Massie BM, Carson PE. Mode of death in patients with heart failure and

a preserved ejection fraction: Results from the irbesartan in heart failure with preserved ejection fraction study (I-Preserve) Trial. *Circulation*. 2010;121:1393–1405.

94.   Yusuf S, Pfeffer MA, Swedberg K, Granger CB, Held P, McMurray JJ V, Michelson EL, Olofsson B, Östergren J. Effects of candesartan in patients with chronic heart failure and preserved left-ventricular ejection fraction: The CHARM-preserved trial. *Lancet*. 2003;362:777–781.

95.   Ahmed A, Rich MW, Fleg JL, Zile MR, Young JB, Kitzman DW, Love TE, Aronow WS, Adams KF, Gheorghiade M. Effects of digoxin on morbidity and mortality in diastolic heart failure: The ancillary digitalis investigation group trial. *Circulation*. 2006;114:397–403.

96.   Cleland JGF, Tendera M, Adamus J, Freemantle N, Polonski L, Taylor J. The perindopril in elderly people with chronic heart failure (PEP-CHF) study. *Eur Heart J*. 2006;27:2338–2345.

97.   Massie BM, Carson PE, McMurray JJ, Komajda M, McKelvie R, Zile MR, Anderson S, Donovan M, Iverson E, Staiger C, Ptaszynska A. Irbesartan in Patients with Heart Failure and Preserved Ejection Fraction. *NEnglJMed*. 2008;2456–2467.

98.   van Veldhuisen DJ, Cohen-Solal A, Böhm M, Anker SD, Babalis D, Roughton M, Coats AJS, Poole-Wilson PA, Flather MD. Beta-Blockade With Nebivolol in Elderly Heart Failure Patients With Impaired and Preserved Left Ventricular Ejection Fraction. Data From SENIORS (Study of Effects of Nebivolol Intervention on Outcomes and Rehospitalization in Seniors With Heart Failure). *J Am Coll Cardiol*. 2009;53:2150–2158.

99.   Persson H, Lonn E, Edner M, Baruch L, Lang CC, Morton JJ, Östergren J, McKelvie RS. Diastolic Dysfunction in Heart Failure With Preserved Systolic Function: Need for Objective Evidence. Results From the CHARM Echocardiographic Substudy-CHARMES. *J Am Coll Cardiol*. 2007;49:687–694.

100.   Louridas G, Lourida K. Heart Failure in Patients with Preserved Ejection Fraction: Questions Concerning Clinical Progression. *J Cardiovasc Dev Dis* [Internet]. 2016;3:27. Available from: http://www.mdpi.com/2308-3425/3/3/27

101.   Valero-Muñoz M, Backman W, Sam F. Murine Models of Heart Failure with Preserved Ejection Fraction: a "Fishing Expedition". *JACC Basic to Transl Sci*. 2017;2:770–789.

102.   Roh J, Houstis N, Rosenzweig A. Why don't we have proven treatments for HFpEF? *Circ Res*. 2017;120:1243–1245.

103.   Krum H, Teerlink JR. Medical therapy for chronic heart failure. *Lancet* [Internet]. 2011;378:713–721. Available from: http://dx.doi.org/10.1016/S0140-6736(11)61038-6

104. Morrissey RP, Czer L, Shah PK. Chronic heart failure: Current evidence, challenges to therapy, and future directions. *Am J Cardiovasc Drugs*. 2011;11:153–171.

105. Bui, Anh L, Horwish, Tamara B, Fonarow, Gregg C. Epidemiology and risk profile of heart failure. *Nat Publ Gr*. 2012;8:1–25.

106. Lam CSP, Donal E, Kraigher-Krainer E, Vasan RS. Epidemiology and clinical course of heart failure with preserved ejection fraction. *Eur J Heart Fail*. 2011;13:18–28.

107. Zile MR, Brutsaert DL. New concepts in diastolic dysfunction and diastolic heart failure: Part I: Diagnosis, prognosis, and measurements of diastolic function. *Circulation*. 2002;105:1387–1393.

108. Zile MR, Brutsaert DL. New concepts in diastolic dysfunction and diastolic heart failure: Part II. Causal mechanisms and treatment. *Circulation*. 2002;105:1503–1508.

109. Yarbrough WM, Mukherjee R, Stroud RE, Rivers WT, Oelsen JM, Dixon JA, Eckhouse SR, Ikonomidis JS, Zile MR, Spinale FG. Progressive induction of left ventricular pressure overload in a large animal model elicits myocardial remodeling and a unique matrix signature. *J Thorac Cardiovasc Surg* [Internet]. 2012;143:215–223. Available from: http://dx.doi.org/10.1016/j.jtcvs.2011.09.032

110. Ibrahim E-SH. Myocardial tagging by Cardiovascular Magnetic Resonance: evolution of techniques--pulse sequences, analysis algorithms, and applications. *J Cardiovasc Magn Reson* [Internet]. 2011;13:36. Available from: http://jcmr-online.biomedcentral.com/articles/10.1186/1532-429X-13-36

111. Argulian E, Chandrashekhar Y, Shah SJ, Huttin O, Pitt B, Zannad F, Bonow RO, Narula J. Teasing Apart Heart Failure with Preserved Ejection Fraction Phenotypes with Echocardiographic Imaging: Potential Approach to Research and Clinical Practice. *Circ Res*. 2018;122:23–25.

112. Kraigher-Krainer E, Shah AM, Gupta DK, Santos A, Claggett B, Pieske B, Zile MR, Voors AA, Lefkowitz MP, Packer M, McMurray JJ V, Solomon SD. Impaired systolic function by strain imaging in heart failure with preserved ejection fraction. *J Am Coll Cardiol*. 2014;63:447–456.

113. Shah AM, Claggett B, Sweitzer NK, Shah SJ, Anand IS, Liu L, Pitt B, Pfeffer MA, Solomon SD. Prognostic importance of impaired systolic function in heart failure with preserved ejection fraction and the impact of spironolactone. *Circulation*. 2015;132:402–414.

114. Kato S, Koide M, Copper IV G, Zile MR. Effects of pressure- or volume-overload hypertrophy on passive stiffness in isolated adult cardiac muscle cells. *Am J Physiol Heart Circ Physiol*. 1996;271:2575–83.

115. Jalil JE, Doering CW, Janicki JS, Pick R, Shroff SG, Weber KT. Fibrillar collagen and myocardial stiffness in the intact hypertrophied rat left ventricle. *Circ Res*. 1989;64:1041–1050.

116. Schnelle M, Catibog N, Zhang M, Nabeebaccus AA, Anderson G, Richards DA, Sawyer G, Zhang X, Toischer K, Hasenfuss G, Monaghan MJ, Shah AM. Echocardiographic evaluation of diastolic function in mouse models of heart disease. *J Mol Cell Cardiol*. 2018;114:20–28.

117. Zile MR, Adamson PB, Cho YK, Bennett TD, Bourge RC, Aaron MF, Jr JMA, Abraham WT, Kueffer FJ, Taepke RT. Hemodynamic Factors Associated With Acute Decompensated Heart Failure: Part 2-Use in Automated Detection. *J Card Fail*. 2011;17:282–291.

118. Zhao L, Cheng G, Jin R, Afzal MR, Samanta A, Xuan YT, Girgis M, Elias HK, Zhu Y, Davani A, Yang Y, Chen X, Ye S, Wang OL, Chen L, Hauptman J, Vincent RJ, Dawn B. Deletion of Interleukin-6 Attenuates Pressure Overload-Induced Left Ventricular Hypertrophy and Dysfunction. *Circ Res*. 2016;118:1918–1929.

119. Epstein AM, Jha AK, Orav EJ. The Relationship between Hospital Admission Rates and Rehospitalizations. *N Engl J Med*. 2011;365:2287–2295.

120. Batson G, Chandrasekhar K, Payas Y, Rickards D. Comparison of pulmonary wedge pressure measured by the flow directed Swan-Ganz catheter with left atrial pressure. *Br Heart J*. 1971;33:616.

121. Zile MR, Tanaka R, Lindroth JR, Spinale F, Carabello BA, Mirsky I. Left ventricular volume determined echocardiographically by assuming a constant left ventricular epicardial long-axis/ short-axis dimension ratio throughout the cardiac cycle. *J Am Coll Cardiol* [Internet]. 1992;20:986–993. Available from: http://dx.doi.org/10.1016/0735-1097(92)90202-X

122. Torres WM, Jacobs J, Doviak H, Barlow SC, Zile MR, Shazly T, Spinale FG. Regional and temporal changes in left ventricular strain and stiffness in a porcine model of myocardial infarction. *Am J Physiol Circ Physiol* [Internet]. 2018;958–967. Available from: https://doi.org/10.1152/ajpheart.00279.2018

123. Stalling D, Westerhoff M, Hege H. Amira: A Highly Interactive System for Visual Data Analysis. *Vis Handb*. 2005;1:749–767.

124. Rigort A, Günther D, Hegerl R, Baum D, Weber B, Prohaska S, Medalia O, Baumeister W, Hege HC. Automated segmentation of electron tomograms for a quantitative description of actin filament networks. *J Struct Biol*. 2012;177:135–144.

125. Weber B, Greenan G, Prohaska S, Baum D, Hege HC, Müller-Reichert T, Hyman AA, Verbavatz JM. Automated tracing of microtubules in electron tomograms of plastic embedded samples of Caenorhabditis elegans embryos. *J Struct Biol*.

2012;178:129–138.

126.   Blom AS, Mukherjee R, Pilla JJ, Lowry AS, Yarbrough WM, Mingoia JT, Hendrick JW, Stroud RE, McLean JE, Affuso J, Gorman RC, Gorman JH, Acker MA, Spinale FG. Cardiac support device modifies left ventricular geometry and myocardial structure after myocardial infarction. *Circulation*. 2005;112:1274–1283.

127.   Kitzman DW, Rich MW. Age Disparities in Heart Failure Research. *JAMA*. 2010;304:1950–1951.

128.   Laplace PS. Theorie de I'action capillarie. In: Traite de mecanique celeste. Paris: 1806.

129.   Grossman W, Jones D, McLaurin LP. Wall stress and patterns of hypertrophy in the human left ventricle. *J Clin Invest*. 1975;56:56–64.

130.   Mirsky I, Laks MM. Time Course of Changes in the Mechanical-Properties of the Canine Right and Left-Ventricles During Hypertrophy Caused by Pressure Overload. *Circ Res*. 1980;46:530–542.

131.   Stroud JD, Baicu CF, Barnes MA, Spinale FG, Zile MR, Janicki JS, Dixon JA, Gorman RC, Stroud RE, Bouges S, Iii JHG, Martens TP, Itescu S, Schuster MD, Plappert T, John-sutton MGS. Viscoelastic properties of pressure overload hypertrophied myocardium : effect of serine protease treatment Viscoelastic properties of pressure overload hypertrophied myocardium : effect of serine protease treatment. 2013;5799:2324–2335.

132.   Freedman BR, Bade ND, Riggin CN, Zhang S, Haines PG, Ong KL, Janmey PA. The (dys)functional extracellular matrix. *Biochim Biophys Acta - Mol Cell Res*. 2015;1853:3153–3164.

133.   Park DW, Sebastiani A, Yap CH, Simon MA, Kim K. Quantification of coupled stiffness and fiber orientation remodeling in hypertensive rat right-ventricular myocardium using 3D ultrasound speckle tracking with biaxial testing. *PLoS One*. 2016;11:1–16.

134.   Kouzu H, Yuda S, Muranaka A, Doi T, Yamamoto H, Shimoshige S, Hase M, Hashimoto A, Saitoh S, Tsuchihashi K, Miura T, Watanabe N, Shimamoto K. Left ventricular hypertrophy causes different changes in longitudinal, radial, and circumferential mechanics in patients with hypertension: A Two-dimensional speckle tracking study. *J Am Soc Echocardiogr* [Internet]. 2011;24:192–199. Available from: http://dx.doi.org/10.1016/j.echo.2010.10.020

135.   Gaasch WH, Aurigemma GP. CMR imaging of extracellular volume and myocardial strain in hypertensive heart disease. *JACC Cardiovasc Imaging*. 2015;8:181–183.

136.   Gorgulu S, Norgaz T, Nurkalem Z, Ergelen M, Eksik A, Genc A, Zencirci AE.

Comparison of left ventricular contractility in pressure and volume overload: a strain rate study in the clinical model of aortic stenosis and regurgitation. *Echocardiography*. 2010;27:798–802.

137. Phan TT, Shivu GN, Abozguia K, Gnanadevan M, Ahmed I, Frenneaux M. Left ventricular torsion and strain patterns in heart failure with normal ejection fraction are similar to age-related changes. *Eur J Echocardiogr*. 2009;10:793–800.

138. Spinale FG, Janicki JS, Zile MR. Membrane-associated matrix proteolysis and heart failure. *Circ Res*. 2013;112:195–208.

139. Azevedo CF, Nigri M, Higuchi ML, Pomerantzeff PM, Spina GS, Sampaio RO, Tarasoutchi F, Grinberg M, Rochitte CE. Prognostic significance of myocardial fibrosis quantification by histopathology and magnetic resonance imaging in patients with severe aortic valve disease. *J Am Coll Cardiol*. 2010;56:278–287.

140. Schubert A, Binner C. Extracellular matrix gene expression correlates to left ventricular mass index after surgical induction of left ventricular hypertrophy. 2001;387:381–387.

141. Spinale FG. Matrix metalloproteinases: Regulation and dysregulation in the failing heart. *Circ Res*. 2002;90:520–530.

142. Goldsmith EC, Bradshaw AD, Spinale FG. Cellular mechanisms of tissue fibrosis. 2. Contributory pathways leading to myocardial fibrosis: moving beyond collagen expression. *Am J Physiol Cell Physiol*. 2013;304:C393-402.

143. Monrad ES, Hess OM, Nonogi H, Corin WJ, Krayenbuehl HP. Time course of regression of left ventricular hypertrophy after aortic valve replacement. *Circulation*. 1988;77:1345–1355.

144. Villari B, Vassalli G, Monrad ES, Chiariello M, Turina M, Hess OM. Normalization of diastolic dysfunction in aortic stenosis late after valve replacement. *Circulation*. 1995;91:2353–8.

145. Krayenbuehl HP, Hess OM, Monrad ES, Schneider J, Mall G, Turina M. Left ventricular myocardial structure in aortic valve disease before, intermediate, and late after aortic valve replacement. *Circulation*. 1989;79:744–755.

146. Hess OM, Ritter M, Schneider J, Grimm J, Turina M, Krayenbuehl HP. Diastolic stifness and myocardial structure in aortic valve disease before and after valve replacement. *Circulation*. 1989;79:744–755.

147. Roach MR, Burton AC. The reason for the shape of the distensibility curves of arteries. *Can J Biochem Physiol*. 1957;35:681–690.

148. Taber LA, Humphrey JD. Stress-Modulated Growth, Residual Stress, and Vascular Heterogeneity. *J Biomech Eng*. 2001;123:528.

149. Ambrosi D, Ateshian GA, Arruda EM, Cowin SC, Dumais J, Goriely A, Holzapfel

GA, Humphrey JD, Kemkemer R, Kuhl E, Olberding JE, Taber LA, Garikipati K. Perspectives on biological growth and remodeling. *J Mech Phys Solids*. 2011;59:863–883.

150. Hariton I, DeBotton G, Gasser TC, Holzapfel GA. Stress-driven collagen fiber remodeling in arterial walls. *Biomech Model Mechanobiol*. 2007;6:163–175.

151. Taber LA. Biomechanics of Growth, Remodeling, and Morphogenesis. *Appl Mech Rev* [Internet]. 1995;48:487. Available from: http://appliedmechanicsreviews.asmedigitalcollection.asme.org/article.aspx?article id=1395451

152. Fung YC. Stress, strain, growth, and remodeling of living organisms. *Z angew Math Phys*. 1995;46:S469–S482.

153. Weisman HF, Bush DE, Mannisi JA, Bulkley BH. Global cardiac remodeling after acute myocardial infarction: A study in the rat model. *J Am Coll Cardiol* [Internet]. 1985;5:1355–1362. Available from: http://linkinghub.elsevier.com/retrieve/pii/S073510978580348X

154. Klepach D, Lee LC, Wenk JF, Ratcliffe MB, Zohdi TI, Navia JL a, Kassab GS, Kuhl E, Guccione JM. Growth and remodeling of the left ventricle: A case study of myocardial infarction and surgical ventricular restoration. *Mech Res Commun* [Internet]. 2012 [cited 2015 Jan 15];42:134–141. Available from: http://www.pubmedcentral.nih.gov/articlerender.fcgi?artid=3390946&tool=pmcen trez&rendertype=abstract

155. Cohn JN, Ferrari R, Sharpe N. Cardiac remodeling-concepts and clinical implications: A consensus paper from an International Forum on Cardiac Remodeling. *J Am Coll Cardiol*. 2000;35:569–582.

156. Jacot JG, McCulloch AD, Omens JH. Substrate stiffness affects the functional maturation of neonatal rat ventricular myocytes. *Biophys J* [Internet]. 2008;95:3479–87. Available from: http://www.pubmedcentral.nih.gov/articlerender.fcgi?artid=2547444&tool=pmcen trez&rendertype=abstract

157. Janicki JS, Brower GL, Gardner JD, Chancey AL, Stewart JA. The dynamic interaction between matrix metalloproteinase activity and adverse myocardial remodeling. *Heart Fail Rev*. 2004;9:33–42.

158. Ertl G, Frantz S. Adverse cardiac remodeling: Phosphoinositide 3-kinase, another unique factor in a multifactorial condition. *Circulation*. 2012;126:2175–2176.

159. Spinale FG, Mukherjee R, Zavadzkas JA, Koval CN, Bouges S, Stroud RE, Dobrucki LW, Sinusas AJ. Cardiac restricted overexpression of membrane type-1 matrix metalloproteinase causes adverse myocardial remodeling following myocardial infarction. *J Biol Chem*. 2010;285:30316–30327.

160. Yarbrough WM, Baicu C, Mukherjee R, Van Laer A, Rivers WT, McKinney RA, Prescott CB, Stroud RE, Freels PD, Zellars KN, Zile MR, Spinale FG. Cardiac-restricted overexpression or deletion of tissue inhibitor of matrix metalloproteinase-4: differential effects on left ventricular structure and function following pressure overload-induced hypertrophy. *Am J Physiol Heart Circ Physiol* [Internet]. 2014;307:H752-61. Available from: http://www.pubmedcentral.nih.gov/articlerender.fcgi?artid=4187400&tool=pmcentrez&rendertype=abstract

161. Mirea O, Duchenne J, Voigt J-U. Recent advances in echocardiography: strain and strain rate imaging. *F1000Research* [Internet]. 2016;5:787. Available from: http://f1000research.com/articles/5-787/v1

162. Picard MH, Adams D, Bierig SM, Dent JM, Douglas PS, Gillam LD, Keller A m, Malenka DJ, Masoudi FA, McCulloch M, Pellikka PA, Peters PJ, Stainback RF, Strachan GM, Zoghbia WA. American Society of echocardiography recommendations for quality echocardiography laboratory operations. *J Am Soc Echocardiogr* [Internet]. 2011;24:930. Available from: http://dx.doi.org/10.1016/j.echo.2010.11.006

163. Lang RM, Badano LP, Mor-Avi V, Afilalo J, Armstrong A, Ernande L, Flachskampf FA, Foster E, Goldstein SA, Kuznetsova T, Lancellotti P, Muraru D, Picard MH, Rietzschel ER, Rudski L, Spencer KT, Tsang W, Voigt JU. Recommendations for cardiac chamber quantification by echocardiography in adults: An update from the American society of echocardiography and the European association of cardiovascular imaging. *Eur Heart J Cardiovasc Imaging* [Internet]. 2015;16:233–271. Available from: http://dx.doi.org/10.1016/j.echo.2014.10.003

164. Blessberger H, Binder T. Non-invasive imaging: Two dimensional speckle tracking echocardiography: basic principles. *Heart* [Internet]. 2010;96:716–22. Available from: http://www.ncbi.nlm.nih.gov/pubmed/20424157

165. Burns AT, La Gerche A, D'hooge J, Macisaac AI, Prior DL. Left ventricular strain and strain rate: Characterization of the effect of load in human subjects. *Eur J Echocardiogr*. 2010;11:283–289.

166. Farsalinos KE, Daraban AM, Ünlü S, Thomas JD, Badano LP, Voigt JU. Head-to-Head Comparison of Global Longitudinal Strain Measurements among Nine Different Vendors: The EACVI/ASE Inter-Vendor Comparison Study. *J Am Soc Echocardiogr*. 2015;28:1171–1181.

167. Ommen SR, Nishimura RA, Appleton CP, Miller FA, Oh JK, Redfield MM, Tajik AJ. Clinical Utility of Doppler Echocardiography and Tissue Doppler Imaging in the Estimation of Left Ventricular Filling Pressures : A Comparative Simultaneous Doppler-Catheterization Study. *Circulation* [Internet]. 2000;102:1788–1794. Available from: http://circ.ahajournals.org/cgi/doi/10.1161/01.CIR.102.15.1788

168. Nagueh SF, Middleton KJ, Kopelen HA, Zoghbi WA, Quiñones MA. Doppler

123

tissue imaging: A noninvasive technique for evaluation of left ventricular relaxation and estimation of filling pressures. *J Am Coll Cardiol*. 1997;30:1527–1533.

169. Weiss J a., Maker BN, Govindjee S. Finite element implementation of incompressible, transversely isotropic hyperelasticity. *Comput Methods Appl Mech Eng*. 1996;135:107–128.

170. Dorri F, Niederer PF, Lunkenheimer PP. A finite element model of the human left ventricular systole. *Comput Methods Biomech Biomed Engin*. 2006;9:319–341.

171. Goktepe S, Acharya SNS, Wong J, Kuhl E. Computational Modeling of passive myocardium. *Int j numer method biomed eng*. 2010;27:1–12.

172. Palit A, Bhudia SK, Arvanitis TN, Turley GA, Williams MA. Computational modelling of left-ventricular diastolic mechanics : Effect of fibre orientation and right-ventricle topology. *J Biomech* [Internet]. 2015;1–9. Available from: http://dx.doi.org/10.1016/j.jbiomech.2014.12.054

173. Maas SA, Ellis BJ, Ateshian GA, Weiss JA. FEBio: Finite Elements for Biomechanics. *J Biomech Eng* [Internet]. 2012;134:011005. Available from: http://biomechanical.asmedigitalcollection.asme.org/article.aspx?articleid=143139 6

174. M Moerman K. GIBBON: The Geometry and Image-Based Bioengineering add-On. *J Open Source Softw* [Internet]. 2018;3:506. Available from: http://joss.theoj.org/papers/10.21105/joss.00506

175. Hayashida W, Van Eyll C, Rousseau MF, Pouleur H, The SOLVD Investigators. Regional remodeling and nonuniform changes in diastolic function in patients with left ventricular dysfunction: Modification by long-term enalapril treatment. *J Am Coll Cardiol*. 1993;22:1403–1410.

176. Yarbrough WM, Mukherjee R, Brinsa T a, Dowdy KB, Scott A a, Escobar GP, Joffs C, Lucas DG, Crawford F a, Spinale FG. Matrix metalloproteinase inhibition modifies left ventricular remodeling after myocardial infarction in pigs. *J Thorac Cardiovasc Surg* [Internet]. 2003;125:602–10. Available from: http://www.ncbi.nlm.nih.gov/pubmed/12658202

177. Carew TE, Covell JW. Fiber orientation in hypertrophied canine left ventricle. *Am J Physiol Hear Circ Physiol* [Internet]. 1979;236:0. Available from: http://ajpheart.physiology.org/cgi/content/abstract/236/3/H487

178. Alreshidan M, Shahmansouri N, Chung J, Lash V, Emmott A, Leask RL, Lachapelle K. Obtaining the biomechanical behavior of ascending aortic aneurysm via the use of novel speckle tracking echocardiography. *J Thorac Cardiovasc Surg*. 2017;153:781–788.

179. Bell V, Mitchell WA, Sigurdsson S, Westenberg JJM, Gotal JD, Torjesen AA,

Aspelund T, Launer LJ, de Roos A, Gudnason V, Harris TB, Mitchell GF. Longitudinal and circumferential strain of the proximal aorta. *J Am Heart Assoc*. 2014;3:1–11.

180.   Teien D, Karp K, Eriksson P. Non-invasive estimation of the mean pressure difference in aortic stenosis by Doppler ultrasound. *Heart*. 1986;56:450–454.

181.   Jordan WD, Alcocer F, Wirthlin DJ, Westfall a O, Whitley D. Abdominal aortic aneurysms in "high-risk" surgical patients: comparison of open and endovascular repair. *Ann Surg* [Internet]. 2003;237:623–630. Available from: http://www.ncbi.nlm.nih.gov/entrez/query.fcgi?cmd=Retrieve&db=PubMed&dopt=Citation&list_uids=12724628

APPENDIX A

JOURNAL PERMISSION FOR USE OF MANUSCRIPT

Reuse by Authors of Their Work Published by APS

The APS Journals are copyrighted for the protection of authors and the Society. The Mandatory Submission Form serves as the Society's official copyright transfer form. Author's rights to reuse their APS-published work are described below:

Republication in New Works	Authors may republish parts of their final-published work (e.g., figures, tables), without charge and without requesting permission, provided that full citation of the source is given in the new work.
Meeting Presentations and Conferences	Authors may use their work (in whole or in part) for presentations (e.g., at meetings and conferences). These presentations may be reproduced on any type of media in materials arising from the meeting or conference such as the proceedings of a meeting or conference. A copyright fee will apply if there is a charge to the user or if the materials arising are directly or indirectly commercially supported1. Full citation is required.
Theses and Dissertations	Authors may reproduce whole published articles in dissertations and post to thesis repositories without charge and without requesting permission. Full citation is required.
Open Courseware	Authors may post articles, chapters or parts thereof to a public access courseware website. Permission must be requested from the APS1. A copyright fee will apply to a book chapter and during the first 12 months of a journal article's publication. Full citation is required.
Websites	Authors may not post a PDF of the accepted or final version of their published work to any website including social and research networking platforms; instead, links may be posted to the APS or publisher partner website where the work is published1 (see exception to authors' own institution's repository, as note below).
Institutional Repositories (non-theses)	Authors may deposit their accepted, peer-reviewed journal manuscripts into an institutional repository providing: • the APS retains copyright to the article1 • a 12-month embargo period from the date of final publication of the article is observed by the institutional repository and the author • a link to the article published on the APS or publisher-partner website is prominently displayed alongside the article in the institutional repository • the article is not used for commercial purposes • self-archived articles posted to repositories are without warranty of any kind
	1Unless it is published under the APS Open Access (*AuthorChoice*) option, which allows for immediate public access under a Creative Commons license (CC BY 4.0) (See also the APS **Policy on Depositing Articles in PMC**.)

From <https://www.physiology.org/author-info.permissions>

Figure A.1: Permission from American Journal of Physiology – Heart and Circulatory Physiology to include published manuscript in this dissertation.
Chapter 2 is included in this dissertation with permission from the publisher. Information can be found at <https://www.physiology.org/author-info.permissions>

126